Measurements of event-by-event fluctuation of anisotropic flow in pp, p+Pb and Pb+Pb collisions with the ATLAS detector

A Dissertation presented

by

Peng Huo

to

The Graduate School

in Partial Fulfillment of the

Requirements

for the Degree of

Doctor of Philosophy

in

Chemistry

Stony Brook University

August 2018

Stony Brook University
The Graduate School

Peng Huo

We, the dissertation committe for the above candidate for the
Doctor of Philosophy degree, hereby recommend
acceptance of this dissertation

Jiangyong Jia - Dissertation Advisor
Professor, Department of Chemistry

Roy A. Lacey - Chairperson of Defense
Professor, Department of Chemistry

Trevor Sears
Professor, Department of Chemistry

Derek Teaney
Associate Professor, Department of Physics and Astronomy

Björn Peter Schenke
Physicist, Physics Department, Brookhaven National Lab

This dissertation is accepted by the Graduate School

Dean of the Graduate School

Abstract of the Dissertation

Measurements of event-by-event fluctuation of anisotropic flow in pp, p+Pb and Pb+Pb collisions with the ATLAS detector

by

Peng Huo

Doctor of Philosophy

in

Chemistry

Stony Brook University

2018

Heavy ion collisions create a deconfined state of quarks and gluons, which behaves as the most perfect fluid in nature and is well described in terms of nearly inviscid hydrodynamics. Collective motion of the nuclear matter is observed to be anisotropic in momentum space, which is intepreted as the response to the lumpy density profile at the initial stage. This anistropic collective behavior is characterized by a set of flow harmonics $\boldsymbol{v}_n = v_n e^{in\Phi_n}$ corresponding to different patterns.

In the past, extensive flow studies assume the system is boost invariant and focus on the mid-rapidity, while the expansion of the nuclear matter is actually three dimensional. Recently, evidences indicate the correlation between flow harmonics $v_n e^{in\Phi_n}$ from two separated pseudorapidity (η) interval

weakens as the pseudorapidity separation broadens. This phenomenal is referred to as "decorrelation" and is studied in this thesis work at ATLAS in Pb+Pb collisions at 2.76 TeV and 5.02 TeV. The $\boldsymbol{V}_n$ decorrelation is found to have comparable contributions from the flow magnitude (v_n) and the flow phase (Φ_n). Mixed-type decorrelations, e.g. $\boldsymbol{V}_n\boldsymbol{V}_m$, $\boldsymbol{V}_n\boldsymbol{V}_m\boldsymbol{V}_k$ are also measured. In case of $\boldsymbol{V}_2$ and $\boldsymbol{V}_3$, their decorrelation is found to be independent of each other, while the decorrelation of $\boldsymbol{V}_4$ and $\boldsymbol{V}_5$ are found to be driven by nonlinear contribution from $\boldsymbol{V}_2^2$ and $\boldsymbol{V}_2\boldsymbol{V}_3$, respectively.

Collective effects are also found in these small systems, *pp* and *p*+Pb, which were treated as control experiments to the Pb+Pb collisions. Correlations of two flow harmonics v_n and v_m are measured via three- and four-particle cumulants in 13 TeV *pp*, 5.02 TeV *p*+Pb, and 2.76 TeV peripheral Pb+Pb collisions with the ATLAS detector. These results show a negative correlation between v_2 and v_3 and a positive correlation between v_2 and v_4 for all collision systems and over the full multiplicity range. However, the magnitudes of the correlations are found to depend strongly on the event multiplicity, the choice of the transverse momentum range and the collision systems. The relative correlation strength, obtained by normalization of the cumulants with the $\langle v_n^2 \rangle$ from a two-particle correlation analysis, is similar in the three collision systems and depends weakly on the event multiplicity and transverse momentum. These results based on the subevent methods provide strong evidence for a similar long-range multi-particle collectivity in *pp*, *p*+Pb and peripheral Pb+Pb collisions.

Contents

List of Figures

List of Tables

1 Introduction

In this section, we will briefly discuss the object of the study in this thesis. In Section 1.1, we will discuss the Quantum Chromodynamics, which deals with elementary particles (quarks) interacting via the strong force and with the elementary particles (gluons) which are the strong force carriers. In Section 1.2 we will discuss the object of this study, quark-gluon plasma (QGP), which is a new state of matter consisting of deconfined quarks and gluons. In Sections 1.3 and 1.4, we will discuss how QGP can be created in ultra-relativistic heavy-ion collisions and what evidences indicate the formation of QGP.

1.1 Quantum Chromodynamics

One long pursuit in particle physics is to answer the question what are the basic constituents of matter and how do they interact with each other. *Quarks* and *gluons*, collectively called *partons*, are the most fundamental constituents for nuclear matter. Quarks are "glued" by gluons to form composite particles called *hadrons*, the most stable of which are protons and neutrons. Quarks possess a property called *color charge*. There are three types color charge: arbitrarily labeled red, green and blue, and the corresponding negative units ("anti-red","anti-green","anti-blue"). Each quark carries a color, while every antiquark carries an anti-color. Gluon is bi-colored, i.e. they carry one positive and one negative unit of color. The system of attraction and repulsion between quarks is called strong interaction, which is mediated by exchanging gluons. The theory that describes strong interactions is *Quantum chromodynamics* (QCD), which is a non-abelian gauge theory with symmetry group $SU(3)$. Quantum Chromodynamics has two peculiar properties:

- *Asymptotic freedom.* Strong interaction strength becomes asymptotically weaker at large energies (or equivalently at short distances). This property is related to competition between *screening* and *anti-screening* of color charges. Vacuum fluctuations produced a cloud of virtual

quark-antiquark pairs around a quark. In the vicinity of the quark, the vacuum becomes polarized: virtual antiquarks of opposing charge are attracted to it, and virtual quarks of like charge are repelled. This polarization tends to screen the effective color charge of the quark seen by other quarks and the interaction strength becomes weaker with distance. On the contrary, cloud of virtual gluons are also polarized and tend to augment and change the effective color of the quark due to the fact a gluon is bi-colored. This is sometimes called *anti-screening*. For standard QCD with three colors, as long as there are no more than 16 flavors of quark (not counting the antiquarks separately), anti-screening prevails and the the strong interaction is asymptotically free. This phenomenon is a unique feature of non-abelian gauge theory.

- *Color confinement*. This phenomenon is closely related to asymptotic freedom, which states that no single quark exist in isolated state. For example, as the quark and antiquark in a pair are separated, the gluon field between a pair of color charges forms a narrow flux tube (or string) between them. Because of the behavior of the gluon field, the strong force between the particles is constant regardless of their separation. Therefore, the gluon binding potential is proportional to the distance. At some point, rather than extending the tube further, it becomes energetically favorable to produce a new quark-antiquark pair which combine with the existing quarks and antiquarks to form two new pairs (hadrons). This string breaking mechanism prevents produce isolated quark(antiquark) in nature. Hadrons are categorized into two families: *baryons*, made of three quarks; and *mesons*, made of one quark and one antiquark. Protons and neutrons are examples of baryons.

1.2 Quark-gluon plasma

Deconfined state of quarks is expected at extremely high temperature and/or high nuclear density. As the density increases, each quark will find more

quarks in its vicinity. This lead to screening of the color charge and less binding energy between them. At a sufficient high nuclear density, the binding energy drops to zero and quarks can move freely over an extended range beyond the size of a hadron. This deconfinement mechanism is similar to Debye screening effect in plasma, where the electric charges are screened due to the presence of other mobile charges. As the temperature increases, the energy density also increases and produces numerous virtual quark-antiquark pairs from vacuum, which also leads to the screening effect. This deconfined state is firstly called as *quark-gluon plasma* (QGP) by Edward Shuryak in 1978 [1].

Figure 1 is a sketch of the possible QCD phase diagram, including conjectures which are not fully established. The vertical axis is temperature T, which is related to energy density ϵ, and the horizontal axis is baryon chemical potential μ_B, which reflects the net baryon (number of quarks offset by the number of anti-quarks) density. The vacuum is at the origin of the axes and the ordinary nuclear matter is at T = 0 MeV and μ_B = 900 MeV (the mass of a nucleon).

In the lower left region, quarks and gluons are confined in the hadron state, while if keeping μ_B constant and increase the temperature, the quark-gluon plasma state is reached. The strength of the color force means that quark-gluon plasma behaves as a near-ideal Fermi liquid, while hadrons are color neutral and weakly interacted behaving like gas. From lattice QCD calculations [2–4], the phase transition is predicted to appear as smooth crossover at finite μ_{B}. For example, Lattice QCD calculations at μ_{B} = 0 indicate that the transition occurs around temperatures of ~ 170 MeV [5]. On the other hand, at high μ_{B}, a first order phase transition is predicted. It is believed that the two different phase transitions are separated by a QCD critical point [6]. Apart from hadrons and QGP phase, a color superconductor phase is conjectured at the lower right corner. This low T and high μ_B state is conjectured to exist in the core of neutron stars, which is formed by the gravitational collapse of large stars. The structure of the phase diagram

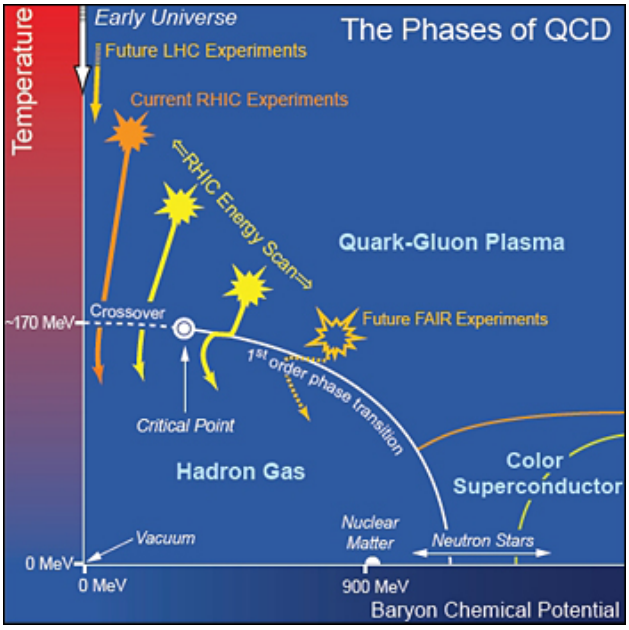

Figure 1: Schematic phase-diagram of QCD matter. Solid lines indicate phase boundaries between the different phases. The solid circle indicates the critical point for the hadron-gas to QGP phase transition. Note that the existence of a critical point is conjectured, its existence has not been established.

is of great interest since it is determined by the QCD.

1.3 Heavy-ion collisions

Ultra-relativistic heavy-ion collisions are proposed as one method to create quark-gluon plasma in laboratory [7]. Two nuclei are accelerated to near the speed of light and guided to collide head on. Tremendous energy is released into the tiny collision region and a phase transition is expected to transform the normal hadronic matter into QGP. One parameter of the collision is the center-of-mass energy ($\sqrt{s_{\rm NN}}$) per nucleon pair, which controls the energy density and temperature.

Relativistic Heavy Ion Collider (RHIC) and Large Hadron Collider(LHC)

are the two main facilities, both of which can accelerate and collide a good variety of particle species. At LHC, proton+proton (pp), proton+lead (p+Pb), lead+lead (Pb+Pb) and xenon-xenon (Xe+Xe) systems are boosted to center-of-mass energy range from 2.76 trillion electron volts (TeV) to 13 TeV. At RHIC, gold-gold (Au+Au), pp, copper+copper (Cu+Cu), deuteron+Au (d+Au), etc. can be boosted to a wide energy range from 7.7 GeV to 500 GeV. In this thesis, we will use "A+A" to denote these heavy nuclei collision, e.g. Au+Au, Pb+Pb, while when we use the term "small systems", we are referring to collisions involving at least one light nucleus, e.g pp, p+Pb, etc.

When center-of-mass energy is more than 100 GeV, the baryons inside nuclei tend to recede away from the center of mass without being completely stopped, leaving behind a nuclear matter with high temperature (energy) and low baryon density. As shown on Figure 1, LHC approaches QGP phase at high temperature low baryon density region, which is close to what universe is believed to be shortly after the big bang. When center-of-mass energy is around tens of GeV, the collision tend to stop each nucleon, forming a nuclear matter of both high temperature and high baryon density. RHIC could perform a beam energy scan over a wide μ_B region on the QCD phase diagram, serve to map out the critical point and phase boundaries.

The fireball created in the heavy ion collision is encoded with a non-trivial initial geometry of the interaction region, which is preserved through the space-time evolution of the system and eventually reflected in the final particle distributions. A brief description of the initial geometry and space-time evolution will be discussed below.

Geometry of the collision

Here, we are taking about the initial geometry of the collision at the crossing time of two nuclei.

The geometry is rather simple in longitudinal direction (see fig. 2(a)). In the z-axis (along the moving direction of particle beam), the nuclei are traveling at 99.9999991% times the speed of light when the center of mass energy

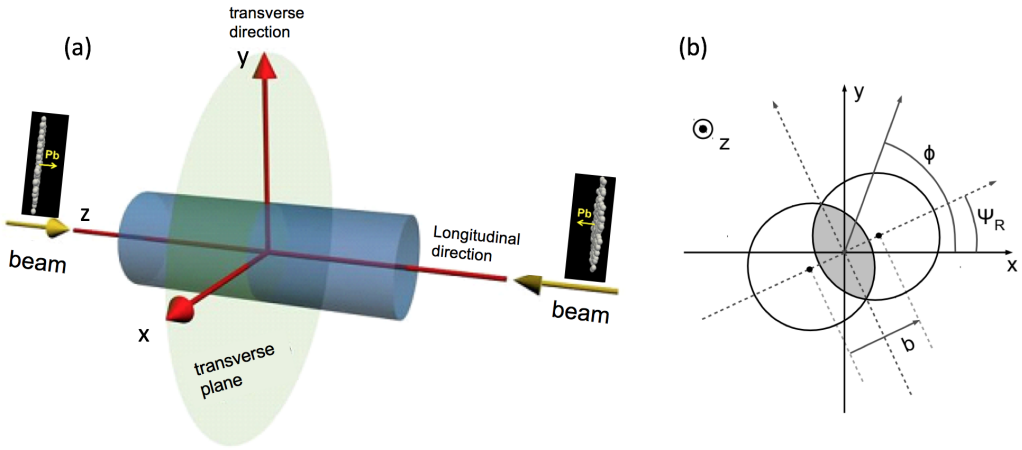

Figure 2: (a): Schematic of the coordinate system. (b): Schematic of a non-central nucleus-nucleus collision viewed in transverse plane.

is 7 TeV. And each nucleus looks like a pancake due to Lorentz contraction ($\gamma \sim 7000$).

The geometry in transverse plane (x–y plane) is non-trivial (see fig. 2(b)). It is convenient to use cylindrical coordinates (r, ϕ), with ϕ being the azimuthal angle. Impact parameter vector ($\boldsymbol{b}$) is defined as the line interval between the center of two nuclei. Together with z-axis, a unique plane, called *reaction plane* (RP) is defined for each event. The event plane angle Ψ_R fluctuates randomly from event to event. In non-central collisions, if the nucleon density within the nuclei is continuous, the initial nuclear overlap region is spatially asymmetric with an "almond-like" shape. Only nucleons in this overlap region interact in the collisions, which are called *participants* or *wounded nucleons*, while the undeflected nucleons are called *spectators*. The number of participants is denoted as N_{part} [8]. In real case, fluctuations of the nucleon wave function generate a rather lumpy density profile event-by-event, which contains rich patterns of deformation besides an almond shape. This will be elaborated later in Section 2.3.2.

Besides the shape, the volume of the interaction region is also very important to characterize an heavy ion collision. The volume reflects the amount

of energy deposited in the collision, which in turn is related to the number of produced particles, which is referred to as *multiplicity*. Intuitively, the volume is characterized by a concept *centrality* [9, 10], defined as a percentage. Conventionally, 0% refers to a collision with fully overlap of two nuclei (b = 0), which has a large N^{part} and large multiplicity. And 100% centrality means the two nuclei touch each other tangentially and b roughly equals to the sum of the radii of the colliding nuclei, along with less particles being produced. Collisions are often categorized as central, mid-central and peripheral; they have small, mediocre and large centrality values correspondingly. In practice, b, N_{part} and multiplicity can be used to determine centrality equivalently. In Monte Carlo Glauber model [8], multiplicity is a function proportional to N_{part} and number of binary nucleon nucleon collisions (N_{bin}) the participants undergo. So there is a straightforward mapping of the experimental observables to centrality and to the Glauber quantities, as illustrated in Figure 3.

Evolution of Heavy Ion Collisions

The fireball created after the heavy ion collisions evolves dynamically with a characteristic size ~ 10 fm and a fleeting characteristic time ~ 10 fm/c [11]. What is seen by the detector is only the final particles. The standard model of heavy ion collisions divide the whole evolution into several stages, which are illustrated in Figure 4 and can be roughly categorized as the following:

- Initial state: The initial geometry of density profile is determined at this stage. Currently, there are two prevailing models, Glauber and Color Color Condensate (CGC), which handle initial density deposition with different approaches. The collision happens through multiple parton-parton scatterings. The time scales of the scatterings is related to the inverse of the momentum transferred Q. Thus a hard scattering, which produced high transverse momentum p_{T} particles, happens in the very very early time, followed by the production of low p_{T} particles by the time ~ 0.2 fm/c. If the produce partons weakly interact, they

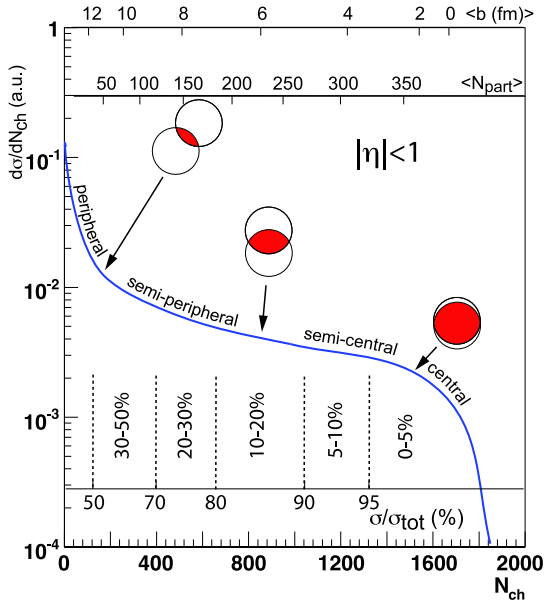

Figure 3: The schematic of the mapping of the experimental observables to centrality variable and to Glauber quantities [8].

will evolve independently into hadrons, as in the case of pp. However, the multiple parton scattering lead to fast establishment of a locally thermalized nuclear matter. The data suggests that the thermalization is reached by ~ 1 fm/c and QGP is formed at that time [7].

- QGP phase: Further fast parton scatterings build up pressure at macroscopic level. Outside the QGP is vacuum, thus the fireball expands outward and cools down. However, these pressure gradients are anisotropic, due to the elliptic nature of the average overlap geometry between the colliding nuclei as well as fluctuations in the initial energy distribution, resulting in anisotropic expansion rate of the fluid. This stage of the

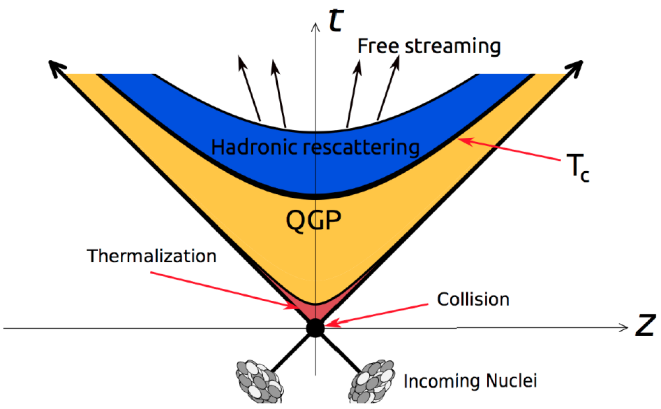

Figure 4: The schematic of the time evolution of a relativistic heavy ion collision. The horizontal axis represents the beam direction and the vertical axis is the proper time.

collision has been shown to be very well described by relativistic hydrodynamics with a very small shear-viscosity to entropy-density ratio η/s.

- Hadronization: The expanding fireball eventually becomes cool and dilute. At a point the interactions among partons are sufficiently strong to confine the partons into hadrons. A mechanism called *recombination* or *coalescence* is employed to describe this process. Energetic partons might hadronize via *fragmentation*, a different scheme that explains the formation of hadron *jets*. Note the fragmentation functions are modified by existence of QGP medium compared to the case in vacuum.

- Hadron gas: This stage might exist for a short time. Hadrons are weakly coupled and still exhibit collective behavior. The whole system is still in equilibrium. Due to the relatively weak interactions among hadrons, the system resembles a dilute gas and is best described by transport models such as the Ultra-relativistic Quantum Molecular Dynamics model (UrQMD). Recent studies seem to suggest that the life-

time of this stage is so small that its influence to anisotropy of particle momentum distribution is very limited.

- Freeze-out: As the system further expands and continues to cool down. Interactions among hadrons become even weaker and the typical mean free path of hadrons becomes comparable to the size of the system. There is no hadron interaction and particles free stream to detector. This stage is called *kinetic freeze-out*.

1.4 QGP signature

QGP is not directly seen by the detector due to its short lifetime, but it leaves many fingerprints. On one hand, QGP provides the medium background and some physics processes could be modified via interaction with the medium. Thus one expect quite different behavior compared to the vacuum. On the other hand, QGP has many signatures directly related to itself, e.g. photon and muon rates, sizable collective flow etc. Here we only introduce few of these evidences.

Quarkonium suppression: In particle physics, *quarkonium* designates a meson whose constituents are a heavy quark and its own antiquark. Υ particle, a quarkonium consisting of a bottom and an anti-bottom quark, exists in three states known as 1S, 2S and 3S, in decreasing order of how tightly the quarks are bound. Because they are more loosely bound, the 2S and 3S states will melt more readily in the QGP. CMS observed a dramatic difference in the number of $\Upsilon(2S)$ and $\Upsilon(3S)$ produced in the heavy-ion and proton collisions, as expected in case their production is suppressed by the QGP [12]. The relative production of the excited states of the Υ particle in heavy-ion collisions is only about 30% that of the comparative rates from proton collisions.

jet quenching: In a hard scattering, final partons gain large transverse energy p_{T} and have a large virtuality, which are reduced by radiating gluons or splitting into quark antiquark pairs. Consequently, the outgoing parton

fragments into a collimated stream of hadrons, referred as a *jet*. If a QGP is formed, the hard scattering parton will interact with the medium and loss energy, thus the energy of those partons and their fragmentation functions are modified compared to the case in vacuum. As expected, the jet yield is suppressed compared to expectation from proton-proton collisions , which is called *jet quenching*. The ratio of the measured to expected yield is denoted by R_{AA}. In central heavy ion collisions jet R_{AA} values close to 0.5 are observed implying that the jets are heavily quenched in the produced medium [13].

strangeness enhancements: Once formed, QGP transfers heat internally by radiation just like any hot object. However there is enough energy available that gluons collide and produce an excess of the heavy strange quarks. Whereas, if the QGP didn't exist and there was a pure collision, the same energy would be converted into a non-equilibrium mixture containing even heavier quarks such as charm quarks or bottom quarks. Enhancement of strange baryon production relative to *pp* collisions have been observed in the experimental data [14].

2 Collective phenomena in heavy-ion collisions (H.I.C.)

The study of collective phenomena of a strongly correlated, interacting many-body system has been an important topic in many fields of physics, from the very large scale (the cosmos) to the very small scale (elementary particles). They form the "complexity frontier" in physics, which address the question how patterns of large-scale behavior emerge from the complex interactions of the small constituent parts. One of the key question in these study is to find out the fundamental laws that describe these collective behaviors.

2.1 Collective Phenomena in H.I.C

Early studies on RHIC's heavy ion collisions indicates the produced QGP matter appears to be more like a liquid rather than the expected gas. These studies indicate that the primordial particles produced in the collisions tend to move collectively in response to variations of pressure across the volume formed by the colliding nuclei. This phenomenon is referred to as *flow* [15], in analogous to the properties of fluid motion.

This azimuthal anisotropy of flow is of great importance. In a non-central collision (see fig. 5(left)), the the overlap region has an "almond-like" shape, where nuclear matter distribution is assumed to be continuous. The average pressure gradient between the center of the overlap region and the surrounding vacuum is larger in reaction plane (horizontal) than out of plane (vertical) direction because the system is thinner in that direction. Then anisotropically flowing medium emits particles boosted in the flow direction and therefore the observed particles have a momentum anisotropy approximately proportional to the initial elliptic deformation (see fig. 5(right)).

Later on, it was realized that on the event-by-event basis, the initial geometry is not smooth but fluctuates around the averaged elliptic shape due to random positions of wounded nucleons (see fig. 6). This detailed deformation is characterized by a mode decomposition method with respect

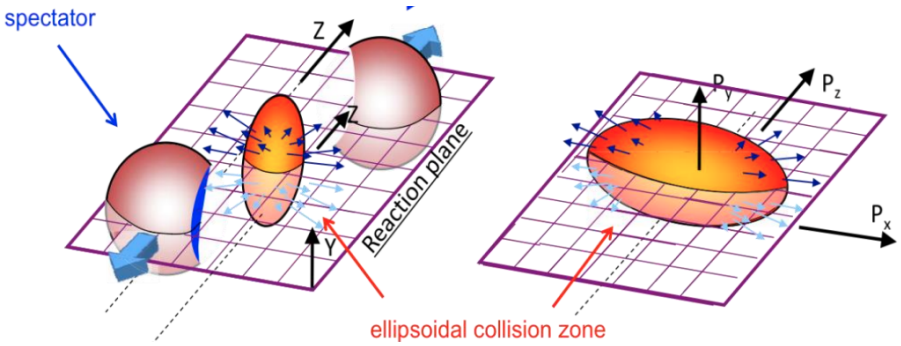

Figure 5: Left: View of a non-central collision. Right: The initial spatial anisotropy translates via pressure gradients into a momentum anisotropy of the produced particles.

to the azimuthal asymmetry of initial density profile. If one takes the complex expression $z = x + iy = re^{i\phi}$ for the transverse coordinates, a set of (complex) dimensionless harmonic coefficients *eccentricity* are defined [16, 17]

$$\varepsilon_1 \equiv \epsilon_1 e^{i\phi_1} = -\frac{\langle z^2 z^* \rangle}{\langle |z|^3 \rangle} = -\frac{\langle r^3 e^{i\phi} \rangle}{\langle r^3 \rangle} \tag{1}$$

$$\varepsilon_n \equiv \epsilon_n e^{i\phi_n} = -\frac{\langle z^n \rangle}{\langle |z|^n \rangle} = -\frac{\langle r^n e^{in\phi} \rangle}{\langle r^n \rangle} \ (n > 1) \tag{2}$$

where (r, ϕ) is relative to center-of-mass and $\langle \cdots \rangle$ denotes an average over all the participating nucleons. By definition, the magnitude ϵ_n is bounded by unity. Additionally, one can also use cumulants since the average Glauber distribution is roughly Gaussian and the cumulants are translationally invariant [16]. Due to fluctuations, even when two nuclei are fully overlapped, deformations of any order could exist, which in turn generate momentum anisotropies.

2.2 Harmonic flow

Anisotropies in particles' momentum ($\boldsymbol{p}$) distribution is a key observable since it is related to the initial spatial anisotropies as well as the medium properties of QGP. We first define a new coordinate system in momentum space

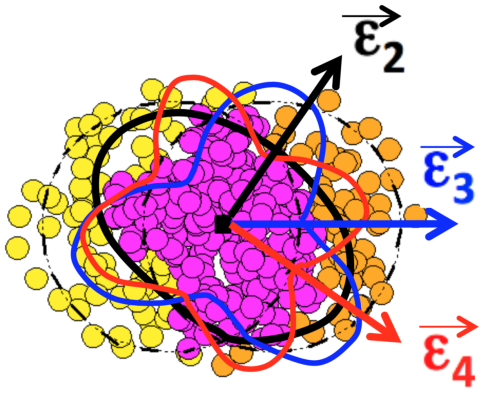

Figure 6: Distribution of nucleons showing an initial geometry with many components from Monte Carlo Glauber.

$(p_{\mathrm{T}}, y/\eta, \phi)$, which is related to the Cartesian coordinate system (p_x, p_y, p_z) by (see fig. 7).

$$\begin{aligned} p_x &= p_T \cos\phi \\ p_y &= p_T \sin\phi \\ p_z &= \sqrt{p_T^2 + m^2}\sinh y \end{aligned} \tag{3}$$

where the rapidity (y) is

$$y = \frac{1}{2}\ln\frac{E + p_z}{E - p_z} \tag{4}$$

the pseudorapidity (η) is

$$\eta = \frac{1}{2}\ln\frac{|\boldsymbol{p}| + p_z}{|\boldsymbol{p}| - p_z} = -\ln\tan(\frac{\theta}{2}) \tag{5}$$

here θ is the polar angle between $\boldsymbol{p}$ and beam axis (z). When the mass of the particle is negligible (or the particle moves at near the speed of light), pseudorapidity is equivalent to rapidity. For example, the invariant mass of a pion–the most abundant species of detected hadrons–m_π = 140 MeV is small compared to the typically measured transverse momentum 1 GeV, therefore we have $\eta_\pi \approx y_\pi$. In hadron collider physics, the pseudorapidity is

preferred over the polar angle ϕ because, loosely speaking, particle production is constant as a function of pseudorapidity.

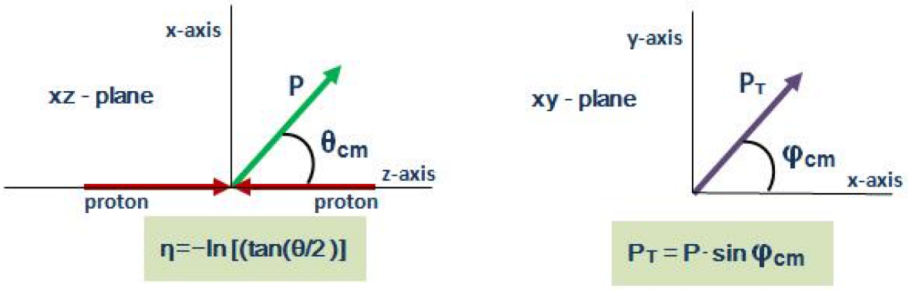

Figure 7: Schematic of coordinate system in momentum space.

Then the momentum distribution of detected particles is characterized by Fourier expansion:

$$E\frac{d^3N}{d^3p} = \frac{1}{2\pi}\frac{d^2N}{p_{\mathrm{T}}dp_{\mathrm{T}}d\eta}(1+\sum_{n=1}^{\infty}2v_n(p_{\mathrm{T}},\eta)\cos[n(\phi-\Phi_n)]) \tag{6}$$

These Fourier coefficient v_n are referred to as *harmonic flow* [15]. Usually the first few harmonics are important: directed flow(v_1), elliptic flow(v_2), triangular flow(v_3), quadrangular flow (v_4) and pentagonal flow (v_5) (see fig. 8). The n^{th} order flow is described as the response to the n^{th} eccentricity $v_n \propto \epsilon_n$ ($n \leq 3$) in hydrodynamics. Here, the v_n coefficients are functions of η and p_{T}, and as such they are often referred to as *differential flow*.

The phase Φ_n, referred to as *event plane angle*, reflects the orientation of the n^{th} order flow, which has n-fold symmetry, i.e. the distribution is rotational invariant under a phase shift $\Phi_n \to \Phi_n + 2\pi/n$.

The differential flow ($v_n(p_{\mathrm{T}},\eta)$) integrated over a broad η and p_{T} window, are often referred to as *integrated flow*

$$\frac{dN}{d\phi} = \frac{N}{2\pi}(1+\sum_{n=1}^{\infty}2v_n\cos[n(\phi-\Phi_n)]) \tag{7}$$

Given the above Fourier expansion, using the orthogonality properties of trigonometric functions, one can show that

$$v_n = \langle\cos[n(\phi-\Phi_n)]\rangle \tag{8}$$

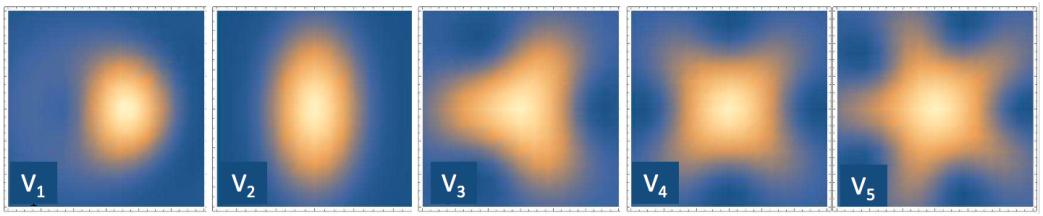

Figure 8: Schematic of the first few n−th order anisotropy in transverse plane. Reproduced from [18]

where the brackets denote average over all the particles in one event. Usually, it's convenient pack the v_n and Φ_n together in the complex format $\boldsymbol{V}_n = v_n e^{in\Phi_n}$ or as a vector $\vec{v}_n = (v_n \cos(n\Phi_n), v_n \sin(n\Phi_n))$. Similarly, one can show

$$\boldsymbol{V}_n = v_n e^{in\Phi_n} = \left\langle e^{in\phi} \right\rangle \tag{9}$$

Figure 9 shows an example of the differential flow as a function of p_{T} in one centrality interval (left) and integrated flow over $p_{\mathrm{T}} > 0.2$GeV as a function of centrality (right) in Pb+Pb. Also hydrodynamic calculations (solid curves) are drawn with the data [19]. Excellent agreement is reached with a low viscosity $\eta/s = 0.2$ at LHC energy for flow with order $n = 2 - 5$.

The main interest of anisotropic flow is due to its sensitivity to the early time dynamics [20]. The anisotropy in particle momentum space origins from the initial spatial anisotropy. Since the spatial anisotropies decrease rapidly with time, the anisotropic flow can develop only in the first fm/c. Secondly, the anisotropic flow provides information to the transport properties of the medium, such as η/s. Lastly, almost 99% of total particle yields are soft (low p_{T}) particles. And collective evolution is a main source for these soft particle production.

2.3 Flow paradigm

Based on extensive studies over the past couple of decades, the community has converged to the flow paradigm in heavy ion (A+A) collision systems,

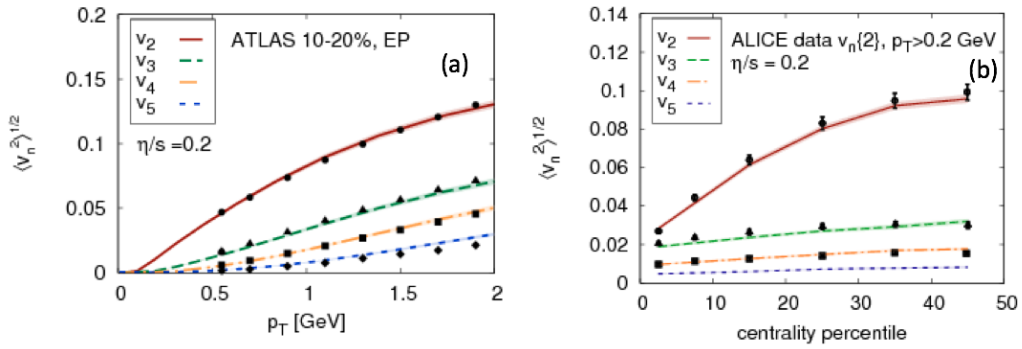

Figure 9: Left:The $v_n(p_{\mathrm{T}})$ values from Pb+Pb collisions at LHC by ATLAS (solid points) compared to values from hydrodynamic calculations (solid curves). Right:The integrated v_n over $p_{\mathrm{T}} > 0.2$GeV as a function of centrality from Pb+Pb collisions at LHC by ALICE with hydrodynamic calculations [19].

where deformations in the lumpy initial energy density profile are fully transposed to the collective anisotropy flow via strong final-state interactions. The dynamics of the QGP evolution are described by nearly ideal hydrodynamics. There are three main ingredients in this flow paradigm: hydrodynamic modeling, geometrical properties of the initial state and medium response.

2.3.1 Hydrodynamic framework

Ideally, the collective behavior of quark-gluon plasma can be described from first principle using quantum chromodynamics (QCD). The QCD Lagrangian density is

$$L = \bar{\psi}_i(i\gamma_\mu D^\mu_{ij} - m\delta_{ij})\psi_j - \frac{1}{4}F_{\mu\nu\alpha}F^{\mu\nu\alpha} \tag{10}$$

where ψ_i is a quark field, γ_μ are Dirac matrices, D^μ is a covariant derivative, m is a quark mass, δ is Kronecker delta symbol and $F^{\mu\nu\alpha}$ is the field strength of the gluons. However albeit simple looking of the Lagrangian , the non-linear interaction of gluons, and the dynamical many body system and color confinement makes direct prediction impossible. Alternatively, the

hydrodynamic model provides a phenomenological theory to build the bridge between theory and data. Hydrodynamic models can describe the data with just few thermodynamic variables, thus provides an intuitive and transparent picture without need to know the details of the interaction on the microscopic level. The hydrodynamic model is applicable when the mean free path of the system is smaller than the size of the system, $\lambda_{m.f.p} \ll L$ and the system is required to be in approximate local thermal equilibrium.

The equations of motion in hydrodynamic model are just a set of conservation laws related to the equation of state, viscosity and heat conductivity of the fluid. In ideal (zero viscosity) hydrodynamics, local conservation laws for the energy-momentum tensor and conserved charges are

$$\partial_\mu T^{\mu\nu} = 0, \quad \partial_\mu N_j^\mu = 0 \tag{11}$$

where $T^{\mu\nu}$ is energy-momentum tensor defined as a function of energy density e, pressure P and flow four-velocity u^μ and N_j^μ is the j^{th} conserved current. Also the system satisfy the constraint from the second law of thermodynamics

$$\partial_\mu S^\mu = 0 \tag{12}$$

where S^μ is the entropy current.

In reality, the system is not ideal and there will be deviations from local thermal equilibrium. The expressions for particle current, energy-momentum tensor and the entropy current will be modified from their equilibrium form, including more terms. Details of equations of motion can be find in Ref. [18].

Once the system becomes so dilute that hydrodynamics is not applicable, the fluid cells are transformed into hadrons through the Cooper and Frye formalism, in which hadrons are generated from a fluid on a 3D hyper-surface Σ determined by the freeze out conditions. The momentum distribution of hadrons from Cooper-Frye formalism is given as

$$E\frac{dN_i}{d^3p} = \int_\Sigma d\sigma \cdot p f(u^\mu, T, \mu) \tag{13}$$

where $f(u^\mu, T, \mu)$ is the phase-space distribution function. Contrast to this sudden freeze-out scenario, an alternative hybrid approach takes into account

the subsequent hadron interaction using a transport model until a kinetic freeze-out is reached.

2.3.2 Initial conditions

Extracting medium properties from hydrodynamic calculations requires a good quantitative constraint on the initial conditions. While there are different approaches to build the model, they must satisfy two main essential requirements: (a) a good description of initial state geometry and fluctuations, (b) an *ab initio* mechanism of multi-particle production.

The simplest model is Monte Carlo Glauber [8]. Nucleons in each nucleus are treated as round balls and distributed with the Woods-Saxon functional form. The nucleus-nucleus collision is treated as the superposition of multiple nucleon-nucleon collisions, which are determined by the energy dependent inelastic cross section. The energy deposition of each nucleon-nucleon collision in the transverse plane is according to a two-dimensional Gaussian with a width parameter typically chosen as 0.4 fm. Fluctuation of initial geometry in each event stems from the random positions of a finite number of nucleons sampled from distribution function. In A+A systems the nucleon-level Galuber is sufficient enough to provide confidence in the overall heavy ion standard model space-time evolution and extraction of matter properties such as η/s with precision. In small systems, e.g. pp, fluctuations are extended by including the detailed substructure of the nucleon. One simple approach is to decompose each nucleon into three valance quark, each with a cloud of gluons around it, and that each valence quark cloud interact when it comes within some fixed distance of another such cloud.

The Color Glass Condensate (CGC) is a QCD-based effective theory, describes the physics of the nonlinear gluonic interactions at high energy. The CGC model provides a consistent first-principles framework to understand the initial conditions of heavy ion collisions [21]. When heavy ions are accelerated to near light speed, gluon density is saturated and each nucleus can be view as a "gluon wall" (see fig. 10(a)). This steady state of maximal

gluon concentration is called *color glass condensate*. The gluons themselves are disordered and do not change their positions rapidly because of time dilation, similar like glass in nature. Condensate means that the gluons have a very high density. When the two nucleus collide, they pass through each other and the gluons interact to form "flux tubes". This is the initial state of quark-gluon plasma (QGP), called a *glasma* [22], because it has properties that lie between CGC and Quark Gluon Plasma (see fig. 10(b)).

The impact parameter dependent Glasma model (IP-Glasma) is based on CGC, where the gluon fields are described by classical Yang-Mills equations of motions [19]. Besides the fluctuations in distribution of nucleons, there are fluctuations in the color charge distribution inside each nucleon, which lead to "lumpy" gluon configurations. The scale of lumpiness is given on average by the nuclear saturation scale Q_s which corresponds to distance scale smaller than the nucleon size. The initial energy deposition is computed in terms of overlapping gluon fields. As for small collision systems, the IP-Glasma model can be extended under the ansatz that the proton has a substructure with three gluon hot spots and then constraining their distribution with one additional free parameter fixed to match HERA $e + p$ data.

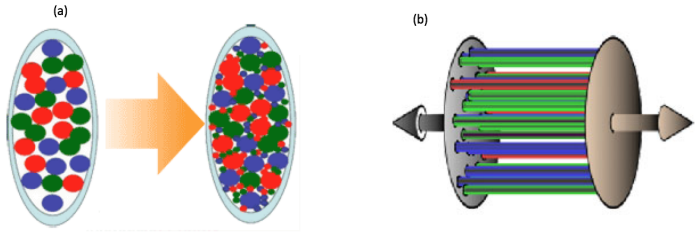

Figure 10: Panel (a) A schematic illustration of gluon saturation as as heavy ions are accelerated to near light speed. Panel (b) When the ions collide, they pass through each other and the gluons interact to form "flux tubes", which is the initial state of quark-gluon plasma (QGP), called a glasma.

Figure 11 shows an example for the initial density profile simulated by IP-Glasma on panel (a) and MC-Glauber on panel (b). The density profile

from IP-Glasma is more finer and more spiky, implying stronger fluctuations of anisotropy.

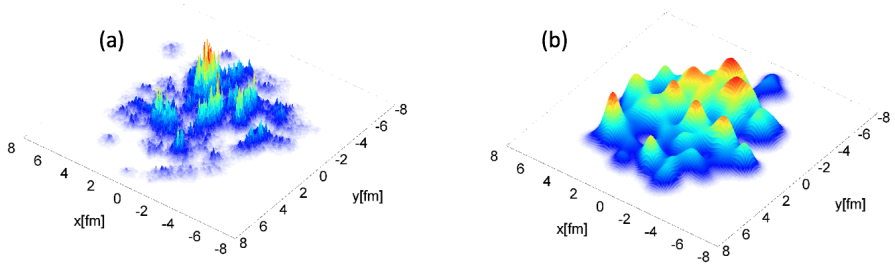

Figure 11: Initial energy density (arbitrary units) in the transverse plane from IP-Glasma (a), and MC-Glaube (b) models [19].

2.3.3 Medium response

The hydrodynamic prediction of harmonic flow are expected to be a function of the eccentricities

$$\boldsymbol{V}_n = \boldsymbol{V}_n(\varepsilon, \alpha) \tag{14}$$

where ε denotes a set of (complex) eccentricities ($\varepsilon_n = \epsilon_n e^{in\Phi_n^*}$) of different orders and α represents the medium dynamic properties, e.g. η/s. However the function format is not known *a priori* from first-principle calculation, there is mounting evidence from numerical hydrodynamic simulation suggesting

$$\boldsymbol{V}_2 \approx \kappa_2 \varepsilon_2 \tag{15}$$

$$\boldsymbol{V}_3 \approx \kappa_3 \varepsilon_3 \tag{16}$$

$$\boldsymbol{V}_4 \approx \kappa_4 \varepsilon_4 + \kappa_{422} \varepsilon_2^2 \tag{17}$$

$$\boldsymbol{V}_5 \approx \kappa_5 \varepsilon_5 + \kappa_{523} \varepsilon_2 \varepsilon_3 \tag{18}$$

$$\boldsymbol{V}_6 \approx \kappa_6 \varepsilon_6 + \kappa_{633} \varepsilon_3^2 + \kappa_{624} \varepsilon_2 \varepsilon_4 + \kappa_{6222} \varepsilon_2^3 \tag{19}$$

where the dependence on medium dynamical properties is absorbed in $\kappa(\alpha)$ [16, 17]. The effect of fluid response is suppressed by viscosity in hydrodynamics. And higher order harmonics get stronger suppression. Note, this expansion

is truncated by keeping only the leading contribution and the terms are also constrained by the rotation invariance of n-th order event plane.

For the high order harmonic flow $\boldsymbol{V}_n$, it is easy to write $\boldsymbol{V}_n = \boldsymbol{V}_n^{\mathrm{L}} + \boldsymbol{V}_n^{\mathrm{NL}}$ for $(n > 3)$. The linear component is a response to eccentricity of the same order, $\boldsymbol{V}_n^{\mathrm{L}} \propto \varepsilon_n$, while the nonlinear components gets contribution from mixture of lower order eccentricities. and the linear and nonlinear component are usually assumed to be uncorrelated on an event basis. Consequently, one expect this event averaged correlation is zero [23]:

$$\left\langle \boldsymbol{V}_n^{\mathrm{L}} (\boldsymbol{V}_n^{\mathrm{NL}})^* \right\rangle = 0 \tag{20}$$

2.4 Experimental methods

In flow paradigm, particles are emitted independently from the azimuthal distribution

$$f(\phi) = 1 + \sum_{n=1}^{\infty} 2v_n \cos[n(\phi - \Phi_n)] \tag{21}$$

and they are all correlated to the same set of event planes Φ_n, which lead to a global azimuthal correlation among all the flow-driven particles. Thus, multi-particle azimuthal correlation encode information about flow harmonics. Two-, four-, six- and eight-particle correlation will be discussed here.

2.4.1 flow and non-flow

Since each particle is emitted independently, the joint multivariate particle density function (p.d.f.) of the azimuthal angles of m particles can factorize into product of single particle density function

$$f(\phi_1, \phi_2, \cdots, \phi_m) = f(\phi_1) f(\phi_2) \cdots f(\phi_m) \tag{22}$$

This factorization relationship is the the foundation for multi-particle correlation. For a event with N particles produced, the m-particle correlation is

defined as:

$$\begin{aligned}\langle m\rangle_{n_1,n_2,\cdots,n_m} &= \left\langle e^{i(n_1\phi_1+n_2\phi_2+\cdots+n_m\phi_m)}\right\rangle \\ &= \left\langle e^{in_1\phi_1}\right\rangle\left\langle e^{in_2\phi_2}\right\rangle\cdots\left\langle e^{in_m\phi_m}\right\rangle \\ &= v_{n_1}e^{in_1\Phi_{n_1}}v_{n_2}e^{in_2\Phi_{n_2}}\cdots v_{n_m}e^{in_m\Phi_{nm}}\end{aligned} \tag{23}$$

where $\langle\rangle$ denotes average over the set of all possible m-particle combinations in one event.

A heavy-ion collision also have non-flow processes, e.g. jet fragmentation, which produced few particles together in a correlated manner. Total momentum conservation of the non-flow process leads to correlation among these produced particles in momentum and in space. For these non-flow processes, the p.d.f. of correlated particle cannot factorize. Since the detected particles include both flow and non-flow particles, Equation (22) is modified as

$$f(\phi_1,\phi_2,\cdots,\phi_m) = f(\phi_1)f(\phi_2)\cdots f(\phi_m) + f_c(\phi_1,\phi_2,\cdots,\phi_m) \tag{24}$$

where the subscript c denotes the non-flow induced correlation and the m-particle correlation contains contribution from non-flow

$$\langle m\rangle_{n_1,n_2,\cdots,n_m} = v_{n_1}e^{in_1\Phi_{n_1}}v_{n_2}e^{in_2\Phi_{n_2}}\cdots v_{n_m}e^{in_m\Phi_{nm}} + \text{nonflow} \tag{25}$$

2.4.2 Two-particle azimuthal correlation

Two-particle azimuthal correlation (2PC) measures pair distribution of two particles as a function of the relative azimuthal difference $\Delta\phi = \phi_a - \phi_b$ and pseudorapidity difference $\Delta\eta = \eta_a - \eta_b$. Here the particles a and b are commonly referred to as *trigger* and *associated* particle respectively. Measurements in different collisions systems have revealed the *ridge* phenomenon [24–28]: enhanced production of particle pairs at small azimuthal angle separation, $\Delta\phi$, extended over a wide range of pseudorapidity separation, $\Delta\eta$. The ridge reflects multi-parton dynamics early in the collision and has generated significant interest in the high-energy physics community. In A+A collisions, ridge is interpreted as evidence of collective flow (see eq. (28)).

Figure 12(a) shows an example of the correlation function $C(\Delta\eta, \Delta\phi)$, measured in 0-5% centrality in Pb+Pb collisions by ATLAS. The correlation function gets contribution from both flow and non-flow and exhibits a very rich structure in $\Delta\eta$ and $\Delta\phi$.

Firstly, a sharp peak arises, localized near $(\Delta\phi \sim 0, \Delta\eta \sim 0)$. This peak is only significant within a small $\Delta\eta$ interval (short-range). Such a peak is caused by particle correlations from single jet fragmentation, resonance decay, and so forth. For example, particles from a single fragmenting jet are in a cone, narrowed in (η, ϕ), inter-jet correlations are thus confined at small $\Delta\phi$ and $\Delta\eta$.

Secondly, ridge-like structures are observed at $\Delta\phi \sim 0$ (near-side) and $\Delta\phi \sim \pi$ (away side). Since ridge is almost invariant along $\Delta\eta$, $C(\Delta\phi, \Delta\eta)$ is usually projected into a 1D function along $\Delta\phi$ by averaging over $|\Delta\eta| > 2$.

$$C(\Delta\phi) = \frac{\int d|\Delta\eta| C(|\Delta\eta|, \Delta\phi)}{\int d|\Delta\eta|} \tag{26}$$

where the cut $|\Delta\eta| > 2$ is sufficiently wide to avoid the near-side peak. It is then conveniently to decompose the 1D correlation function into Fourier series:

$$C(\Delta\phi) \propto 1 + 2\sum_{n=1}^{\infty} v_{n,n}^{a,b} \cos(n\Delta\phi) \tag{27}$$

Figure 12(b) shows the $C(\Delta\phi)$ along with the individual $v_{n,n}$ components and their sum from Fourier fit components. The azimuthal structure can be quite well described by including modulations up to order 6. In the flow paradigm, using Equations (21) and (22), one can show these sinusoidal modulations $(\cos(n\Delta\phi))$ arises solely from the flow-induced modulations on singe-particle

distribution

$$
\begin{aligned}
C(\Delta\phi) &\propto \int \frac{dN^a(\phi_1)}{d\phi_1}\frac{dN^b(\phi_2)}{d\phi_2}\delta(\phi_1-\phi_2-\Delta\phi)d\phi_1 d\phi_2 \\
&\propto \int (1+\sum_{n=1}^{\infty} 2v_n^a \cos[n(\phi_1-\Phi_n)]) \times (1+\sum_{n=1}^{\infty} 2v_n^b \cos[n(\phi_2-\Phi_n)]) \\
&\times \delta(\phi_1-\phi_2-\Delta\phi)d\phi_1 d\phi_2 \\
&= 1+2\sum_{n=1}^{\infty} v_n^a v_n^b \cos(n\Delta\phi)
\end{aligned}
\tag{28}
$$

Thus the Fourier coefficients of two-particle correlations factorize into product of single particle flow harmonics

$$
v_{n,n}^{a,b} = v_n^a \times v_n^b \tag{29}
$$

Especially, when particle a and b are selected with the same criteria, e.g. p_{T}, $v_{n,n} = v_n^2$.

Lastly, the $|\Delta\eta| > 2$ cut cannot remove non-flow correlations extended in $\Delta\eta$ completely. These non-flow correlations are usually at $\Delta\phi \sim \pi$ and leads to a much broader peak on the away side. Their effects are found to be negligible in central and mid-central A+A collisions. These correlations are mostly caused by dijets (back-to-back jets), which are emitted back to back in azimuth to conserve transverse momentum, but not constrained for their longitudinal momenta. Therefore, the dijet correlations are around $\Delta\phi \sim \pi$ but unbounded in $\Delta\eta$ direction. In general, the dijet correlation has its strength proportional to the inverse of the number of produced particles, $\sim 1/N$, so its contribution decreases from peripheral to central collisions. On the contrary, in small systems, these dijet correlations are found to be significant, which will be introduced in Section 2.5 and detailed in Section 6.

2.4.3 Multi-particle correlation

The multi-particle cumulants are constructed from m-particle correlations. They can probe the event-by-event fluctuation of a single flow harmonic v_n, as well as the correlated fluctuations between two flow harmonics, v_n and

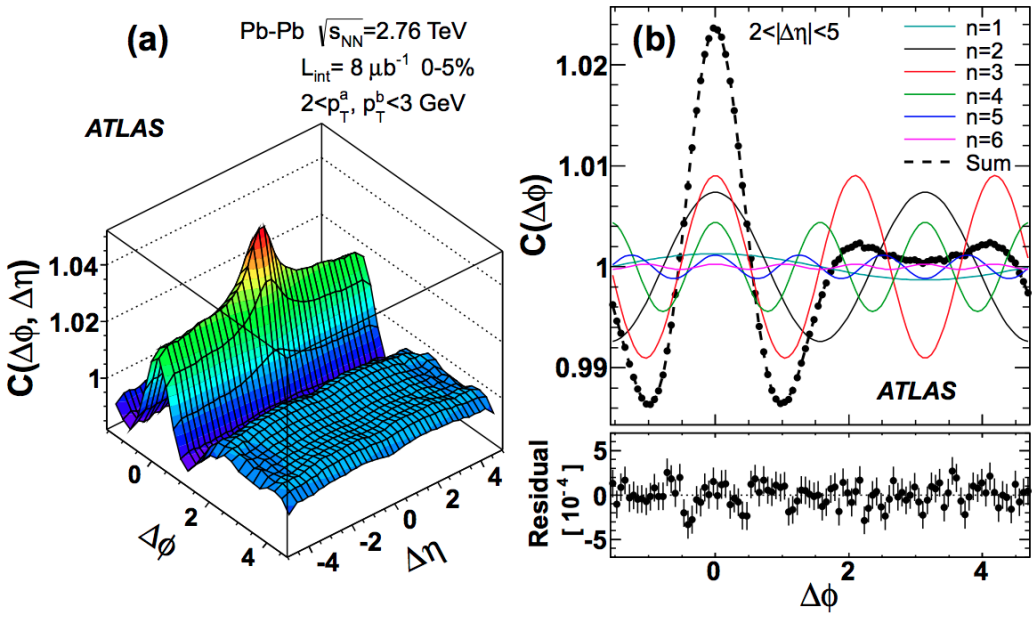

Figure 12: Left:the two particle correlation function measured in 0-5% central Pb+Pb collisions at the LHC using the ATLAS detector. The correlation function is plotted over the range $-\pi/2 < \Delta\phi < 3\pi/2$; the periodicity of the measurement requires $C(\Delta\eta, 3\pi/2) = C(\Delta\eta, -\pi/2)$. Right: The 1D correlation function $C(\Delta\phi)$ for the region with $|\Delta\eta| > 2.0$, overlaid with contributions from the individual $v_n^2 (n < 6)$ components and their sum. The smaller panel on the right show the deviation of the data points from the Fourier sum.

v_m. These event-by-event fluctuations are often represented by probability density distributions $p(v_n)$ and $p(v_n, v_m)$, respectively.

Probing $p(v_n)$: cumulants

Further insight into the ridge phenomenon is obtained via a multi-particle correlation technique, known as cumulants, involving three or more particles [29–31]. Multi-particle cumulants utilize correlations among of $2, 4, 6, ..., m$

particles to subtract non-flow correlations among only $m-2$ particles sequentially, where $m = 2k$ is an even number.

For an event with N particles, we first define the single-event two-and four-particle azimuthal correlations for the n-th order harmonic

$$\langle 2 \rangle_n \equiv \frac{1}{P_{N,2}} \sum_{i \neq j} e^{in(\phi_i - \phi_j)} = \left\langle v_n e^{in\Phi_n} v_n e^{-in\Phi_n} \right\rangle = \left\langle v_n^2 \right\rangle \tag{30}$$

$$\langle 4 \rangle_n \equiv \frac{1}{P_{N,4}} \sum_{i \neq j \neq k \neq l} e^{in(\phi_i + \phi_j - \phi_k - \phi_l)} = \left\langle v_n^4 \right\rangle \tag{31}$$

where $P_{n,m} = N!/(N-m)!$ and the sum runs over all combinations in which all indices are taken different. Note in data analysis, each track is assigned a weight to correct detector inefficiencies, the sum then becomes a weighted sum. Generalization to six and eight particle correlations, $\langle 6 \rangle_n$ and $\langle 8 \rangle_n$, can be derived in similar manner.

The cumulants $c_n\{m\}$ are then defined as combinations of these correlations averaged over many events [30]

$$c_n\{2\} = \left\langle \left\langle e^{in(\phi_1 - \phi_2)} \right\rangle \right\rangle = \langle \langle 2 \rangle_n \rangle \tag{32}$$

$$\begin{aligned} c_n\{4\} &= \left\langle \left\langle e^{in(\phi_1 - \phi_2 + \phi_3 - \phi_4)} \right\rangle \right\rangle - \left\langle \left\langle e^{in(\phi_1 - \phi_2)} \right\rangle \right\rangle \left\langle \left\langle e^{in(\phi_3 - \phi_4)} \right\rangle \right\rangle \\ &\quad - \left\langle \left\langle e^{in(\phi_1 - \phi_4)} \right\rangle \right\rangle \left\langle \left\langle e^{in(\phi_3 - \phi_2)} \right\rangle \right\rangle \\ &= \langle \langle 4 \rangle_n \rangle - 2 \langle \langle 2 \rangle_n \rangle^2 \end{aligned} \tag{33}$$

$$c_n\{6\} = \langle \langle 6 \rangle_n \rangle - 9 \langle \langle 4 \rangle_n \rangle \langle \langle 2 \rangle_n \rangle + 12 \langle \langle 2 \rangle_n \rangle^3 \tag{34}$$

$$\begin{aligned} c_n\{8\} &= \langle \langle 8 \rangle_n \rangle - 16 \langle \langle 6 \rangle_n \rangle \langle \langle 2 \rangle_n \rangle + 18 \langle \langle 4 \rangle_n \rangle \\ &\quad + 144 \langle \langle 4 \rangle_n \rangle \langle \langle 2 \rangle_n \rangle^2 - 144 \langle \langle 2 \rangle_n \rangle^4 \end{aligned} \tag{35}$$

here the outer $\langle\rangle$ means average over events which have similar multiplicities. If one assume, v_n is a constant, the single particle flow coefficients $v_n\{2k\}$ are then calculated from these cumulants, e.g

$$v_n\{2\} \equiv \sqrt{c_n\{2\}}; \;\; v_n\{4\} \equiv \sqrt[4]{-c_n\{4\}}; \;\; v_n\{6\} \equiv \sqrt[6]{c_n\{6\}/4}; \;\; v_n\{8\} \equiv \sqrt[8]{-c_n\{8\}/33} \tag{36}$$

The multi-particle cumulants probe the event-by-event fluctuation of a single flow harmonic v_n. These event-by-event fluctuations are often represented by probability density distributions. The two components of flow vector $\vec{v}_n = (v_{n,x}, v_{n,y}) = (v_n \cos(n\Phi_n), v_n \sin(n\Phi_n))$ are generally assumed to have independent Gaussian fluctuations respectively, as studies shown in Monte-Carlo Glauber model. It is convenient to write the joint probability distribution of $(v_n \cos(n\Phi_n), v_n \sin(n\Phi_n))$ in compact vector format

$$p(\vec{v}_n) = \frac{1}{2\pi\sigma_{v_n}} e^{-(\vec{v}_n - \vec{v}_n^{\mathrm{RP}})^2/(2\sigma^2_{v_n})} \tag{37}$$

where $\vec{v}_n^{\mathrm{RP}}$ represents the event averaged flow vector, which is associated with the average geometry in the reaction plane and σ_{v_n} reflects the width of the fluctuation. After averaging over the azimuthal direction, the joint p.d.f. is projected to radial direction ($v_n = \sqrt{v^2_{n,x} + v^2_{n,y}}$) and the distribution $p(v_n)$ is found to follow a Bessel Gaussian(B-G) distribution

$$p(v_n) = \frac{v_n}{\sigma^2_{v_n}} e^{-\frac{v_n^2 + (v_n^{\mathrm{RP}})^2}{2\sigma^2_{v_n}}} I_0\left(\frac{v_n^{\mathrm{RP}} v_n}{\sigma^2_{v_n}}\right) \tag{38}$$

Under the B-G distribution, then these flow $v_n\{2k\}$ from cumulants have a particularly simple form

$$\begin{aligned} v_n\{2k\} &= \sqrt{(v_n^{\mathrm{RP}})^2 + 2\sigma^2_{v_n}}; \quad k = 1 \\ v_n\{2k\} &= v_n^{\mathrm{RP}}; \quad k > 1 \end{aligned} \tag{39}$$

These measurements have been particularly powerful since they allow extraction of both the event averaged flow harmonics and the event-by-event variance σ^2. Figure 13 shows the $v_2\{2k\}$ from cumulants of different orders as a function of p_{T} measured in 40-45% Pb+Pb collisions at ATLAS [32]. The $v_2\{2\}$ are larger than the higher order cumulants through all p_{T} ranges, while the higher order cumulants are consistent which supports the B-G distribution assumption.

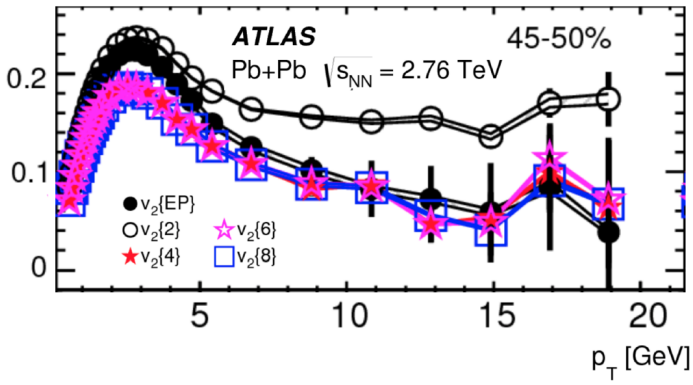

Figure 13: The $v_n\{2k\}$ from 2 particle, 4 particle, 6 particle and 8 particle cumulants as a function of p_{T} measured in 40-45% Pb+Pb collisions at ATLAS [32].

Probing $p(v_n, v_m)$: symmetric cumulants

Based on the cumulant framework, novel correlation between mixed orders harmonics v_n and v_m is proposed. The observable is called symmetric cumulant $sc_{n,m}\{4\}$, in which $\{4\}$ denotes the observable is in fact a four-particle correlator. $sc_{n,m}\{4\}$ is defined as the four-particle cumulant format to suppress non-flow correlations

$$\begin{aligned} sc_{n,m}\{4\} &= \left\langle\left\langle e^{i(m\phi_1+n\phi_2-m\phi_3-n\phi_4)}\right\rangle\right\rangle - \left\langle\left\langle e^{im(\phi_1-\phi_3)}\right\rangle\right\rangle\left\langle\left\langle e^{in(\phi_2-\phi_4)}\right\rangle\right\rangle \\ &= \left\langle v_n^2 v_m^2\right\rangle - \left\langle v_n^2\right\rangle\left\langle v_m^2\right\rangle \end{aligned} \tag{40}$$

This symmetric cumulant is unaffected by the event plane Φ_n and Φ_m and is zero if flow amplitude v_n and v_m are uncorrelated in each event. So it directly probes the joint p.d.f. $p(v_n, v_m)$.

Figure 14(a) shows $sc_{4,2}\{4\}$ and $sc_{3,2}\{4\}$ as a function of centrality in Pb+Pb by ALICE [33]. $sc_{4,2}\{4\}$ is positive through all centralities, suggesting a positive correlation between the event-by-event fluctuations of v_2 and v_4, while $sc_{3,2}\{4\}$ is negative, suggesting a negative correlation between v_2 and v_3. In other words, these observations suggest that for an event, in which v_2 is larger than the average $\langle v_2\rangle$ in this centrality, it is more possi-

ble to find harmonics v_4 larger than the $\langle v_4 \rangle$ and v_3 smaller than $\langle v_3 \rangle$. The data from ALICE is also compared to calculations from AMPT model and hydrodynamic model with three different setup of η/s: constant value and temperature dependent of $\eta/s(T)$ with different parametrization [34]. The hydrodynamic model can qualitatively capture the the centrality dependence of $sc_{4,2}\{4\}$ and $sc_{3,2}\{4\}$ but not quantitatively. While, the same model can captures quantitatively the centrality dependence of the individual v_2, v_3, and v_4 harmonics with a precision better than 10% in the central and mid-central collisions [34]. In the hydrodynamic model, $\mathrm{sc}_{n,m}\{4\}$ are also found to be very sensitive to the transport coefficient, η/s. Therefore one can conclude symmetric cumulant provide a better constrain on theoretical modeling than the single flow harmonic v_n. On the other hand, the transport model AMPT generally predicts the sign of but not the magnitude of $sc_{4,2}\{4\}$ and $sc_{3,2}\{4\}$. A study based on AMPT also suggest these observables are sensitive to the cross-section of partonic and hadronic interaction in the model.

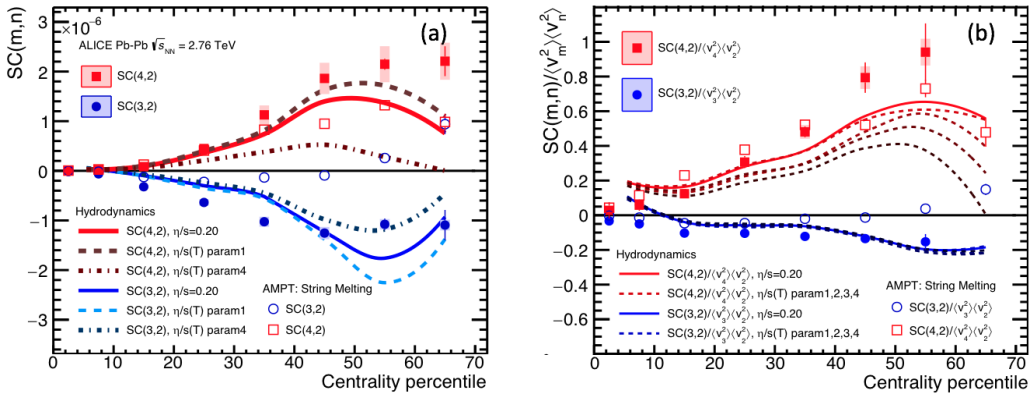

Figure 14: Panel(a): comparison of the SC(4,2) and SC(3,2) to hydrodynamic model from Ref. with constant and temperature dependent η/s and AMPT model. Panel(b): results divided by $\langle v_n \rangle \langle v_m \rangle$ obtained from two-particle correlations. Figure taken from [33].

Figure 14(b) shows the same information with Figure 14(a), but $\mathrm{sc}_{n,m}\{4\}$ are normalized by $\langle v_n^2 \rangle \langle v_m^2 \rangle$ from two-particle correlation method. The nor-

malization procedure removes the influence from centrality dependence of v_n and v_m. In the normalized situation, $sc_{3,2}\{4\}$ is find to be less sensitive to η/s, which indicates it is more related to the initial conditions and less related to medium properties. While the normalized $sc_{4,2}\{4\}$ is both sensitive to initial conditions and medium properties since v_4 get non-linear contribution of v_2^2 during the cumulant expansion of the fluid.

2.5 Flow in small system

With the success of establishing the perfect QGP fluid paradigm in heavy ion (A+A) collisions, a big question still under intense debate is: how small can a QGP fluid system be in size? The small collision systems, such as *pp*, *p*+Pb, were thought to be too small to provide volume and number of particles sufficient for a QGP to form and equilibrate. However, recent studies found that collective effects in small systems are very similar to these effects in A+A system. A key question is whether the these collective effects have the same origin with A+A systems where QGP fluid is formed and anisotropic flow is the final-state hydrodynamic response to the initial transverse collision geometry [35] or these collective effects reflect the initial momentum correlation from gluon saturation effects, which are uncorrelated with spatial anisotropy [36].

Here we give a brief summary of some experimental measurements in small system in the rest of this section.

Ridge is everywhere

Two-particle correlation analysis in high multiplicity *pp* and *p*+Pb exhibits a visible near side ridge, which is very similar to the peripheral Pb+Pb collisions, as shown on Figure 15. There is a $\cos 2(\Delta\phi)$-like azimuthal structure in the two-particle correlation functions, which is most notably in *p*+Pb and Pb+Pb collisions. These *pp* system has a more pronounced dijet correlations at away side than *p*+Pb and peripheral Pb+Pb. In Section 6, subtraction of

these dijet correlation will be discussed in details.

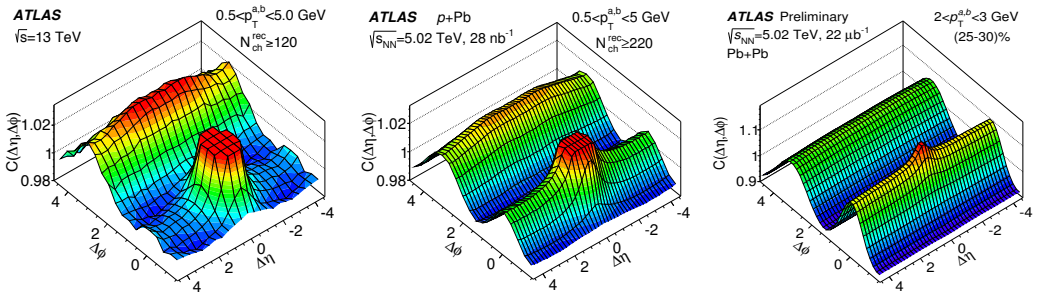

Figure 15: 2D two-particle correlation function in high-multiplicity pp, p+Pb and Pb+Pb collisions at LHC from ATLAS

The ridges are studies in more details to provide more constrain to theoretical interpretation. Figure 16(left column) shows that, in p+Pb system, shape of $v_2(p_{\mathrm{T}})$ and $v_3(p_{\mathrm{T}})$ is very similar to Pb+Pb collisions with same multiplicity range [27]. Basar and Teaney [37] also argue that the $v_n(p_{\mathrm{T}})$ shape in the two collision systems are related to each other by a constant scale factor of K = 1.25 accounting for the difference in their $\langle p_{\mathrm{T}} \rangle$. The rescaled v_n in p+Pb are shown in the right column of Figure 16. The magnitude (y axis) of v_2 of Pb+Pb is also rescaled by 0.66 to approximately match the magnitude of the corresponding p+Pb v_n data, which is due to the difference of elliptic geometry between p+Pb and Pb+Pb collisions. After the scaling, the $v_2(p_{\mathrm{T}})$ shape from the two systems agree well with each other, in particular in the low-p_{T} region (p_{T} < 2–4 GeV) where the statistical uncertainties are small. For $v_3(p_{\mathrm{T}})$ we also see a roughly good matching without the need of scaling on flow magnitude since v_3 is driven by fluctuation.

Qualitative agreement between calculation and experimental data has been shown in p_{T} differential v_2 on Figure 17. However the viscous hydrodynamics interpretation may be questionable due to large pressure gradients that are present for a significant fraction of the space-time evolution. On the other hand, an alternative model can also reproduce the $v_2(p_{\mathrm{T}})$ features in p+Pb, which computes single and double inclusive gluon distributions in

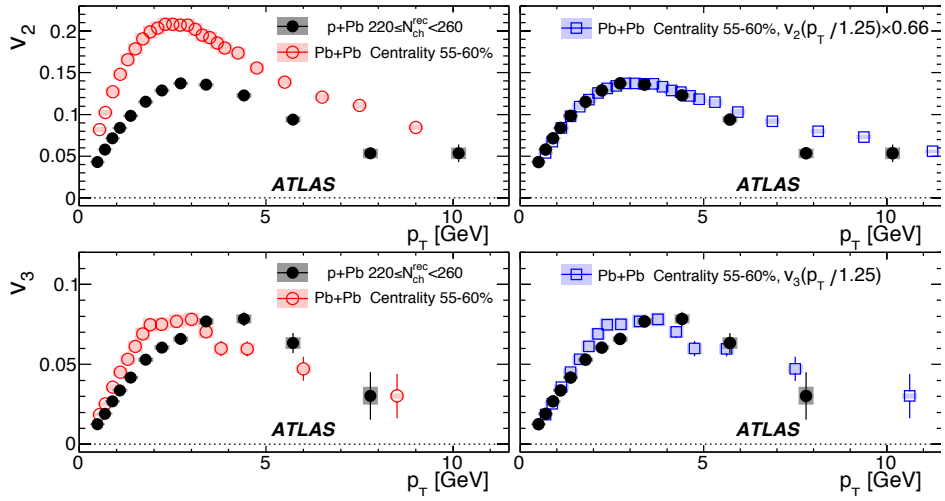

Figure 16: In the left column, shape of $v_2(p_{\mathrm{T}})$ and $v_3(p_{\mathrm{T}})$ for 5.02 TeV p+Pb collisions compared to 2.76 TeV Pb+Pb with similar multiplicity . In the right column, the same Pb+Pb data are rescaled horizontally by a constant factor of 1.25, and the v_2 is also down-scaled by an empirical factor of 0.66 to match the p+Pb data.

classical Yang-Mills simulations, without the need of additional final state interactions [38]. These momentum space anisotropies at early times are uncorrelated with the global spatial anisotropy, in contrast to anisotropies generated by collective flow. It is therefore important to explore if multi-particle correlations at different transverse momentum scales can be understood in part or whole in alternative approaches.

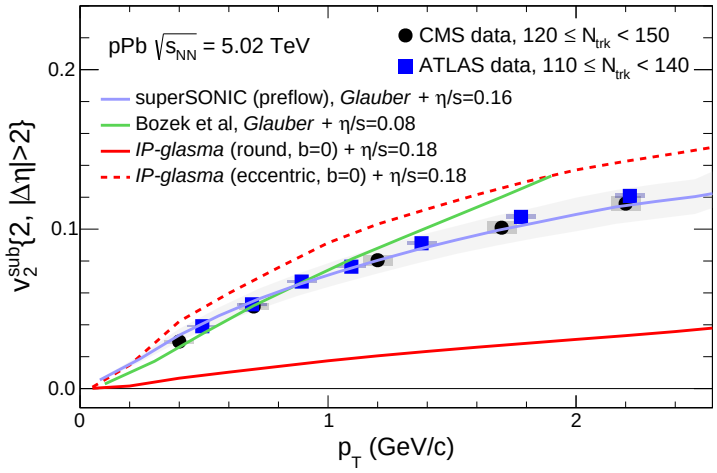

Figure 17: The $v_2(p_T)$ measured in high multiplicty p+Pb at ATLAS ans CMS compared to hydrodynamic model calculation: prediction with MC-Glauber MC Glauber initial condition, results from superSONIC with preflow, and IP-Glasma+MUSIC calculation.

Multi-Particle Correlations

To understand if the ridge is truly a consequence of collective motion of the nuclear matter, it is important to establish that the collective behavior exists for all particles as a whole, and not just only among few particles. Multi-particle cumulants are measured among two-, four- and eight-particles including the all particles case, Lee-Yang Zero method by CMS collaboration [39]. Figure 18 shows the mass ordering of v_2 from multi-particle cumulant measurements $v_2\{4\}, v_2\{6\}, v_2\{8\}$ and $v_2\{LYZ\}$ in pp and p+Pb systems, which

are very much similar to the peripheral Pb+Pb collisions.

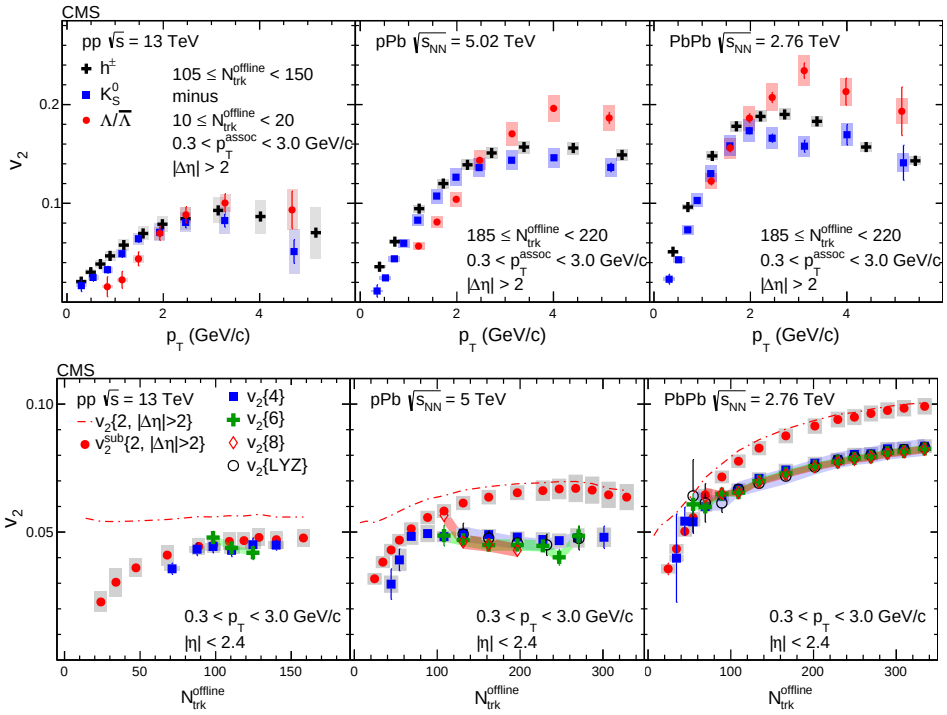

Figure 18: The v_2 data measured in pp, pPb and PbPb collisions at the LHC energies by CMS as a function of p_T for charged particles, K_0^s and Λ particles at high multiplicities from two-particle correlations [39, 40] (top), and as a function of multiplicity for charged particles averaged over $0.3 < p_T < 3$ GeV/c from two- and multi-particle correlations [39] (bottom).

2.6 Topic in this thesis work

In the previous discussion, anisotropic flow is studied in integrated η range, since the system is assumed to be boost-invariant near mid-rapidity ($\eta \approx 0$). However the energy deposition and evolution of the system is three dimensional. Event-by-event fluctuations along η is also very important, which provides information about how the initial density distributed in 3D and helps to constrain the QGP transport properties as well as their temperature

dependence. In Section 4, we will discuss a comprehensive study on flow fluctuations in pseudorapidity in Pb+Pb.

Collective effects in small system need more evidences to clarify its origin. In Sections 5 and 6 we will discuss ATLAS measurement of symmetric cumulants in pp and p+Pb using a slightly different verison of cumulant framework, which is more robust from non-flow contamination. These measurements should provide additional grounds for theoretical studies toward a unified paradigm for the observed collective phenomena in pp, p+A and A+A.

3 The ATLAS detector

The analysis presented in this thesis is based on the data collected by the A Toroidal LHC ApparatuS (ATLAS) detector at the Large Hadron Collider (LHC).

3.1 Large Hadron Collider

A collider is a type of particle accelerator with two beams of particles accelerated and directed against each other, so that the particles collide while flying in opposite directions. For sufficiently high energy upon collisions, a reaction occurs that transforms the particles into other particles. Detecting these products gives insight into the physics involved.

The Large Hadron Collider (LHC) is the world's largest and most powerful particle collider. The collider has four crossing points, around which are positioned seven detectors, one of which is ATLAS detector. The LHC primarily collides proton beams (pp), but it can also use beams of heavy ions, e.g. proton–lead (p+Pb) and lead–lead (Pb+Pb) and xenon-xenon (Xe+Xe).

Particles are boosted to the collision energy step by step at LHC. The accelerator complex at CERN is a succession of machines with increasingly higher energies. Each machine injects the beam into the next one, which takes over to bring the beam to an even higher energy and so on. In the LHC-the last element of this chain-each particle beam is accelerated to the final collision energy. A schematic overview of CERN accelerator complex is shown in Figure 19, where the particles are accelerated as following:

- Proton: An electric field is used to strip hydrogen atoms of their electrons to yield protons. Linac2 accelerates the protons to the energy of 50 MeV. The beam is then injected into the Proton Synchrotron Booster (PSB), which accelerate the protons to 1.4 GeV, followed by the Proton Synchrotron, which pushes the beam to 25GeV. Protons are then sent to Super Proton Synchrotron (SPS) where they are accelerated to 450 GeV. The proton beams are finally transferred to the LHC

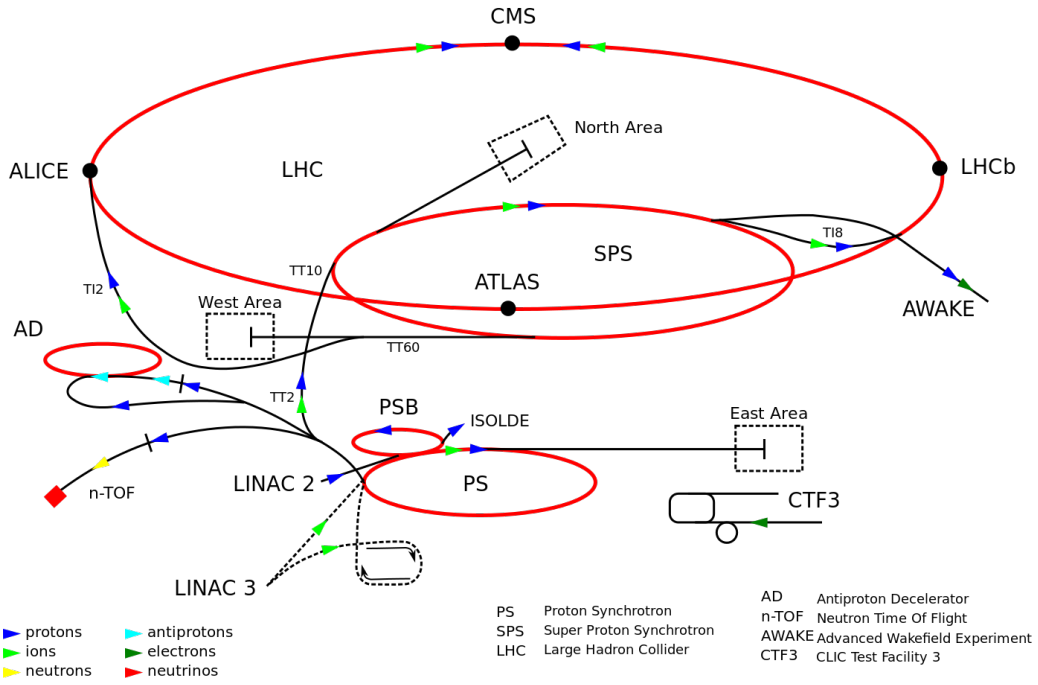

Figure 19: The CERN accelerator complex

(both in a clockwise and an anti-clockwise direction) where they are accelerated to the final energy. Beams then circulate for many hours inside the LHC beam pipes and collisions happens at each crossing point.

- Heavy ions. For example, the lead vapor are firstly ionized to Pb^{54+} by several steps. The Pb^{54+} beam is accumulated and accelerated to 54 Mev/u (energy per nucleon) in the Low Energy Ion Ring (LEIR) which then transfers them to the PS. The PS accelerates the beam to 5.9 Gev/u and sends it to the SPC after first passing it through a foil where Pb^{54+} is fully stripped to Pb^{82+}. The SPC accelerates the ion beam to 177 Gev/u then sends it to the LHC where accelerate it to 2.56 TeV/u or other energy.

3.2 ATLAS detector

The ATLAS (A Toroidal LHC ApparatuS) detector [41] is one of two large general-purpose detectors at the Large Hadron Collider at CERN. The other detector is CMS experiment. These two detectors are designed to achieve the same scientific goals at the energy and intensity frontiers of particle physics. While mainly designed to study pp collisions, its fine granularity and large acceptance made it also an ideal detector to study p+Pb, Pb+Pb and Xe-Xe collisions.

Currently ATLAS heavy ion programs have collected pp data at $\sqrt{s_{\mathrm{NN}}}$ =2.76, 5.02 and 13 TeV; p+Pb data at $\sqrt{s_{\mathrm{NN}}}$ =5.02 and 8.16 TeV; Pb+Pb data at $\sqrt{s_{\mathrm{NN}}}$ = 2.76 and 5.02 TeV and Xe-Xe data at 5.44 TeV.

The detector is nominally symmetric in beam direction with a full coverage in azimuth. The four major components of the ATLAS detector is shown on Figure 20: the Inner Detector, the Calorimeter, the Muon Spectrometer and the Magnet System. Each of these is in turn made of small modules. The detectors are functional complementary: the Inner Detector tracks charged particles, the calorimeters measure the energy of easily stopped particles, and the muon system provides measurements of highly penetrating muons. The two magnet systems bend charged particles in the Inner Detector and the Muon Spectrometer, allowing their momenta to be measured.

In the following, the ATLAS coordinate system will be used. The nominal interaction point is defined as the origin of a right-handed coordinate system. The beam direction defines the z-axis and the $x-y$ plane is transverse to it. The positive z direction is defined as pointing to the "A" side of the detector and negative z direction points to the "C" side. The x-axis is defined to be horizontal direction with positive x direction points to the center of the LHC ring. The y-axis is the vertical direction with positive y direction points upwards.

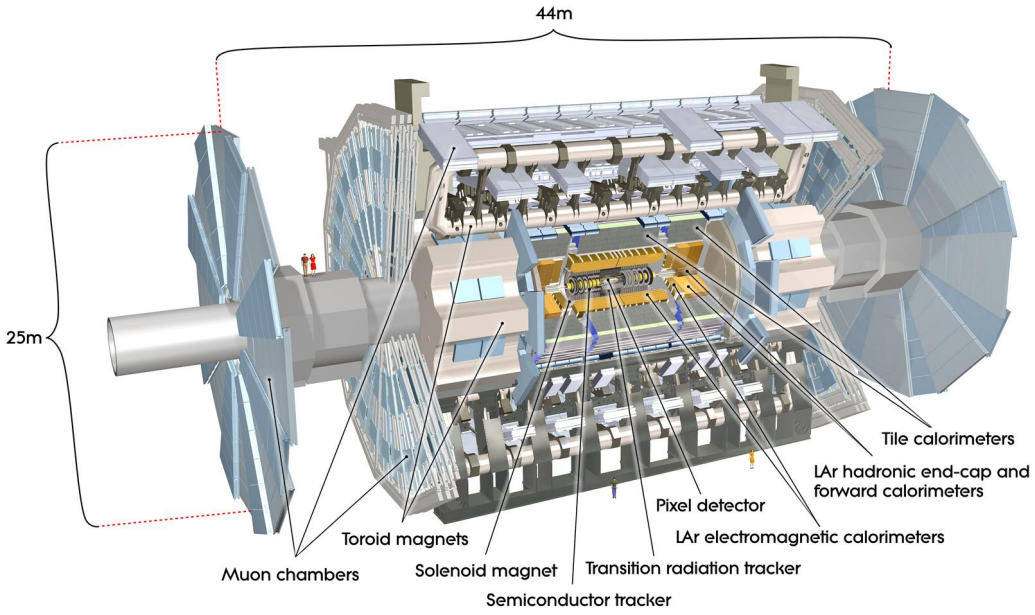

Figure 20: Main subsystems of the ATLAS detector

3.2.1 Inner detector

The ATLAS Inner Detector(ID) is a composite tracking system located in the center of ATLAS detector. It is the first part of ATLAS to see the decay products of the collisions. The ID is used to reconstruct tracks of each charged particle via the space point positions. Once tracks are reconstructed, they can provide the momentum information of each particle and can help to determine the collision vertex as a whole. The ID occupies a cylindrical volume around the detector center spanning ±3512mm in the z direction and 1150 mm in radius, providing full azimuthal coverage and $|\eta| < 2.5$. There are three complementary sub-detectors (from innermost layer): the Pixel Detector, the SemiConductor Tracker (SCT) and the Transition Radiation Tracker (TRT). The Pixel and SCT detectors covers region $|\eta| < 2.5$, while TRC covers $|\eta| < 2$. Relevant features are described briefly below; full details can be found in [42]. Each of the three sub-detectors is divided into barrel (detector layers parallel to the beam pipe) and an end-cap modules (detector layers perpendicular to beam-pipe). Figure 21 shows a scheme of the ID barrel being crossed by one high-energy particle, labeled and with dimensions. Figure 22 shows the dimensions of the various sub-detectors and the typical detector layers that 10 tracks at various η traverse.

The Pixel Detector

The detector is the first detector each flying track will penetrate through, providing three space point measurements per track over the full acceptance. The pixel detector contribute to determination of the impact parameter and detection of short lived particles. The pixel detector is made up of three concentric cylindrical detectors in the barrel region and three end-cap disks each in the forward and backward regions. Typically three pixel layers are crossed by each track. The detector a very high granularity, consisting of 1744 silicon pixel module , each having 47232 pixels, most of $50 \times 400 \mu m^2$ for a total of approximately 80.4 million readout channels. This extremely fine granularity is needed in the pixel detector due to its proximity to the

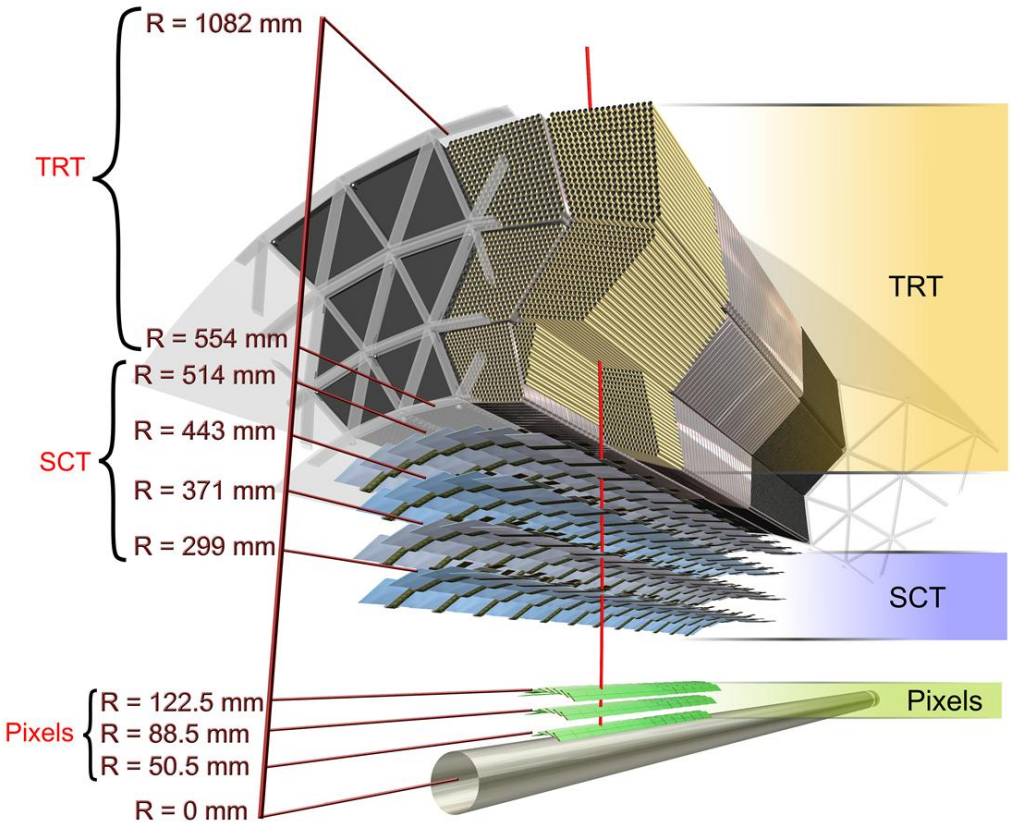

Figure 21: Scheme of the ATLAS inner detector barrel being crossed by one high-energy particle, labeled and with dimensions.

interaction point. Hits in a pixel are read out if the signal exceeds a tunable threshold.

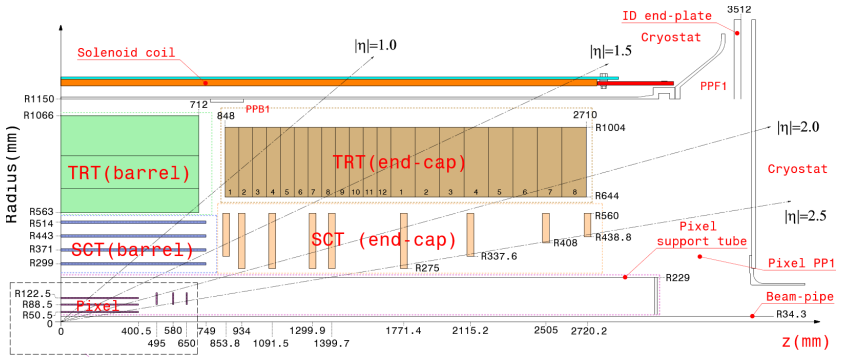

Figure 22: Quarter-section of the ATLAS inner detector showing the major detector elements along with their dimensions. Also shown are the typical number of detector elements that tracks at different η have to cross.

The SemiConductor Tracker (SCT)

The SCT system is designed to provide eight strip measurements (four space-points) per track originating in the intermediate radial range, contributing to the measurement of momentum, impact parameter and vertex position. The detector consists of 4088 modules of silicon-strip detectors arranged in four concentric barrels and two end-caps of nine disks each. In the barrel SCT eight layers of silicon microstrip detectors are approximately parallel to the solenoid field and beam axis, providing precision point in the $R-\phi$ and z coordinates, using small angle stereo to obtain the z-measurement. Each silicon detector has 780 readout strips of 80 μm pitch. The barrel modules are mounted on carbon-fibre cylinders at radii of 30.0, 37.3, 44.7, and 52.0 cm. The end-cap modules are very similar in construction but use tapered strips with one set aligned radially.

The Transition Radiation Tracker (TRT)

The TRT is a drift-tube system and provides robust tracking information with stand-alone pattern recognition capability in the LHC environment, to enhance the momentum resolution by providing track measurement points up

to the solenoid radius and to provide a fast level-2 trigger. The TRT consists of 370,000 cylindrical drift tubes (straws). Each straw (4 mm diameter, made of Kaptonr with a conductive coating) acts as a cathode and is kept at high voltage of negative polarity. The straws in barrel region are arranged in three cylindrical layers while The straws in end-cap regions are radially oriented and arranged in 80 wheel-like modular structure. The TRT straw layout is designed so that charged particles with transverse momentum $p_{\mathrm{T}} > 0.5$ GeV and with pseudorapidity $|\eta| < 2.0$ cross typically more than 30 straws. The TRT provides electron identification capability by employing Xenon gas to detect transition radiation photons created in a radiator between the straws.

3.3 Calorimeters

Calorimeters measure the energy a particle loses as it passes through the detector. It is usually designed to stop entire or "absorb" most of the particles coming from a collision, forcing them to deposit all of their energy within the detector. It consists of metal plates (absorbers) and sensing elements. Interactions in the absorbers transform the incident energy into a "shower" of particles that are detected by the sensing elements. Electromagnetic calorimeters measure the energy of electrons and photons as they interact with matter. Hadronic calorimeters sample the energy of hadrons (particles that contain quarks, such as protons and neutrons) as they interact with atomic nuclei. Calorimeters can stop most known particles except muons and neutrinos.

The components of the ATLAS calorimetry system are: the Liquid Argon (LAr) Calorimeter and the outer Tile Hadronic Calorimeter. Figure 23 is the cut-away view of the ATLAS calorimeters, which covers full azimuthal range over the range $|\eta| < 4.9$ [43]. In the analyses done here, only the Forward Calorimeter (FCal) are used.

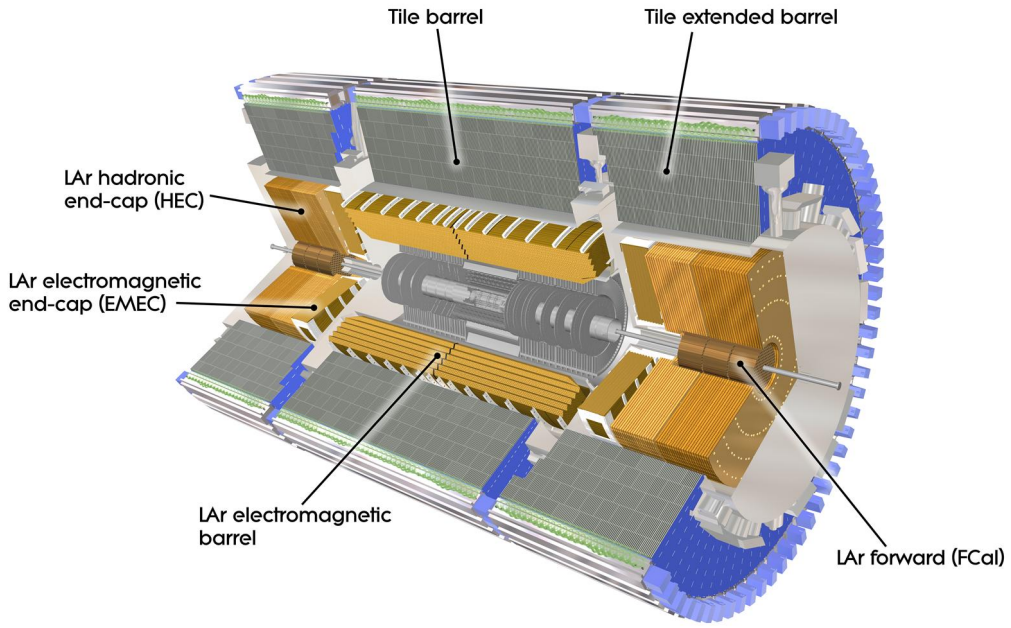

Figure 23: Overview of the ATLAS calorimetry. Near the beam-pipe the tracker is visible, surrounding it is the EM calorimeter and beyond the hadronic calorimeter. Both barrel and end-caps elements are displayed.

3.3.1 Forward Calorimeter

The FCal are a liquid argon, ionization, sampling calorimeters, providing the measurement of transverse energy E_{T} of particles passing it. FCal are located at the two end of ATLAS detector (named FCalA and FCalC), covering $3.2 < |\eta| < 4.9$. Each of the two Forward Calorimeters consists of three modules, one behind the other: FCal1 and FCal2 and FCal3, as shown on Figure 24. The FCal modules are cylindrical in shape with a coaxial hole through which the LHC beams pass. FCal1 module is made of copper is the closest to the Interaction Point and is optimized for electromagnetic measurements. FCal2 and FCal3 modules are are made mostly of tungsten for measurement of hadronic showers.

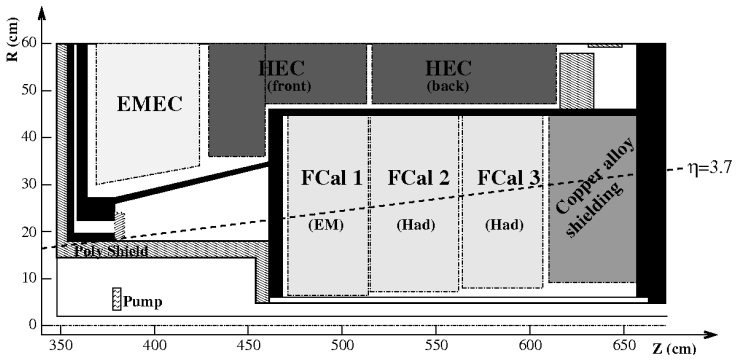

Figure 24: Schematic diagram showing the three FCal modules located in the end-cap cryostat.

In this work, the fine $\eta - \phi$ segmentation of the calorimeter is not used. Instead, the smaller segmentation (cells) are combined to form towers with size 0.1×0.1 in phase space $\eta - \phi$. In regions where the segmentation of the calorimeter cells is larger than 0.1×0.1 (for example last layer of the tile barrel), the cell contributes to multiple towers with its energy divided between the towers. Similarly for the FCal where the segmentations are in $x - y$ rather than in $\eta - \phi$, the $x - y$ cells are combined to make towers of 0.1×0.1 in $\eta - \phi$ with energy of cells that span multiple towers dividend between them. These calorimeter towers are used in the final analyses.

Zero Degree Calorimeter(ZDC)

Zero Degree Calorimeter (ZDC) gets its name as it is located installed on either side (at 140 m downstream, i.e. at zero degrees) of interaction point. Thus ZDC is well separated from the central detector so this minimizes inferences between jet structure and flow.

The primary role of the Zero Degree Calorimeter is in event characterization. Only the neutral particles from the event manage to reach the ZDC as the charged particles are deflected away by the magnetic fields in the beampipe. Thus in Pb+Pb collisions the ZDC the participant number by sampling the spectator neutrons, which is equivalent to measuring the magnitude of the

impact parameter. Each side of the ZDC consists of four modules as shown in the left bottom plot of Figure 25. The detailed design of the modules is shown in the right panel of Figure 25. Each module consists of 11 tungsten plates 10mm thick in the beam direction and steel plates at the front and back (also 10mm thick). Sandwiched between the plates are 1.5 mm diameter quartz rods that run vertically and are viewed by photomultiplier tubes (PMT) from above, via light-pipes. The quartz rods collect Cherenkov radiation from shower particles and guide them to the PMTs. Each PMT is read out by several channels of a Pre Processor Module (PPM). The PPMs are 64 channel, 40 MHz, 10 bit ADCs. The first two ZDC modules on the C side and the second module on the A side also have quartz rods arranged in an $x-y$ grid along the beam-pipe. These can be used for position measurements of the showers. They were however not used in any of the analyses presented here.

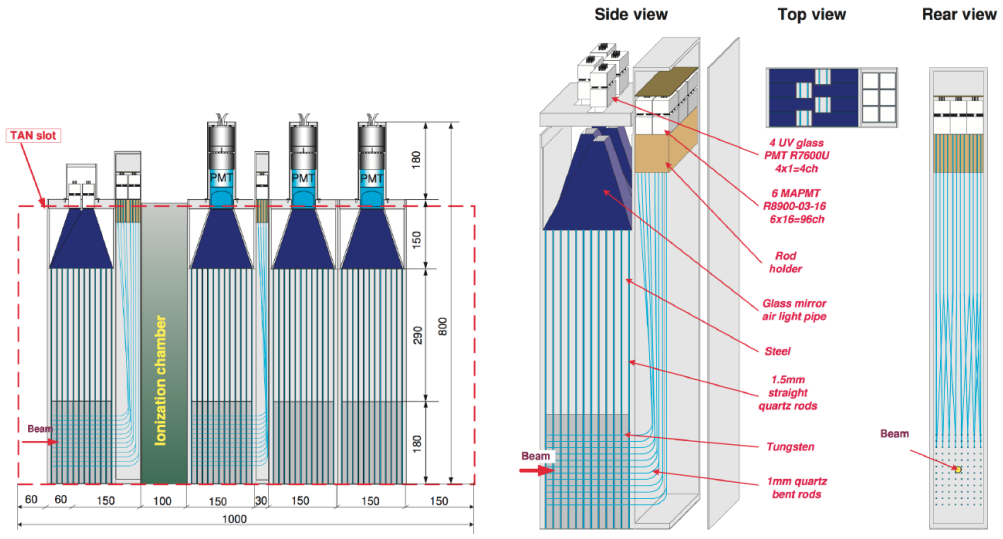

Figure 25: Left Panel:Arrangement of ZDC modules on the side with position sensing EM module. Right Panel: Configuration of the EM module with position sensing rods

3.3.2 Minimum Bias Trigger Scintillator

The minimum bias trigger scintillator (MBTS) provides highly efficient level-1 (L1) triggering on minimum bias (non diffractive inelastic collisions) events in pp, p+Pb and Pb+Pb collisions. The MBTS consist of 2 cm thick polystyrene scintillator disks mounted on both sides of the interaction point just in front of the electromagnetic end-cap at $z = \pm 3.56m$. Each side has an inner and outer ring in η of eight counters in the azimuthal angle ϕ. The outer counters pseudorapidity acceptance is $2.08 \leq |\eta| \leq 2.78$, while the acceptance for inner counters is $2.78 \leq |\eta| \leq 3.75$.

In Run-1, each scintillator has a trapezoidal shape covering an angle of $2\pi/8$. Light collected from each edge of the scintillator is guided to the photomultiplier tubes (PMTs) using wavelength shifting fibers (WLS), as shown on Figure 26. The MBTS signals, after being shaped and amplified in such a way that the pulse amplitude is proportional to the amount of energy deposited in the counter, are fed into leading edge discriminators and sent as 25 ns NIM pulses to the Central Trigger Processor (CTP). The total charge collected as well as the arrival time of the signals are recorded. An MBTS hit is defined as a signal above the discriminator threshold.

In Run-2, it was decided to replace the MBTS with a new detector based on the same ideas and trying to keep the same materials, since the old received a dose in the range of $0.1 \sim 0.4 \times 10^4$ Gy. However, the number of read out channels has to be reduced since they will be in use by the TileCal to instrument the "gap regions".

3.4 Trigger

The trigger system decides whether or not to keep a given collision event for later study, which reduces the event rate from the design bunch-crossing rate of 40 MHz to an average recording rate of a few hundred Hz. In Run-1 (2009-2013),the trigger system has three distinct levels: Level-1 (L1), Level-2 (L2), and the Event Filter (EF). L1 is purely hardware based, built using

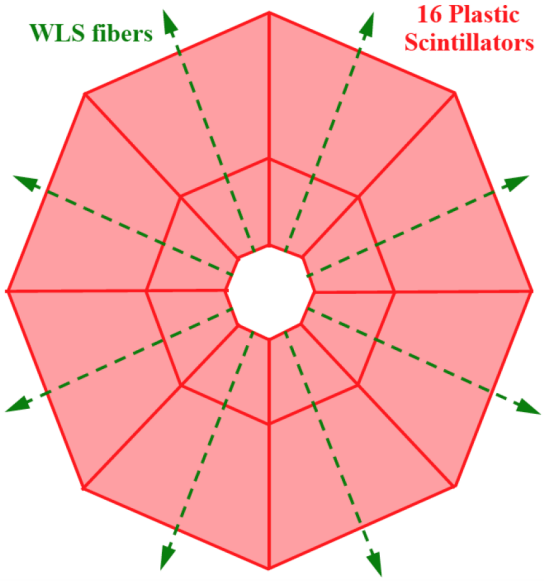

Figure 26: Layout of one of the two MBTS disks in RunI

custom made electronics. L2 and EF are software based running on CPU farms. For Run-2, L2 and EF has been merged into a single event processing HLT farm, which reduces the complexity and allows for dynamic resource sharing between algorithms [44]. A schematic overview of the upgraded Run-2 ATLAS trigger and data acquisition system is shown in Figure 27.

The ATLAS trigger system carries out the selection process in three stages. The Level-1 trigger works on a subset of information from the calorimeter and muon detectors. The decision to keep the data from an event is made less than two microseconds after the event occurs, and the event is then retrieved from pipelined storage buffers. Of 40 million bunch crossings per second, less than 100,000 are kept by the Level-1 trigger.

The Level-2 trigger is a large array of custom processors that analyze in greater detail specific regions of interest identified by the Level-1 system for each event. In the mean time, the full event data is collected into buffers. A few thousand events per second pass Level-2, and have their data passed on

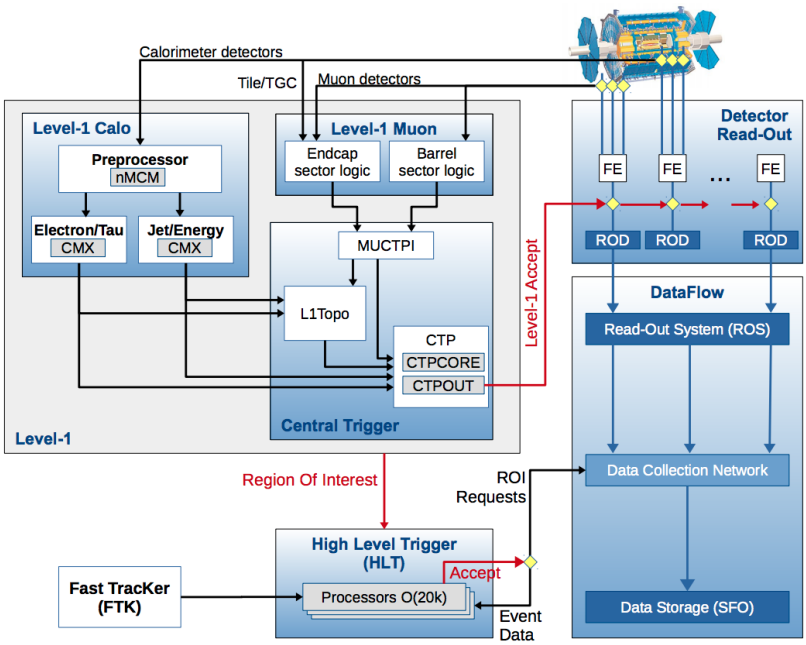

Figure 27: Schematic layout of the ATLAS trigger and data acquisition system in Run-2.

to Level-3.

The Level-3 trigger is a large farm of CPUs which perform a detailed analysis of the full event data. About 200 events per second are left after the Level-3 analysis, and these are passed on to a data storage system for offline analysis.

4 Measurements of longitudinal flow fluctuations in Pb+Pb

For a long time the fireball created in heavy ion collisions is treated as a boost-invariant system and particle production looks the same in all reference frames related by a Lorentz boost in z-axis [7]. Thus study of the QGP dynamics and anisotropic flow has been focused in the transverse directions.

However in recent years, the heavy ion community begin to realize the boost-invariant picture could be broken at the single event level. Recent studies have shown that, due to the longitudinal fluctuations, both flow magnitudes v_n and flow orientation Φ_n may keep constant at different pseudorapidity (η): , i.e. $\boldsymbol{V}_n(\eta_1) \neq \boldsymbol{V}_n(\eta_2)$, as illustrated on Figure 28. And studies from AMPT further indicate the change of $\boldsymbol{V}_n$ along η is not in a purely random way but has some patterns. This phenomena is referred to as *flow decorrelations*. Study of this decorrelation effect over a broad pseudorapidity range can provide a new set of tools for constraining the models for initial states, and for studying the transport properties and evolution dynamics of the QGP.

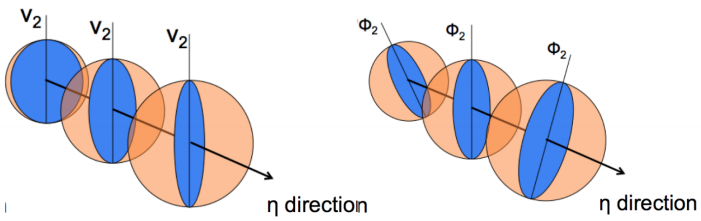

Figure 28: Longitudinal flow fluctuation (a) asymmetry of flow amplitude v_n (b) rotation of event plane Φ_n at different pseudorapidities range.

First measurement of flow decorrelation effect was done by CMS collaboration using a novel observable $r_n(\eta)$, which is defined as a ratio of of two correlations: the flow correlation between η and η_{ref} and the flow correlation

between $-\eta$ and $\eta_{\rm ref}$ [45].

$$r_n(\eta) = \frac{\langle \boldsymbol{V}_n(-\eta)\boldsymbol{V}_n^*(\eta_{\rm ref})\rangle}{\langle \boldsymbol{V}_n(\eta)\boldsymbol{V}_n^*(\eta_{\rm ref})\rangle} \tag{41}$$

This ratio is sensitive to the correlation between η and $-\eta$. The CMS has measured the ratio in Pb+Pb collision and p+Pb collisions for flow harmonics $n = 2-4$. If there is no decorrelation, in the Pb+Pb system, $r_n(\eta)$ equals 1, however, $r_n(\eta)$ is observed to be < 1 and decrease linearly as a function η.

Later on, ATLAS collaboration improved the measurements of flow decorrelation. Firstly, the $r_n(\eta)$ in the CMS measurement, which is effectively the first moment of the correlation between $\boldsymbol{V}_n$ in separate η intervals, is extended to the second and third moments. Secondly, a correlation between four different η intervals is measured to separate the decorrelation from fluctuations of amplitudes v_n and from fluctuations of Φ_n. Thirdly, correlations between harmonics of different order are also measured, e.g. between $\boldsymbol{V}_2$and $\boldsymbol{V}_4$ in different η intervals, to investigate how mode-mixing effects evolve with rapidity. In this way, flow decorrelation is studied involving $\boldsymbol{V}_2 - -\boldsymbol{V}_5$ in Pb+Pb collisions and is studied at two collision energies: $\sqrt{s_{\rm NN}} = 2.76$ and 5.02 TeV. This measurement is the topic of this section.

The majority of work presented in this chapter is Ref [46].

4.1 Methodology

Here, we introduce the set of observables in this analysis, more details are found in Refs. [45, 47].

To begin with, we firstly define the observed per-particle normalized flow vector $\boldsymbol{q}_n$

$$\boldsymbol{q}_n \equiv \frac{\sum_i w_i e^{in\phi_i}}{\sum_i w_i} \ . \tag{42}$$

where the sums run over all particles in a given η interval and $p_{\rm T}$ range of the event, ϕ_i is the azimuthal angle of the $i^{\rm th}$ particle and weight w_i is assigned to accounts for detector non-uniformity and tracking inefficiency.

The single-event quantity, q-vector, is a raw estimate of the true flow vector $\boldsymbol{V}_n$, which also contains statistical smearing $\boldsymbol{s}_n$ (vector) and non-flow $\boldsymbol{c}_n$ (vector) components

$$\boldsymbol{q}_n = \boldsymbol{V}_n + \boldsymbol{s}_n + \boldsymbol{c}_n \tag{43}$$

In general, the three parts are assumed to be uncorrelated in each event. The two-particle correlation can be decomposed as

$$\left\langle \boldsymbol{q}_n^a \boldsymbol{q}_n^{b*} \right\rangle = \left\langle \boldsymbol{V}_n^a \boldsymbol{V}_n^{b*} \right\rangle + \left\langle \boldsymbol{c}_n^a \boldsymbol{c}_n^{b*} \right\rangle + \left\langle \boldsymbol{s}_n^a \boldsymbol{s}_n^{b*} \right\rangle \tag{44}$$

In the absence of non-flow correlation, the correlator averaged over many events can be expressed as:

$$\left\langle \boldsymbol{q}_n^a \boldsymbol{q}_n^{b*} \right\rangle \approx \left\langle \boldsymbol{V}_n^a \boldsymbol{V}_n^{b*} \right\rangle \tag{45}$$

where the statistical fluctuation vanishes after averaging, since they are randomly oriented from event to event. Thus in general, the flow ($\boldsymbol{V}_n$) correlation can be approximated by $\boldsymbol{q}_n$ correlation.

The first observable is constructed using the correlation between k-th moment of the n-th order flow vectors from two different η intervals. And the two windows are selected to be symmetric around $\eta = 0$. The flow correlation is then averaged over many events in a given centrality class to get the ratio $r_{n|n;k}(\eta)$, for $k = 1, 2, 3$:

$$\begin{aligned} r_{n|n;k}(\eta) &= \frac{\langle \boldsymbol{q}_n^k(-\eta) \boldsymbol{q}_n^{*k}(\eta_{\mathrm{ref}}) \rangle}{\langle \boldsymbol{q}_n^k(\eta) \boldsymbol{q}_n^{*k}(\eta_{\mathrm{ref}}) \rangle} \\ &= \frac{\left\langle [v_n(-\eta) v_n(\eta_{\mathrm{ref}})]^k \cos kn(\Phi_n(-\eta) - \Phi_n(\eta_{\mathrm{ref}})) \right\rangle}{\left\langle [v_n(\eta) v_n(\eta_{\mathrm{ref}})]^k \cos kn(\Phi_n(\eta) - \Phi_n(\eta_{\mathrm{ref}})) \right\rangle} \end{aligned} \tag{46}$$

where η_{ref} is the reference pseudorapidity, which is fixed and is common to the numerator and the denominator. The sine(imaginary) terms vanish in the last expression in Equation (46) because $\Phi_n(-\eta) - \Phi_n(\eta_{\mathrm{ref}})$ should be an even function since the positive or negative sign of the value should be random. In essence, the ratio $r_{n|n;k}(\eta)$ quantifies the correlation (decorrelation)

of flow between η and $-\eta$, by comparing each of them to a common reference pseudorapdity window. And from its construction, the observable is effectively a $2k$-particle correlator between two subevents as defined in Ref. [48], and the implementation details of the correlator should be found in Ref [47].

Figure 29 is a cartoon illustrating the construction of $r_{n|n;k}(\eta)$ with ATLAS detector, where $|\eta| < 2.5$ at mid-rapidity is covered by Inner Detector and the $4.0 < |\eta_{\rm ref}| < 4.9$ region is covered by Forward Calorimeter. The pseudorapidity gap between $\eta_{\rm ref}$ and η is large enough to suppress non-flow correlation between the flow vectors in both the numerator and denominator of Equation (46).

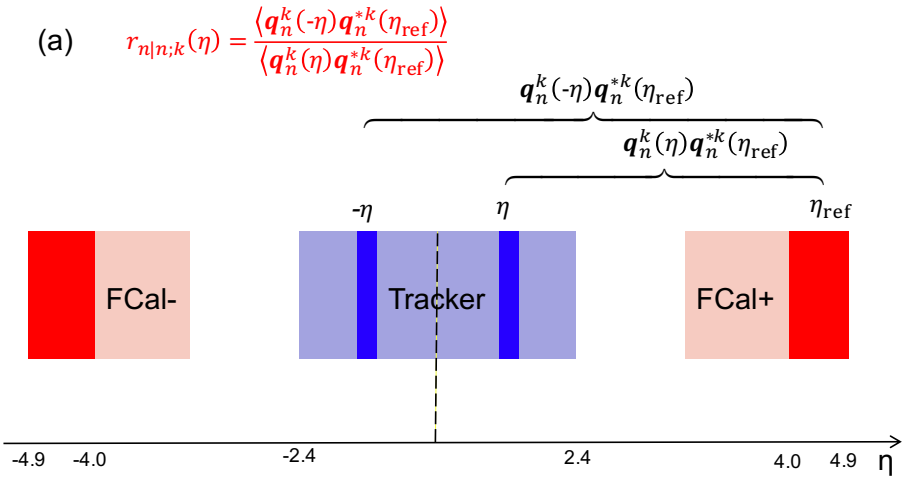

Figure 29: Schematic illustration of procedure for constructing the correlator $r_{n|n;k}(\eta)$ eq. (46). The acceptance coverages for the ATLAS tracker used for η and reference detector used for $\eta_{\rm ref}$ are discussed in Section 3.

If flow harmonics from multi-particle correlations factorize into single-particle flow harmonics, e.g. $\langle \boldsymbol{V}_n^k(\eta)\boldsymbol{V}_n^{*k}(\eta_{\rm ref})\rangle^2 = \langle v_n^{2k}(\eta)\rangle \langle v_n^{2k}(\eta_{\rm ref})\rangle$, then one should expect that $r_{n|n;k}(\eta) = 1$. Therefore, a value of $r_{n|n;k}(\eta)$ different from unity implies a factorization-breaking effect due to longitudinal flow decorrelation, which gets contribution from both the magnitude asymmetry and event plane twist.

In order to estimate the separate contributions of the asymmetry and twist effects, a new observable $R_{n|n;2}(\eta)$ is proposed in Ref [47], which involves correlations of flow vectors in four η intervals and is mainly sensitive to event plane twist effect. The definition of the observable is:

$$R_{n|n;2}(\eta) = \frac{\langle \boldsymbol{q}_n(-\eta_{\rm ref})\boldsymbol{q}_n(-\eta)\boldsymbol{q}_n^*(\eta)\boldsymbol{q}_n^*(\eta_{\rm ref})\rangle}{\langle \boldsymbol{q}_n(-\eta_{\rm ref})\boldsymbol{q}_n^*(-\eta)\boldsymbol{q}_n(\eta)\boldsymbol{q}_n^*(\eta_{\rm ref})\rangle} \tag{47}$$
$$= \frac{\langle v_n(-\eta_{\rm ref})v_n(-\eta)v_n(\eta)v_n(\eta_{\rm ref})\cos n\left[\Phi_n(-\eta_{\rm ref}) - \Phi_n(\eta_{\rm ref}) + \Phi_n(-\eta) - \Phi_n(\eta)\right]\rangle}{\langle v_n(-\eta_{\rm ref})v_n(-\eta)v_n(\eta)v_n(\eta_{\rm ref})\cos n\left[\Phi_n(-\eta_{\rm ref}) - \Phi_n(\eta_{\rm ref}) - (\Phi_n(-\eta) - \Phi_n(\eta))\right]\rangle}$$

where the notation "2" in the subscript indicates that there are two $\boldsymbol{q}_n$ and two $\boldsymbol{q}_n^*$ in the numerator, as well as in the denominator. Seen from Equation (47), the effect of amplitude asymmetry is the same in both the numerator and the denominator, thus this correlator is mainly sensitive to the event-plane twist effects. Figure 30 is a schematic illustration of the relations between different flow vectors with ATLAS detector.

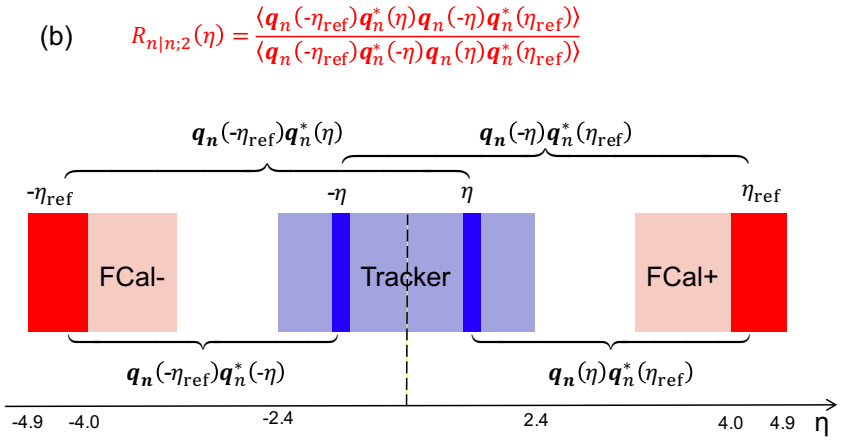

Figure 30: Similar plot as Figure 29 but for correlator $R_{n,n|n,n}(\eta)$.

The study of flow decorrelations can also be extended to between harmonics of different orders. The first type is $\boldsymbol{V}_2\boldsymbol{V}_3$ defined as observable $r_{2,3|2,3}$:

$$r_{2,3|2,3}(\eta) = \frac{\langle \boldsymbol{q}_2(-\eta)\boldsymbol{q}_2^*(\eta_{\rm ref})\boldsymbol{q}_3(-\eta)\boldsymbol{q}_3^*(\eta_{\rm ref})\rangle}{\langle \boldsymbol{q}_2(\eta)\boldsymbol{q}_2^*(\eta_{\rm ref})\boldsymbol{q}_3(\eta)\boldsymbol{q}_3^*(\eta_{\rm ref})\rangle} = \frac{\langle \boldsymbol{V}_2(-\eta)\boldsymbol{V}_2^*(\eta_{\rm ref})\boldsymbol{V}_3(-\eta)\boldsymbol{V}_3^*(\eta_{\rm ref})\rangle}{\langle \boldsymbol{V}_2(\eta)\boldsymbol{V}_2^*(\eta_{\rm ref})\boldsymbol{V}_3(\eta)\boldsymbol{V}_3^*(\eta_{\rm ref})\rangle} \tag{48}$$

If the longitudinal fluctuations for $\boldsymbol{V}_2$ and $\boldsymbol{V}_3$ are independent of each other, one would expect a factorization relationship $r_{2,3|2,3} \approx r_{2|2} r_{3|3}$.

The other two interesting observables are decorrelation effect of $\boldsymbol{V}_4$ and $\boldsymbol{V}_5$ with their non-linear components:

$$r_{2,2|4}(\eta) = \frac{\langle \boldsymbol{q}_2^2(-\eta)\boldsymbol{q}_4^*(\eta_{\rm ref})\rangle}{\langle \boldsymbol{q}_2^2(\eta)\boldsymbol{q}_4^*(\eta_{\rm ref})\rangle} = \frac{\langle \boldsymbol{V}_2^2(-\eta)\boldsymbol{V}_4^*(\eta_{\rm ref})\rangle}{\langle \boldsymbol{V}_2^2(\eta)\boldsymbol{V}_4^*(\eta_{\rm ref})\rangle} \tag{49}$$

$$r_{2,3|5}(\eta) = \frac{\langle \boldsymbol{q}_2(-\eta)\boldsymbol{q}_3(-\eta)\boldsymbol{q}_5^*(\eta_{\rm ref})\rangle}{\langle \boldsymbol{q}_2(\eta)\boldsymbol{q}_3(\eta)\boldsymbol{q}_5^*(\eta_{\rm ref})\rangle} = \frac{\langle \boldsymbol{V}_2(-\eta)\boldsymbol{V}_3(-\eta)\boldsymbol{V}_5^*(\eta_{\rm ref})\rangle}{\langle \boldsymbol{V}_2(\eta)\boldsymbol{V}_3(\eta)\boldsymbol{V}_5^*(\eta_{\rm ref})\rangle} \tag{50}$$

As discussed in Section 2, higher order flow harmonics contain a linear contribution associated with initial geometry and mode-mixing contributions from lower-order harmonics due to nonlinear hydrodynamic response [16, 17, 49]:

$$\boldsymbol{V}_4 = \boldsymbol{V}_{4\rm L} + \chi_4 \boldsymbol{V}_2^2 \tag{51}$$

$$\boldsymbol{V}_5 = \boldsymbol{V}_{5\rm L} + \chi_5 \boldsymbol{V}_2 \boldsymbol{V}_3 \tag{52}$$

If the linear component of v_4 and v_5 is uncorrelated with lower-order harmonics, i.e. $\langle \boldsymbol{V}_2^2 \boldsymbol{V}_{4\rm L}^*\rangle \sim 0$ and $\langle \boldsymbol{V}_2 \boldsymbol{V}_3 \boldsymbol{V}_{5\rm L}^*\rangle \sim 0$, one expects [47]:

$$r_{2,2|4} \approx r_{2|2;2}\ , \quad r_{2,3|5} \approx r_{2,3|2,3} \tag{53}$$

Furthermore, using Equation (51) the $r_{n|n;1}$ correlators involving $n = 4$ and $n = 5$ can be approximated by:

$$r_{4|4;1}(\eta) \approx \frac{\langle \boldsymbol{V}_{4\rm L}(-\eta)\boldsymbol{V}_{4\rm L}^*(\eta_{\rm ref})\rangle + \chi_4^2 \langle \boldsymbol{V}_2^2(-\eta)\boldsymbol{V}_2^{*2}(\eta_{\rm ref})\rangle}{\langle \boldsymbol{V}_{4\rm L}(\eta)\boldsymbol{V}_{4\rm L}^*(\eta_{\rm ref})\rangle + \chi_4^2 \langle \boldsymbol{V}_2^2(\eta)\boldsymbol{V}_2^{*2}(\eta_{\rm ref})\rangle}\ , \tag{54}$$

$$r_{5|5;1}(\eta) \approx \frac{\langle \boldsymbol{V}_{5\rm L}(-\eta)\boldsymbol{V}_{5\rm L}^*(\eta_{\rm ref})\rangle + \chi_5^2 \langle \boldsymbol{V}_2(-\eta)\boldsymbol{V}_2^*(\eta_{\rm ref})\boldsymbol{V}_3(-\eta)\boldsymbol{V}_3^*(\eta_{\rm ref})\rangle}{\langle \boldsymbol{V}_{5\rm L}(\eta)\boldsymbol{V}_{5\rm L}^*(\eta_{\rm ref})\rangle + \chi_5^2 \langle \boldsymbol{V}_2(\eta)\boldsymbol{V}_2^*(\eta_{\rm ref})\boldsymbol{V}_3(\eta)\boldsymbol{V}_3^*(\eta_{\rm ref})\rangle}\ . \tag{55}$$

Therefore, both the linear and nonlinear components are important for $r_{4|4;1}$ and $r_{5|5;1}$.

4.2 A simple interpretation of the observables

Based on CMS observation that $r_{n|n;1}(\eta)$ decrease almost linearly along η, we propose a simple model, which assumes $\boldsymbol{V}_n$ in each event is a slowly varying function in η near mid-rapidity ($\eta = 0$). Therefore, we perform a perturbative expansion for the flow vector along η near mid-rapidity

$$\boldsymbol{V}_n(\eta) \approx \boldsymbol{V}_n(0)(1 + \alpha_n\eta)e^{i\beta_n\eta} \tag{56}$$

In the equation, $\boldsymbol{V}_n(0)$ is the flow vector at mid-rapidity, the term $(1 + \alpha_n\eta)$ characterizes the linear variation along η direction for flow magnitude, and $e^{i\beta_n\eta}$ represents the rotation (twist) of flow orientation with respect to the flow vector at mid-rapidity. With the above approximation, the flow correlation can be write as

$$\left\langle \boldsymbol{q}_n^k(\eta)\boldsymbol{q}_n^{*k}(\eta_{\rm ref})\right\rangle \approx \left\langle \boldsymbol{q}_n(0)^k \left\langle (1 + k\eta\alpha_n)e^{ik\beta_n\eta}\boldsymbol{q}_n^{*k}(\eta_{\rm ref})\right\rangle\right\rangle \tag{57}$$

Note the linear approximation is only valid for small η, while we still keep $\boldsymbol{q}_n(\eta_{\rm ref})$ as a whole. For the flow vector taken from the reference window at large pseudorapidity, one may not simply take the linear approximation. Instead, we take the following parameterization:

$$\boldsymbol{q}_n^k(0)\boldsymbol{q}_n^{*k}(\eta_{\rm ref}) \equiv X_{n;k}(\eta_{\rm ref}) - iY_{n;k}(\eta_{\rm ref}), \tag{58}$$

Then Equation (57) can be written as

$$\left\langle \boldsymbol{q}_n^k(\eta)\boldsymbol{q}_n^{*k}(\eta_{\rm ref})\right\rangle \approx \langle (1 + k\eta\alpha_n)(X_{n;k} + k\eta\beta_n Y_{n;k})\rangle \approx \langle X_{n;k} + k\eta\alpha_n X_{n;k} + k\eta\beta_n Y_{n;k}\rangle \tag{59}$$

$$= \langle X_{n;k}\rangle \left(1 + k\eta\frac{\langle\alpha_n X_{n;k}\rangle}{\langle X_{n;k}\rangle} + k\eta\frac{\langle\beta_n Y_{n;k}\rangle}{\langle X_{n;k}\rangle}\right) \tag{60}$$

and $r_{n|n;k}$ can be approximated by:

$$r_{n|n;k}(\eta) = 1 - 2kF^{\rm r}_{n;k}\eta,\ \ F^{\rm r}_{n;k} \approx F^{\rm asy}_{n;k} + F^{\rm twi}_{n;k}\ ,\ F^{\rm asy}_{n;k} \equiv \frac{\langle\alpha_n X_{n;k}(\eta_{\rm ref})\rangle}{\langle X_{n;k}(\eta_{\rm ref})\rangle}\ , F^{\rm twi}_{n;k} \equiv \frac{\langle\beta_n Y_{n;k}(\eta_{\rm ref})\rangle}{\langle X_{n;k}(\eta_{\rm ref})\rangle}, \tag{61}$$

If $F^{\mathrm{asy}}_{n;k}$ and $F^{\mathrm{twi}}_{n;k}$ in Equation (61) are also independent of k, i.e.

$$F^{\mathrm{asy}}_{n;k} = F^{\mathrm{asy}}_{n;1} \equiv F^{\mathrm{asy}}_{n}, \quad F^{\mathrm{twi}}_{n;k} = F^{\mathrm{twi}}_{n;1} \equiv F^{\mathrm{twi}}_{n}, \tag{62}$$

then one expects:

$$r_{n|n;k} \approx r^{k}_{n|n;1} \text{ or } r^{k}_{n|n} \tag{63}$$

Deviation from this relation could provide insights on the detailed event-by-event structure in the longitudinal flow fluctuations.

In fact, using the approximation Equation (59) and assuming $\boldsymbol{q}_n(-\eta_{\mathrm{ref}})\boldsymbol{q}^*_n(0) \approx \boldsymbol{q}^*_n(\eta_{\mathrm{ref}})\boldsymbol{q}_n(0)$ we have:

$$\begin{aligned}\langle \boldsymbol{q}_n(-\eta_{\mathrm{ref}})\boldsymbol{q}_n(-\eta)\boldsymbol{q}^*_n(\eta)\boldsymbol{q}^*_n(\eta_{\mathrm{ref}})\rangle &\approx \left\langle \boldsymbol{q}_n(-\eta_{\mathrm{ref}})\boldsymbol{q}^*_n(0)\boldsymbol{q}_n(0)\boldsymbol{q}^*_n(\eta_{\mathrm{ref}})e^{-2i\beta_n\eta}\right\rangle \\ &\approx \left\langle \boldsymbol{q}^2_n(0)\boldsymbol{q}^{2*}_n(\eta_{\mathrm{ref}})e^{-2i\beta_n\eta}\right\rangle = \langle X_{n;2}\rangle\left(1 - 2\eta\frac{\beta_n Y_{n;2}}{\langle X_{n;2}\rangle}\right)\end{aligned} \tag{64}$$

Therefore, the observable R can be approximated as:

$$R_{n|n;2} \approx 1 - 4\eta\frac{\langle \beta_n Y_{n;2}(\eta_{\mathrm{ref}})\rangle}{\langle X_{n;2}(\eta_{\mathrm{ref}})\rangle} \approx 1 - 4F^{\mathrm{twi}}_{n;2}\eta \tag{65}$$

if $R_{n|n;2}$ is parameterized with a linear function similar to Equation (61), then:

$$R_{n|n;2} = 1 - 2F^{\mathrm{R}}_{n}\eta, \quad F^{\mathrm{R}}_{n} \approx 2F^{\mathrm{twi}}_{n;2} \tag{66}$$

The contributions from FB asymmetry and event-plane twist can be estimated from $r_{n|n;2}$ and $R_{n|n;2}$:

$$F^{\mathrm{twi}}_{n;2} = F^{\mathrm{R}}_{n}/2\,, \quad F^{\mathrm{asy}}_{n;2} = F^{\mathrm{r}}_{n;2} - F^{\mathrm{R}}_{n}/2\,, \tag{67}$$

4.3 Datasets

This analysis uses approximately 7 $\mu\mathrm{b}^{-1}$ and 470 $\mu\mathrm{b}^{-1}$ of Pb+Pb data at $\sqrt{s_{\mathrm{NN}}}$ = 2.76 and 5.02 TeV, respectively, recorded by the ATLAS experiment at the LHC. The 2.76 TeV data were collected in 2010, while the 5.02 TeV data were collected in 2015. This trigger system selected 7 $\mu\mathrm{b}^{-1}$ and 22 $\mu\mathrm{b}^{-1}$

of minimum-bias Pb+Pb data at $\sqrt{s_{\mathrm{NN}}}$ = 2.76 TeV and $\sqrt{s_{\mathrm{NN}}}$ = 5.02 TeV, respectively. To increase the number of recorded events from very central Pb+Pb collisions, a dedicated Level-1 trigger was used in 2015 to select events requiring the total transverse energy ($\Sigma_{E_{\mathrm{T}}}$) in the FCal to be more than 4.54 TeV. This ultra-central trigger sampled 470 $\mu\mathrm{b}^{-1}$ of Pb+Pb collisions at 5.02 TeV and was fully efficient for collisions with centrality 0–0.1%. Details about the event and track selection are in Ref. [46].

4.4 Data analysis

The data analysis is divided into two steps: building $\boldsymbol{q}_n^k$ from different subdetectors in an event and constructing different observables with corresponding $\boldsymbol{q}_n^k$. The flow vector from FCal severs as the reference $\boldsymbol{q}_n^k(\eta_{\mathrm{ref}})$, while the ID provide the flow vector as a function of pesudurapidity $\boldsymbol{q}_n^k(\eta)$.

In experiments, the detector performance is not uniform at (η, ϕ) due to various reasons. In this case, supposing we have a isotropic true particle distribution in (η, ϕ), the observed distribution is anistropic due to the detector acceptance effet. This fake anisotropy will bias our flow correlator. The detector acceptant effect also exist for particles with different transverse momentum p_{T}.

In order to remove the detector effects, each track is assigned a weight such that Equation (42) is a weighted average [32]. The weight used for the i^{th}-particle in the ID is defined as:

$$w_i^{\mathrm{ID}}(\eta, \phi, p_{\mathrm{T}}) = d_{\mathrm{ID}}(\eta, \phi)/\epsilon(\eta, p_{\mathrm{T}}) \ , \tag{68}$$

where $\epsilon(\eta, p_{\mathrm{T}})$ is the track efficiency and compensates detector inefficiency in η and p_{T} direction, determined from GEANT simulation and detailed in [46]. The weight factor $d_{\mathrm{ID}}(\eta, \phi)$ corrects for variation of non-uniformity of detector acceptance at ϕ, and is also a function of pesudurapidity η. In practice, we determine $d_{\mathrm{ID}}(\eta, \phi)$ in each given η interval with width equals to 0.1 and use it to all particles detected in the same interval.

For a chosen η interval, the distribution in azimuthal bins, $N(\phi,\eta)$, is built up from reconstructed charged particles summed over all events. The weight factor is then obtained as $d_{\rm ID}(\eta,\phi) \equiv \langle N(\eta)\rangle / N(\phi,\eta)$, where $\langle N(\eta)\rangle$ is the average of $N(\phi,\eta)$. After the "flattening" procedure, the ϕ-dependent non-uniformity from track reconstruction should be removed adequately. This step is very very important for any azimuthal correlation analysis. Similarly, the weight in the FCal for the flow vector from Equation (42) is defined as:

$$w_i^{\rm FCal}(\eta,\phi) = d_{\rm FCal}(\eta,\phi) E_{{\rm T},i} \ , \tag{69}$$

where $E_{{\rm T},i}$ is the transverse energy measured in the i$^{\rm th}$ tower in the FCal covering a small (η,ϕ) region. The azimuthal weight $d_{\rm FCal}(\eta,\phi)$ is calculated in η intervals of 0.1 in a similar way to what is done for the ID. The flow vectors $\boldsymbol{q}_n(\eta)$ and $\boldsymbol{q}_n(\eta_{\rm ref})$ are further corrected by subtracting an event-averaged offset: $\boldsymbol{q}_n - \langle \boldsymbol{q}_n \rangle_{\rm evts}$ [50]. The flow vectors obtained after these reweighting and offset procedures are used in the correlation analysis.

The preprocessed flow vectors are used in the correlation analysis. The correlation quantities used in $r_{n|n;k}$ are calculated as:

$$\left\langle \boldsymbol{q}_n^k(\eta) \boldsymbol{q}_n^{*k}(\eta_{\rm ref}) \right\rangle \equiv \left\langle \boldsymbol{q}_n^k(\eta) \boldsymbol{q}_n^{*k}(\eta_{\rm ref}) \right\rangle_{\rm s} - \left\langle \boldsymbol{q}_n^k(\eta) \boldsymbol{q}_n^{*k}(\eta_{\rm ref}) \right\rangle_{\rm b} \ , \tag{70}$$

where subscripts "s" and "b" represent the correlator constructed from the same event ("signal") and from the mixed-event ("background"), respectively. The mixed-event quantity is constructed by combing $\boldsymbol{q}_n^k(\eta)$ from each event with $\boldsymbol{q}_n^{*k}(\eta_{\rm ref})$ obtained in other events with similar characteritics (centrality, vertex z position etc). Thus the mixed-event quantity contains no signal and should mainly reflect remaining detector effect, which is found to be typically more than two orders of the corresponding signal term.

In general, for the mixed-event quantity, we select q vectors located in the same η range from one event and move to next event for another η range. Depends on how many different η ranges involved in the correlator, we combine the same number of different events to construct the mixed-event quantity. For example, the correlator involving flow vectors in two different

η ranges, e.g. $r_{2,3|5}$, is calculated as:

$$\langle \boldsymbol{q}_2(\eta)\boldsymbol{q}_3(\eta)\boldsymbol{q}_5^*(\eta_{\rm ref})\rangle \equiv \langle \boldsymbol{q}_2(\eta)\boldsymbol{q}_3(\eta)\boldsymbol{q}_5^*(\eta_{\rm ref})\rangle_{\rm s} - \langle \boldsymbol{q}_2(\eta)\boldsymbol{q}_3(\eta)\boldsymbol{q}_5^*(\eta_{\rm ref})\rangle_{\rm b} \ . \quad (71)$$

The product of $\boldsymbol{q}_2(\eta)\boldsymbol{q}_3(\eta)$ is from one event and $\boldsymbol{q}_5^*(\eta_{\rm ref})$ is from a similar event. On the other hand, for correlators involving more than two different η ranges, such as $R_{n|n;2}$, each mixed event is constructed from four different events with similar centrality and $Z_{\rm vtx}$.

Since Pb+Pb is a symmetric collision system, most correlators can be symmetrized. For example, the event averaged quantity holds this condition $\langle \boldsymbol{q}_n^k(-\eta)\boldsymbol{q}_n^{*k}(\eta_{\rm ref})\rangle = \langle \boldsymbol{q}_n^k(\eta)\boldsymbol{q}_n^{*k}(-\eta_{\rm ref})\rangle$. So instead of Equation (46) the actual measured observable is:

$$r_{n|n;k}(\eta) = \frac{\langle \boldsymbol{q}_n^k(-\eta)\boldsymbol{q}_n^{*k}(\eta_{\rm ref}) + \boldsymbol{q}_n^k(\eta)\boldsymbol{q}_n^{*k}(-\eta_{\rm ref})\rangle}{\langle \boldsymbol{q}_n^k(\eta)\boldsymbol{q}_n^{*k}(\eta_{\rm ref}) + \boldsymbol{q}_n^k(-\eta)\boldsymbol{q}_n^{*k}(-\eta_{\rm ref})\rangle} \ . \quad (72)$$

The symmetrization procedure also allows further cancellation of possible differences between η and $-\eta$ in the tracking efficiency or detector acceptance. Similarly, we have

$$r_{2,2|4}(\eta) = \frac{\langle \boldsymbol{q}_2^2(-\eta)\boldsymbol{q}_4^*(\eta_{\rm ref})\rangle + \langle \boldsymbol{q}_2^2(\eta_{\rm ref})\boldsymbol{q}_4^*(-\eta)\rangle}{\langle \boldsymbol{q}_2^2(\eta)\boldsymbol{q}_4^*(\eta_{\rm ref})\rangle + \langle \boldsymbol{q}_2^2(\eta_{\rm ref})\boldsymbol{q}_4^*(\eta)\rangle} \quad (73)$$

$$r_{2,3|5}(\eta) = \frac{\langle \boldsymbol{q}_2(-\eta)\boldsymbol{q}_3(-\eta)\boldsymbol{q}_5^*(\eta_{\rm ref})\rangle + \langle \boldsymbol{q}_2(\eta_{\rm ref})\boldsymbol{q}_3(\eta_{\rm ref})\boldsymbol{q}_5^*(-\eta)\rangle}{\langle \boldsymbol{q}_2(\eta)\boldsymbol{q}_3(\eta)\boldsymbol{q}_5^*(\eta_{\rm ref})\rangle + \langle \boldsymbol{q}_2(\eta_{\rm ref})\boldsymbol{q}_3(\eta_{\rm ref})\boldsymbol{q}_5^*(\eta)\rangle} \quad (74)$$

The last thing to mention is related to the the algorithm implemented in data analysis. For example, in the $\langle \boldsymbol{q}_n^k(-\eta)\boldsymbol{q}_n^{*k}(\eta_{\rm ref})\rangle$ correlator, when $k = 2$ case, we need to calculate squared $\boldsymbol{q}_n$:

$$\boldsymbol{q}_n^2 = \frac{\sum_{i=1}^{N}\sum_{j=1}^{N} w_i w_j e^{in(\phi_i+\phi_j)}}{\sum_{i=1}^{M}\sum_{j=1}^{M} w_i w_j} \quad (75)$$

in this way $\boldsymbol{q}_n^2$ contains duplicated particle with the same index $i = j$, which is a $\boldsymbol{q}_{2n}$ contribution. The duplication of same indexed particles introduce mixture of harmonics of other orders. These particle multiples need to be removed. In this analysis, for the correlator which use more than one q-vector

term in correlator	with correction
$\boldsymbol{q}_n^2$	$(\boldsymbol{q}_n^2 - \omega_1 \boldsymbol{q}_{2n})/(1-\omega_1)$
$\boldsymbol{q}_n^3$	$(\boldsymbol{q}_n^3 - 3\omega_1 \boldsymbol{q}_{2n}\boldsymbol{q}_n + 2\omega_2 \boldsymbol{q}_{3n})/(1-3\omega_1+2\omega_2)$
$\boldsymbol{q}_2\boldsymbol{q}_3$	$(\boldsymbol{q}_2\boldsymbol{q}_3 - \omega_1 \boldsymbol{q}_5)/(1-\omega_1)$

Table 1: The correction to remove duplicated particle multiple. Here $\omega_k = \frac{\sum_i w_i^{k+1}}{(\sum_i w_i)^{k+1}}$ and $\boldsymbol{q}_{kn} = \frac{\sum_i w_i^k e^{in\phi_i}}{\sum_i w_i^k}$ and w_i is the particle weight and ϕ_i is the azimuthal angle of particle.

from the same η region or k times of the same $\boldsymbol{q}_n$, we remove the contained duplicated terms. The actually correlator are calculated in Table 1. Note we can only do this correction for $\boldsymbol{q}_n(\eta)$ calculated using tracks in Inner Detector and couldn't do that for flow vector $\boldsymbol{q}_n(\eta_{\rm ref})$ calculated using towers of FCal. But the duplicated term contribution should be small in FCal, since its contribution is inverse to multiplicity, $1/M$. On the other hand, this duplicated term from FCal is equal in numerator and denominator so it should largely cancel out in the ratio.

As a summary, Table 2 gives a list of the set of correlators measured in this analysis. The results are calculated in intervals of centrality and presented as a function of η for the range $|\eta| < 2.4$. The main results are obtained using 5.02 TeV Pb+Pb data. The 2010 2.76 TeV Pb+Pb data are statistically limited, and are used only to obtain $r_{n|n;1}$ and $R_{n|n;2}$ to study the dependence on collision energy.

Figure 31 and Figure 32 show the sensitivity of $r_{2|2;1}$ and $r_{3|3;1}$, respectively, to the choice of the range of $\eta_{\rm ref}$. A smaller $\eta_{\rm ref}$ value implies a smaller pseudorapidity gap between η and $\eta_{\rm ref}$. The values of $r_{n|n;1}$ generally decrease with decreasing $\eta_{\rm ref}$, possibly reflecting the contributions from the dijet correlations. However, such contributions should be reduced in the most central collisions due to large charged-particle multiplicity and jet-quenching effects. Therefore, the decrease of $r_{n|n;1}$ in the most central collisions may also reflect the $\eta_{\rm ref}$ dependence of $F^{\rm r}_{n;1}$. In this analysis, the reference flow vector is cal-

Table 2: The list of observables measured in flow decorrelation analysis.

Observables	Pb+Pb datasets
$r_{n\|n;k}$ for n = 2,3,4 and k = 1	2.76 and 5.02 TeV
$R_{n\|n;2}$ for n = 2,3	2.76 and 5.02 TeV
$r_{n\|n;k}$ for n = 5 and k = 1	5.02 TeV
$r_{n\|n;k}$ for n = 2,3 and k = 2,3	5.02 TeV
$R_{n\|n;2}$ for n = 4	5.02 TeV
$r_{2,2\|4}$, $r_{2,3\|5}$, $r_{2,3\|2,3}$	5.02 TeV

culated from $4.0 < \eta_{\rm ref} < 4.9$, which reduces the effect of dijets and provides good statistical precision. For this choice of $\eta_{\rm ref}$ range, $r_{2|2;1}$ and $r_{3|3;1}$ show a linear decrease as a function of η in most centrality intervals, indicating a significant breakdown of factorization. A similar comparison for $r_{4|4;1}$ can be found in the Ref. [46].

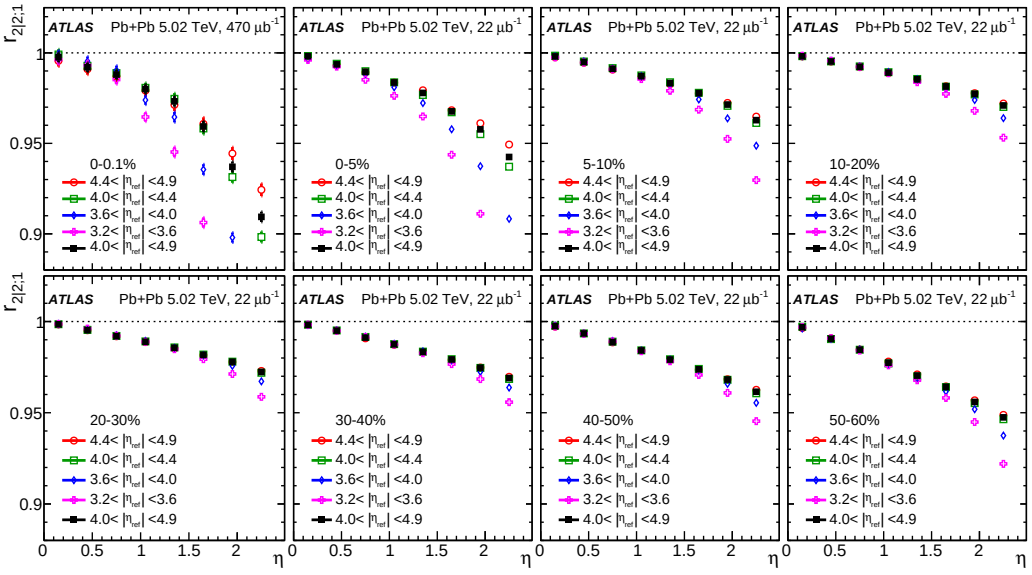

Figure 31: The $r_{2|2;1}(\eta)$ measured for several $\eta_{\rm ref}$ ranges. Each panel shows the results for one centrality range. The error bars are statistical only.

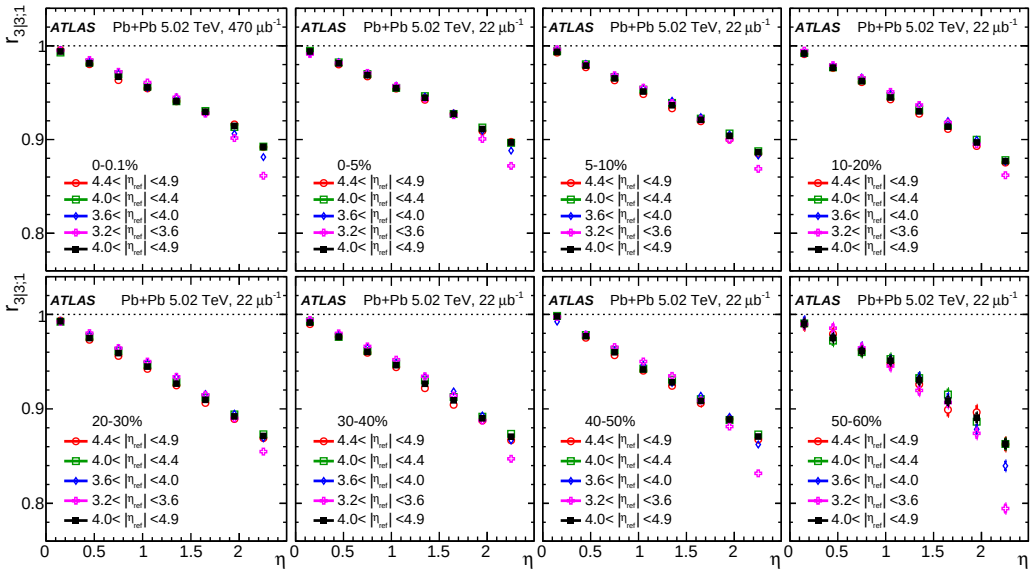

Figure 32: The $r_{3|3;1}(\eta)$ measured for several η_{ref} ranges. Each panel shows the results for one centrality range. The error bars are statistical only.

Figure 33 and Figure 34 show $r_{2|2;1}$ and $r_{3|3;1}$ calculated for several p_{T} ranges of the charged particles in the ID. A similar comparison for $r_{4|4;1}$ can be found in the Ref. [46]. If the longitudinal-flow asymmetry and twist reflect global properties of the event, the values of $r_{n|n;1}$ should not depend strongly on p_{T}. Indeed no dependence is observed, except for $r_{2|2;1}$ in the most central collisions and very peripheral collisions. The behavior in central collisions may be related to the factorization breaking of the v_2 as a function of p_{T} and η [45]. The behavior in peripheral collisions is presumably due to increasing relative contributions from jets and dijets at higher p_{T} and for peripheral collisions. Based on this, the measurements are performed using charged particles with $0.5 < p_{\mathrm{T}} < 3$ GeV.

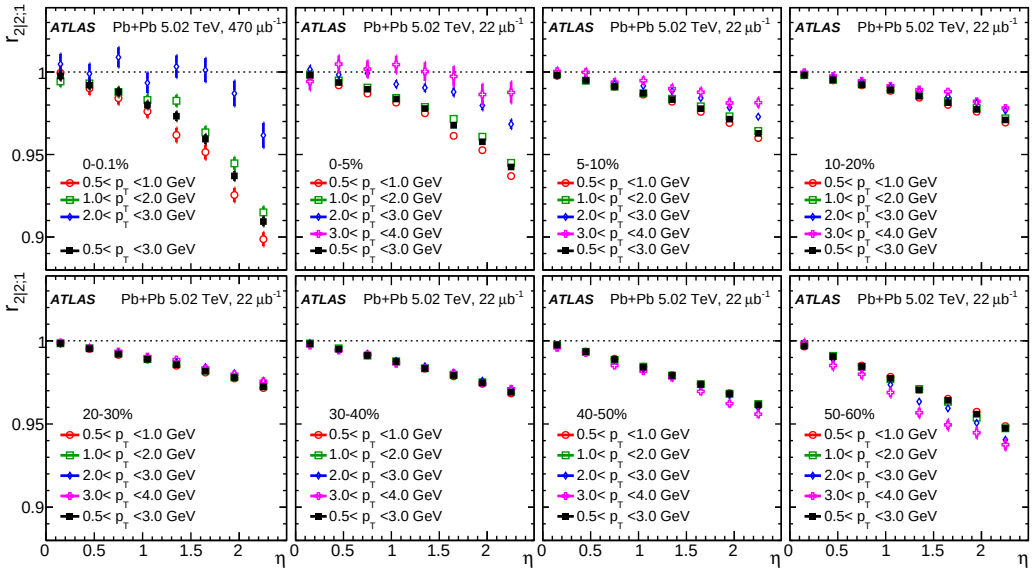

Figure 33: The $r_{2|2;1}(\eta)$ measured in several p_{T} ranges. Each panel shows the results for one centrality range. The error bars are statistical only.

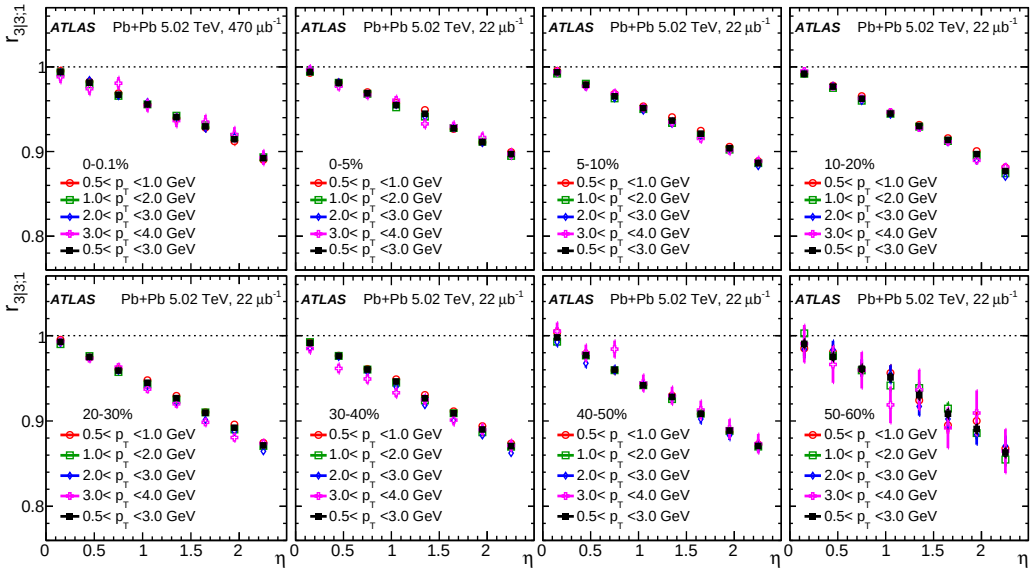

Figure 34: The $r_{3|3;1}(\eta)$ measured in several p_{T} ranges. Each panel shows the results for one centrality range. The error bars are statistical only.

4.5 Systematic uncertainties

In this analysis, all the observables are found to follow approximately linear decrease with η, i.e. $D(\eta) \approx 1 - c\eta$ for a given observable $D(\eta)$ where c is a constant. The systematic uncertainty is therefore presented as the relative uncertainty to $1 - D(\eta)$ at $\eta = 1.2$. There are several sources contributing to the systematic uncertainty:

- The effect of detector azimuthal non-uniformity
- The systematic uncertainty associated with the track quality
- the p_{T} -dependent uncertainty in the track reconstruction efficiency $\epsilon(\eta, p_{\mathrm{T}})$

Details about the systematic is summarized in Ref [46], and the values are listed in Tables 3–5.

Table 3: Systematic uncertainties in percent for $1 - r_{2|2;k}$ and $1 - r_{3|3;k}$ at $\eta = 1.2$ in selected centrality intervals.

	$1-r_{2\|2;1}$			$1-r_{2\|2;2}$			$1-r_{2\|2;3}$		
	0–5%	20–30%	40–50%	0–5%	20–30%	40–50%	0–5%	20–30%	40–50%
Event mixing[%]	0.8	0.2	0.3	2.2	0.4	0.6	6.0	0.6	2.1
Track selections[%]	0.4	0.3	0.2	1.5	0.4	0.9	9.4	1.0	2.4
Reco. efficiency[%]	0.3	0.1	0.1	0.4	0.1	0.1	0.9	0.1	0.1
Total[%]	1.0	0.4	0.4	2.7	0.6	1.1	12	1.2	3.2
	$1-r_{3\|3;1}$			$1-r_{3\|3;2}$			$1-r_{3\|3;3}$		
	0–5%	20–30%	40–50%	0–5%	20–30%	40–50%	0–5%	20–30%	
Event mixing[%]	0.6	0.4	0.9	2.2	1.2	7.9	7.0	9.5	
Track selections[%]	0.6	0.2	0.6	2.5	0.7	4.4	12	10	
Reco. efficiency[%]	0.1	0.1	0.1	0.4	0.2	0.9	1.1	1.5	
Total[%]	0.9	0.5	1.1	3.4	1.5	9.1	14	14	

Table 4: Systematic uncertainties in percent for $1 - R_{2|2;2}$, $1 - R_{3|3;2}$, $1 - r_{4|4;1}$ and $1 - r_{5|5;1}$ at $\eta = 1.2$ in selected centrality intervals.

	$1-R_{2\|2;2}$			$1-R_{3\|3;2}$		
	0–5%	20–30%	40–50%	0–5%	20–30%	40–50%
Event mixing [%]	6.1	1.5	1.5	4.6	2.9	14
Track selections [%]	3.5	0.4	0.7	2.0	3.2	13
Reco. efficiency[%]	0.2	0.1	0.1	0.1	0.2	0.5
Total [%]	7.1	1.6	1.7	5.1	4.4	20
	$1-r_{4\|4;1}$			$1-r_{5\|5;1}$		
	0–5%	20–30%	40–50%	0–5%	20–30%	40–50%
Event mixing [%]	1.8	1.5	2.7	13	5.1	9.8
Track selections [%]	1.5	1.1	2.0	6.3	3.6	4.6
Reco. efficiency[%]	0.3	0.3	0.6	2.2	1.6	1.3
Total [%]	2.4	1.9	3.5	15	6.5	11

	$1-r_{2,3\|2,3}$			$1-r_{2,2\|4}$			$1-r_{2,3\|5}$		
	0–5%	20–30%	40–50%	0–5%	20–30%	40–50%	0–5%	20–30%	40–50%
Event mixing [%]	4.1	1.7	3.2	16	1.5	2.4	15	3.4	7.8
Track selections [%]	1.4	0.5	2.0	12	1.6	1.5	14	2.0	7.4
Reco. efficiency[%]	0.1	0.0	0.1	1.6	0.1	0.1	1.2	0.1	0.5
Total [%]	4.4	1.8	3.8	21	2.2	2.9	21	4.0	11

Table 5: Systematic uncertainties in percent for $1 - r_{2,3|2,3}$, $1 - r_{2,2|4}$ and $1 - r_{2,3|5}$ at $\eta = 1.2$ in selected centrality intervals.

4.6 Results

4.6.1 $r_{n|n;1}$

Figures 35 to 37 shows the longitudinal decorrelation of flow vector $r_{n|n;k}(\eta)$ for different orders($n = 2, 3, 4$) and $k = 1$, for different centrality bins in Pb+Pb collisions with two different collision energies. For simplicity only the first moment $k = 1$ results are shown in these figures. For $k > 1$ cases and comparison between different k will be discussed in next subsection. The

three figures are results for elliptic flow(n = 2) , triangular flow(n = 3) and quadrangle flow(n = 4) respectively. In each figure, from top left to bottom right , $r_{n|n;1}(\eta)$ is presented in different centrality classes from central 0% to peripheral 60%. In each panel, there are two curves representing the same observable measured at two different collision energy 2.76TeV and 5.02TeV as comparison.

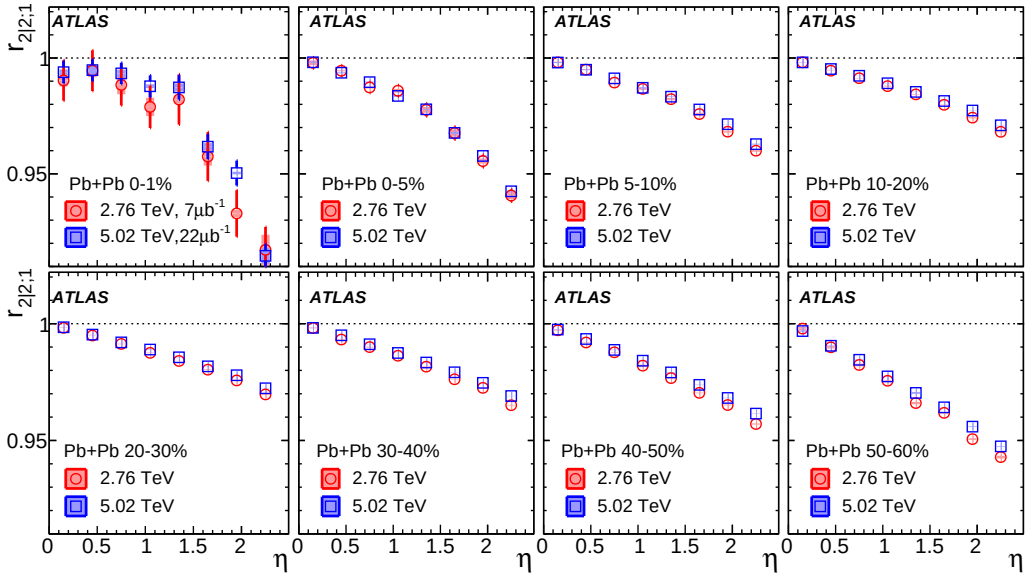

Figure 35: The $r_{2|2;1}(\eta)$ compared between the two collision energies. Each panel shows results from one centrality interval. The error bars and shaded boxes are statistical and systematic uncertainties, respectively.

From Figures 35 to 37, a almost linear decrease as a function of η is observed for the decorrelation of flow vector $\boldsymbol{V}_2$, $\boldsymbol{V}_3$ and $\boldsymbol{V}_4$, except in the most central collisions of $\boldsymbol{V}_2$. These slope of decreasing trend reflects the strength of decorrelation. The elliptic flow decorrelaiton shows a non-monotonic centrality dependence (it is weakest around the 20–30% centrality range, and is more pronounced in both more central and more peripheral collisions). Such non-monotonic centrality dependence is associated with the average elliptic

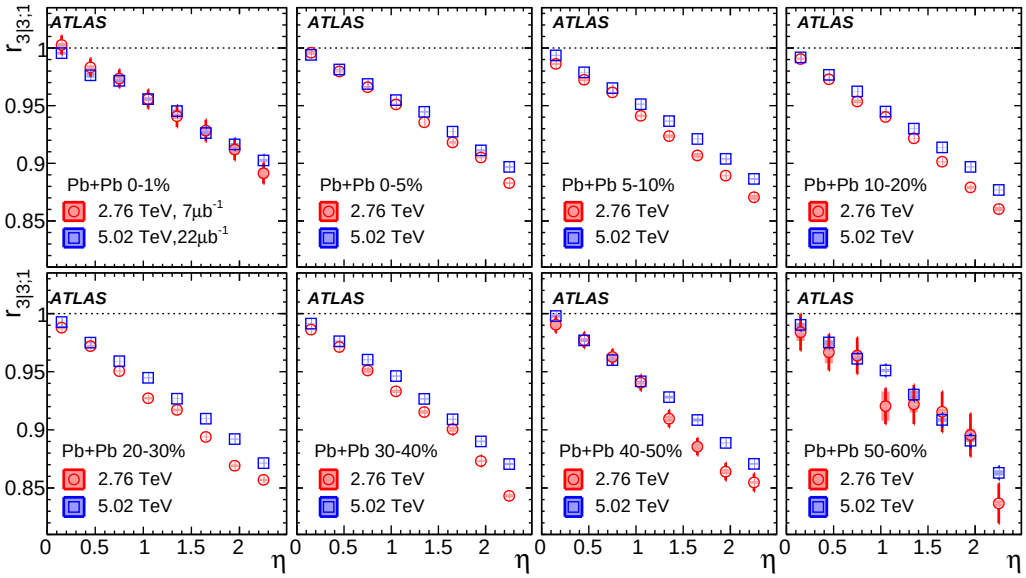

Figure 36: Similar plot to Figure 35 but for $r_{3|3;1}(\eta)$.

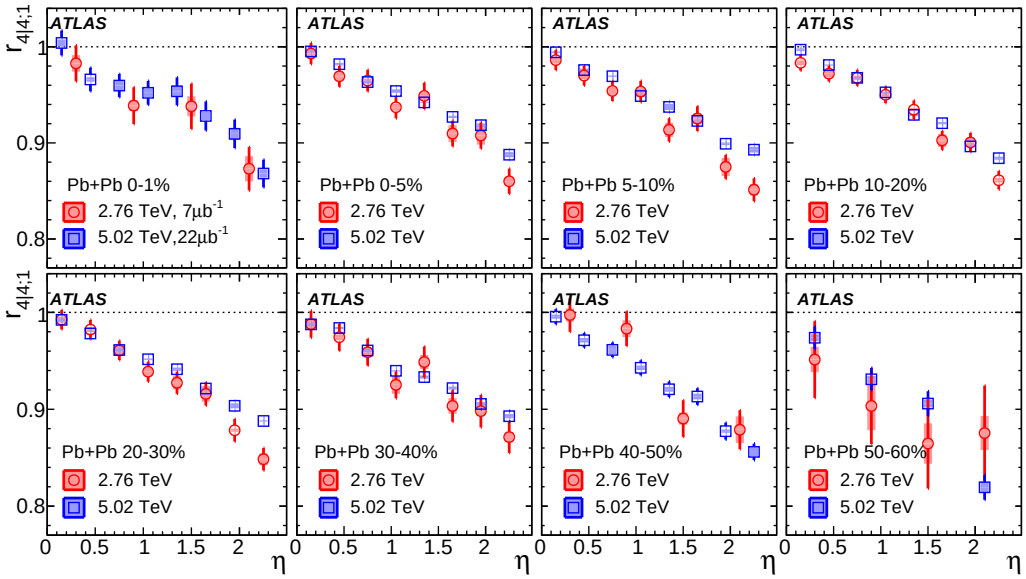

Figure 37: Similar plot to Figure 35 but for $r_{4|4;1}(\eta)$.

shape of initial conditions created by non-central overlapping collision region [51], which drives the development of elliptic flow in mid-central collisions,

whereas the fluctuation becomes more important in central collisions and peripheral collisions. For triangular and quadrangle flow, the rate of the decrease is approximately independent of centrality. This could be due to the fact that both of them are driven by fluctuations. The difference of flow origin between v_2 and v_3, v_4 may be one reason that the observed decorrelation is stronger for $n > 2$.

Note, in $0-1\%$ centrality the rate of v_2 decrease is weaker than v_3, v_4 and the decreasing trend is more like a qubic function $1 - a\eta - b\eta^3$. The original motivation is that the initial conditions in $0-1\%$ centrality or less is predominantly generated by fluctuations such that magnitudes of first several ϵ_n are comparable and the hydrodynamic response is expected to be linear $v_n \propto \epsilon_n$ for all harmonics. However v_2 is observed to differ from original expectation not only in its amplitude compared with other harmonics, but also in the shape of $v_2(p_{\mathrm{T}})$. Further more the event plane angle Φ_2 at same η is found to be different among different p_{T}, while for other harmonics the event plane angles are similar among different p_{T}. The peculiarity of elliptic flow in most central collisions is still in under exploration in theory.

As for the collision energy dependence of flow decorrelation, From Figures 35 to 37 shows all three harmonics have a little stronger decorrelation at lower energy 2.76TeV, which is expected as the collision system becomes less boost-invariant at lower collision energy and it is also observed in a recent study using AMPT initial condition [52].

The decreasing trend of $r_{n|n;1}$ for n = 2–4 in Figures 35 to 37 indicates significant breakdown of the factorization of two-particle flow harmonics into those between different η ranges. However, the size of breakdown depends on the harmonic order n, collision centrality, and collision energy.

4.6.2 $R_{n|n;2}$

Figures 38 and 39 show $R_{2|2;2}$ and $R_{3|3;2}$ in several centrality intervals. Firstly, we see both observables decrease linearly with η in all centrality intervals. Secondly, the decreasing rates is faster at lower collision energy. Since $R_{2|2;2} \neq$

1 is mostly caused by the event-plane twist [47], so the energy dependence study indicates stronger event-plane decorrelation effect at lower energy.

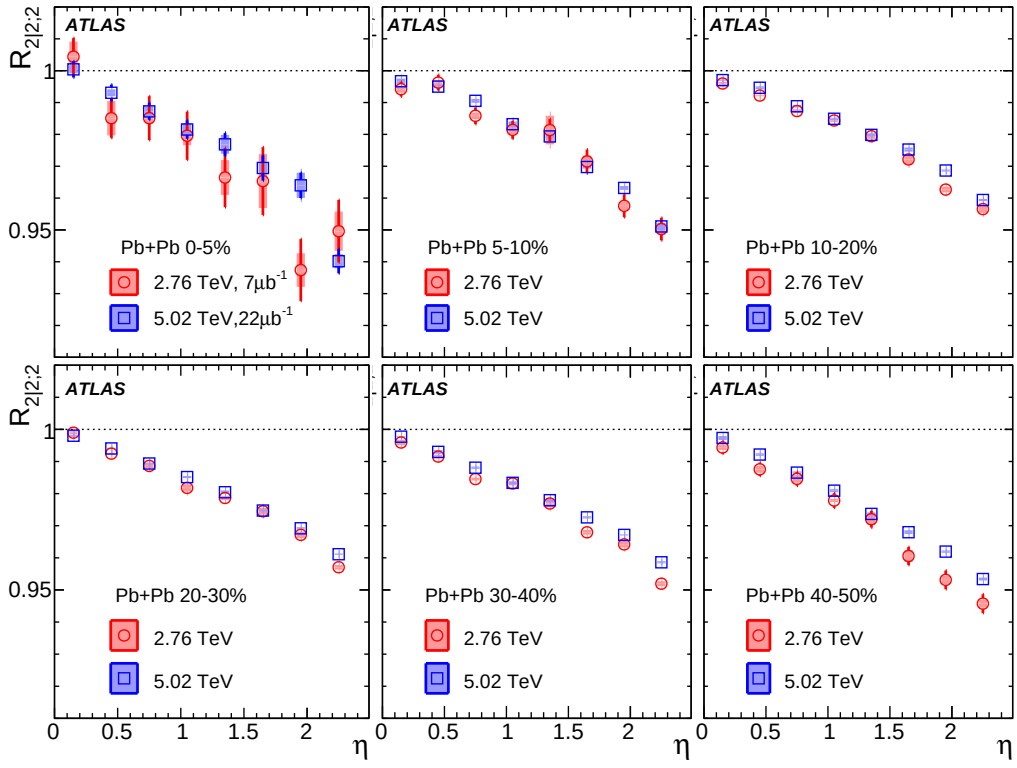

Figure 38: The $R_{2|2;2}(\eta)$ compared between the two collision energies. Each panel shows results from one centrality interval. The error bars and shaded boxes are statistical and systematic uncertainties, respectively.

As stated before, the measured decreasing trend can be described by linear functions quite well

$$r_{n|n;k} = 1 - 2F^{\mathrm{r}}_{n;k}\,\eta\,, \quad R_{n|n;2} = 1 - 2F^{\mathrm{R}}_{n;2}\,\eta \tag{76}$$

here, the slope parameters are obtained with as linear-regression coefficients, which is the same with least squares fitting.

$$F^{\mathrm{r}}_{n;k} = \frac{\sum_i (1 - r_{n|n;k}(\eta_i))\eta_i}{2\sum_i \eta_i^2}\,, \quad F^{\mathrm{R}}_{n;2} = \frac{\sum_i (1 - R_{n|n;2}(\eta_i))\eta_i}{2\sum_i \eta_i^2}\,, \tag{77}$$

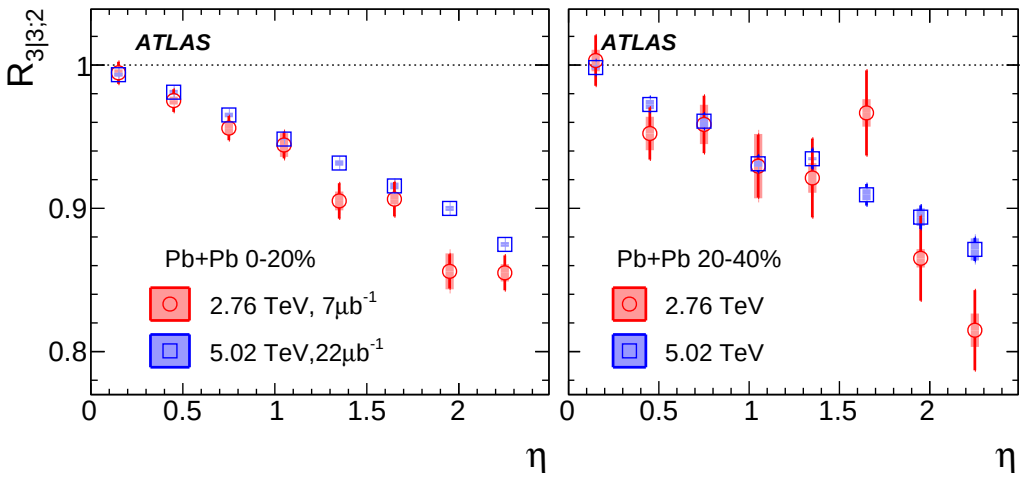

Figure 39: Similar plot with Figure 38 but for $R_{3|3;2}(\eta)$.

This slope reflects the the average η-weighted deviation of $r_{n|n;1}(\eta)$ and $R_{n|n;2}(\eta)$ from unity, where the average runs over all data points. Characterizing decorrelation effect using slope provides more clear information than using the decorrelation function.

Figure 40 and Figure 41 shows $F^{\rm r}_{n;1}$ and $F^{\rm R}_{n;2}$ as a function of centrality (in terms of $N_{\rm part}$) respectively. As one seen the $F^{\rm r}_{n;1}$ and $F^{\rm R}_{n;2}$ has centrality dependence for some harmonic order. How the F parameter change from one energy to another is studied in relative value, via the ratio of $F^{\rm r}_{2;1}$ values and of $F^{\rm R}_{2;2}$ values at the two energies.

The values of $F^{\rm r}_{n;1}$ and $F^{\rm R}_{n;2}$ are larger with decreasing $\sqrt{s_{\rm NN}}$, as the rapidity profile of the initial state is more compressed due to smaller beam rapidity $y_{\rm beam}$ at lower $\sqrt{s_{\rm NN}}$. This energy dependence has been predicted for $F^{\rm r}_{n;1}$ in hydrodynamic model calculations [53], and it is quantified in Figure 42 via the ratio of $F^{\rm r}_{2;1}$ values and of $F^{\rm R}_{2;2}$ values at the two energies. The weighted averages of the ratios calculated in the range $30 < N_{\rm part} < 400$ are given in Table 6. Compared to $\sqrt{s_{\rm NN}}$ = 5.02 TeV, the values of $F^{\rm r}_{2;1}$ and $F^{\rm R}_{2;2}$ at $\sqrt{s_{\rm NN}}$ = 2.76 TeV are about 10% higher, and the values of $F^{\rm r}_{3;1}$ and $F^{\rm r}_{4;1}$ are about 16% higher.

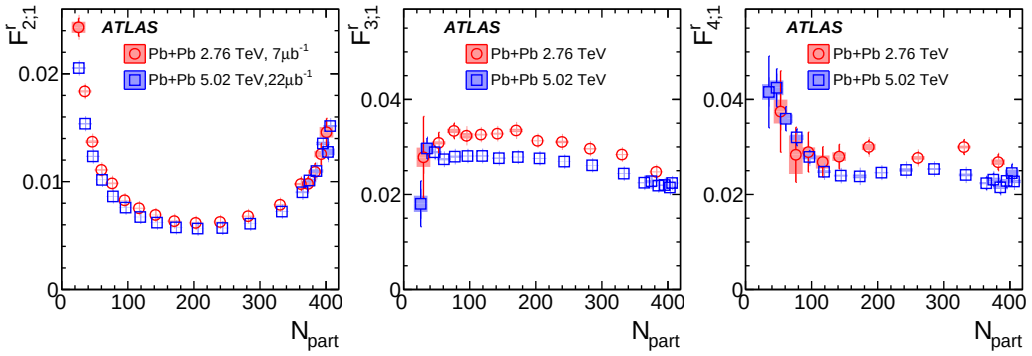

Figure 40: Centrality dependence of $F^{\mathrm{r}}_{2;1}$ (left panel), $F^{\mathrm{r}}_{3;1}$ (middle panel) and $F^{\mathrm{r}}_{4;1}$ (right panel) for Pb+Pb at 2.76 TeV (circles) and 5.02 TeV (squares). The error bars and shaded boxes are statistical and systematic uncertainties, respectively. The widths of the centrality intervals are not fixed but are optimized to reduce the uncertainty.

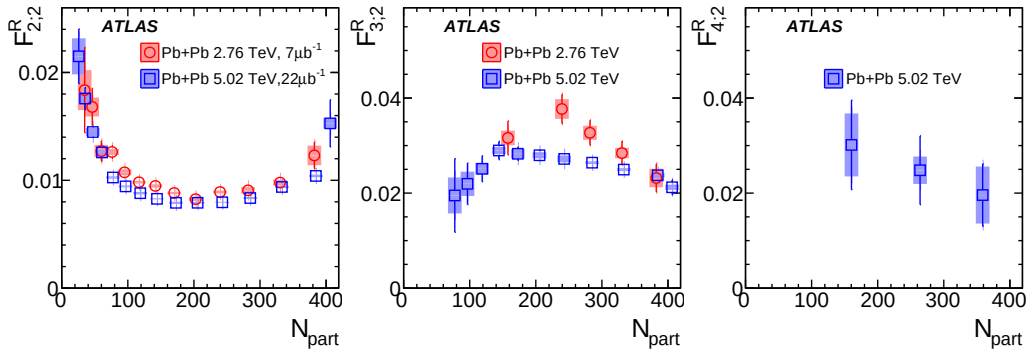

Figure 41: Centrality dependence of $F^{\mathrm{R}}_{2;2}$ (left panel), $F^{\mathrm{R}}_{3;2}$ (middle panel) and $F^{\mathrm{R}}_{4;2}$ (right panel) for Pb+Pb at 2.76 TeV (circles) and 5.02 TeV (squares). The error bars and shaded boxes are statistical and systematic uncertainties, respectively. The widths of the centrality intervals are not fixed but are optimized to reduce the uncertainty.

Another thing is that at different energy, the collision system has different longitudinal length y_{beam}, so maybe the entire change of slope parameter

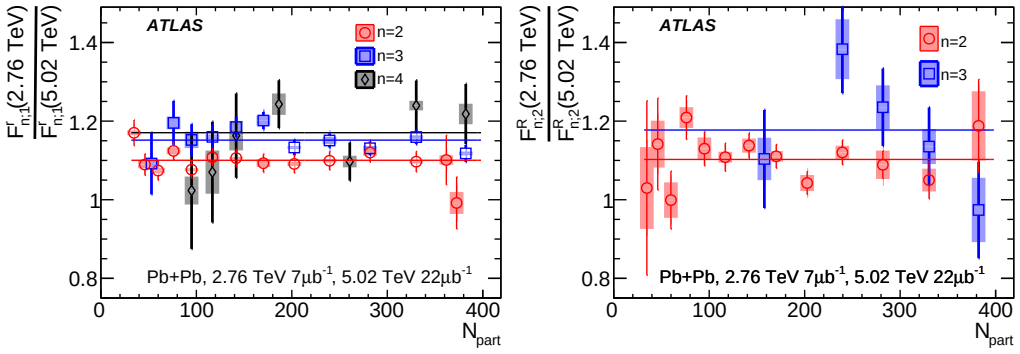

Figure 42: Centrality dependence of ratio of $F^{\mathrm{r}}_{n;1}$ values (left panel) and $F^{\mathrm{R}}_{n;2}$ values (right panel) at 2.76 TeV and 5.02 TeV. The lines indicate the average values in the range $30 < N_{\mathrm{part}} < 400$, with the results and fit uncertainties given by Table 6. The error bars and shaded boxes are statistical and systematic uncertainties, respectively.

with $\sqrt{s_{\mathrm{NN}}}$ can be explained by this. So we should study the decorrelaiton function as a function of scaled pseudorapidity η/y_{beam}. In this case, the slope parameter should be multiplied by the beam rapidity, i.e. $\hat{F}^{\mathrm{r}}_{n;1} \equiv F^{\mathrm{r}}_{n;1} y_{\mathrm{beam}}$ and $\hat{F}^{\mathrm{R}}_{n;2} \equiv F^{\mathrm{R}}_{n;2} y_{\mathrm{beam}}$.

Figure 43 shows the ratio of $\hat{F}^{\mathrm{r}}_{2;1}$ values and of $\hat{F}^{\mathrm{R}}_{2;2}$ values at the two energies. The beam rapidity is $y_{\mathrm{beam}} = 7.92$ and 8.52 for $\sqrt{s_{\mathrm{NN}}} = 2.76$ and 5.02 TeV, which can lead to %7.5 reduction of the ratio. And the final result shows $\hat{F}^{\mathrm{r}}_{2;1}$ and $\hat{F}^{\mathrm{R}}_{2;2}$ at $\sqrt{s_{\mathrm{NN}}} = 2.76$ TeV are about 3% higher, and the values of $\hat{F}^{\mathrm{r}}_{3;1}$ and $\hat{F}^{\mathrm{r}}_{4;1}$ are about 8% higher

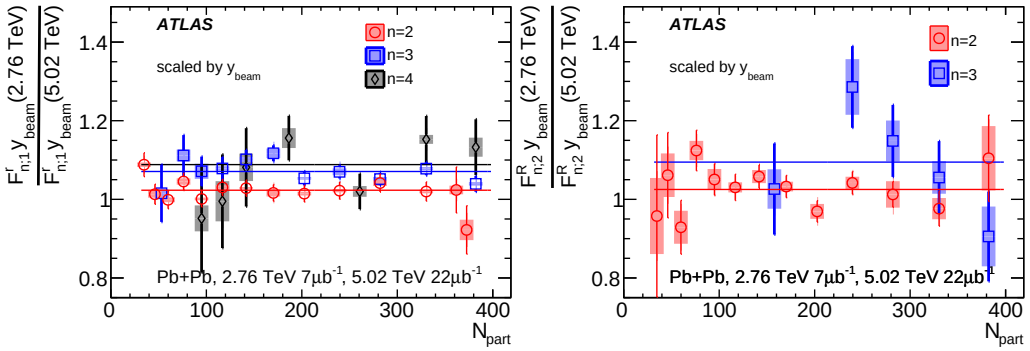

Figure 43: Centrality dependence of ratio of $\hat{F}^{\mathrm{r}}_{n;1} \equiv F^{\mathrm{r}}_{n;1} y_{\mathrm{beam}}$ values (left panel) and $\hat{F}^{\mathrm{R}}_{n;2} \equiv F^{\mathrm{R}}_{n;2} y_{\mathrm{beam}}$ values (right panel) at 2.76 TeV and 5.02 TeV. The lines indicate the average values in the range $30 < N_{\mathrm{part}} < 400$, with the results and fit uncertainties given by Table 6. The error bars and shaded boxes are statistical and systematic uncertainties, respectively.

Table 6: Results of the fits to the ratio of $F^{\mathrm{r}}_{n;1}$, $F^{\mathrm{R}}_{n;2}$, $\hat{F}^{\mathrm{r}}_{n;1} \equiv F^{\mathrm{r}}_{n;1} y_{\mathrm{beam}}$ and $\hat{F}^{\mathrm{R}}_{n;2} \equiv F^{\mathrm{R}}_{n;2} y_{\mathrm{beam}}$ values at the two energies in the range $30 < N_{\mathrm{part}} < 400$ shown in Figures 42 and 43. The uncertainties include both statistical and systematic uncertainties.

	$n = 2$	$n = 3$	$n = 4$
$F^{\mathrm{r}}_{n;1}(2.76\ \mathrm{TeV})/F^{\mathrm{r}}_{n;1}(5.02\ \mathrm{TeV})$	1.100 ± 0.010	1.152 ± 0.011	1.17 ± 0.036
$F^{\mathrm{R}}_{n;2}(2.76\ \mathrm{TeV})/F^{\mathrm{R}}_{n;2}(5.02\ \mathrm{TeV})$	1.103 ± 0.026	1.18 ± 0.08	–
$\hat{F}^{\mathrm{r}}_{n;1}(2.76\ \mathrm{TeV})/\hat{F}^{\mathrm{r}}_{n;1}(5.02\ \mathrm{TeV})$	1.023 ± 0.009	1.071 ± 0.010	1.088 ± 0.033
$\hat{F}^{\mathrm{R}}_{n;2}(2.76\ \mathrm{TeV})/\hat{F}^{\mathrm{R}}_{n;2}(5.02\ \mathrm{TeV})$	1.025 ± 0.024	1.10 ± 0.07	–

4.6.3 $r_{n|n;k}$ $(k > 1)$

$r_{2|2;k}$ can be extended to higher order of k, which carry more information about the probability distribution of EbyE flow fluctuations in η. Under assumptions in Ref. [47], it is shown that a scaling relationship $F_{n;k}/k = F_{n;1}$ holds as given by Equation (63).

Figure 44 compares the results for second-order harmonic flow v_2 at 5.02 TeV, where $r_{2|2;k}$ for k = 1–3 with $r^k_{2|2;1}$ for k = 2–3 are plotted together for comparison. In the most central collisions (0–5% centrality), where v_2 is driven by the initial-state fluctuations, $r_{2|2;k} = r^k_{2|2;1}$ almost holds. In other centrality intervals, where the average geometry contribution for v_2 is more important, we see $r_{2|2;k} < r^k_{2|2;1}$.

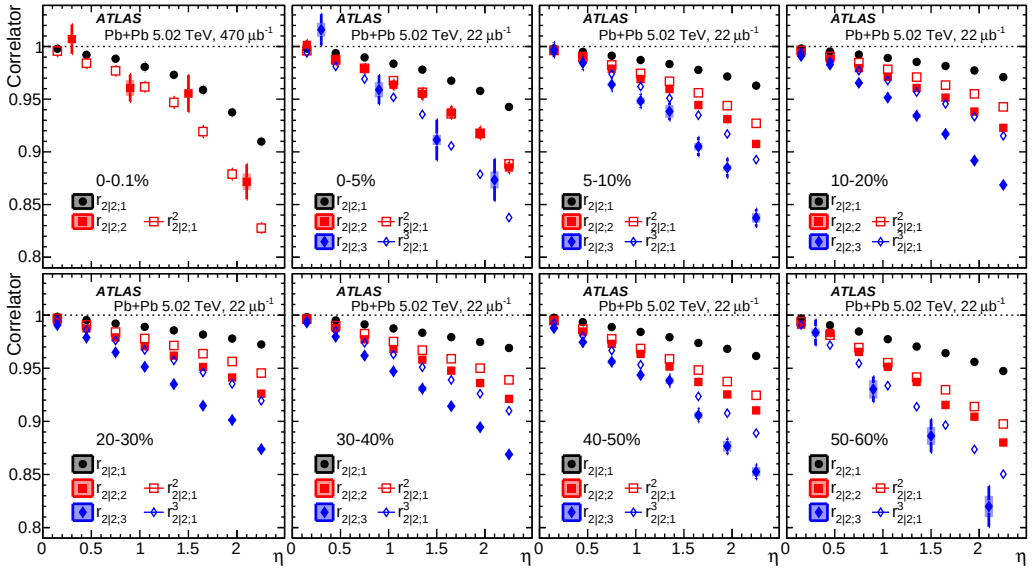

Figure 44: The $r_{2|2;k}$ for k = 1–3 compared with $r^k_{2|2;1}$ for k = 2–3 in various centrality intervals for Pb+Pb collisions at 5.02 TeV. The error bars and shaded boxes are statistical and systematic uncertainties, respectively. The data points for k = 2 or 3 in some centrality intervals are rebinned to reduce the uncertainty.

Figure 45 shows the result for third-order harmonic flow v_3, which is driven by initial-state fluctuations in all centrality intervals. The data indicates $r_{3|3;k} = r^k_{3|3;1}$ holds approximately.

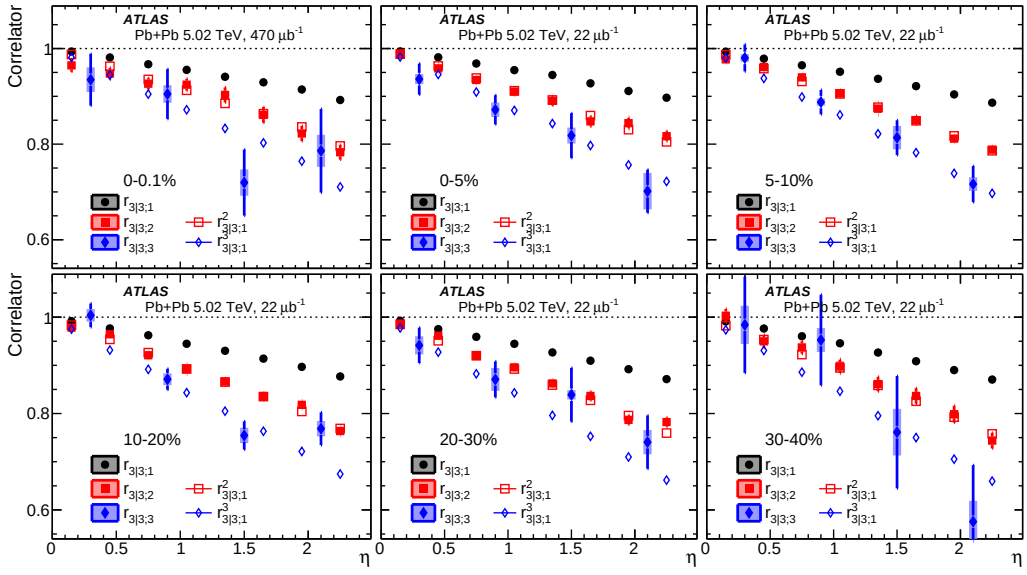

Figure 45: The $r_{3|3;k}$ for k = 1–3 compared with $r^k_{3|3;1}$ for k = 2–3 in various centrality intervals for Pb+Pb collisions at 5.02 TeV. The error bars and shaded boxes are statistical and systematic uncertainties, respectively. The data points for k = 2 or 3 in some centrality intervals are rebinned to reduce the uncertainty.

In this analysis, the difference between $r_{n|n;k}$ and $r^k_{n|n;1}$ is quantified using the slopes ($F^{\mathrm{r}}_{n;k}$) of $r_{n|n;k}$ are calculated via Equation (76) and Equation (77).Then, the scaled slopes $F^{\mathrm{r}}_{n;k}/k$ are compared with each other as a function of centrality in Figure 46.

For elliptic flow v_2, the data shows a clearing hierarchy $F^{\mathrm{r}}_{2;3}/3 > F^{\mathrm{r}}_{2;2}/2 > F^{\mathrm{r}}_{2;1}$. However in the most central and most peripheral collisions, the scaling relationship $F^{\mathrm{r}}_{n;k}/k = F^{\mathrm{r}}_{n;1}$ holds approximately. On the other hand, For triangular flow v_3, the data shows a slightly opposite trend , $F^{\mathrm{r}}_{3;3}/3 \lesssim F^{\mathrm{r}}_{3;2}/2 \lesssim F^{\mathrm{r}}_{3;1}$

in mid-central collisions ($150 < N_{\rm part} < 350$).

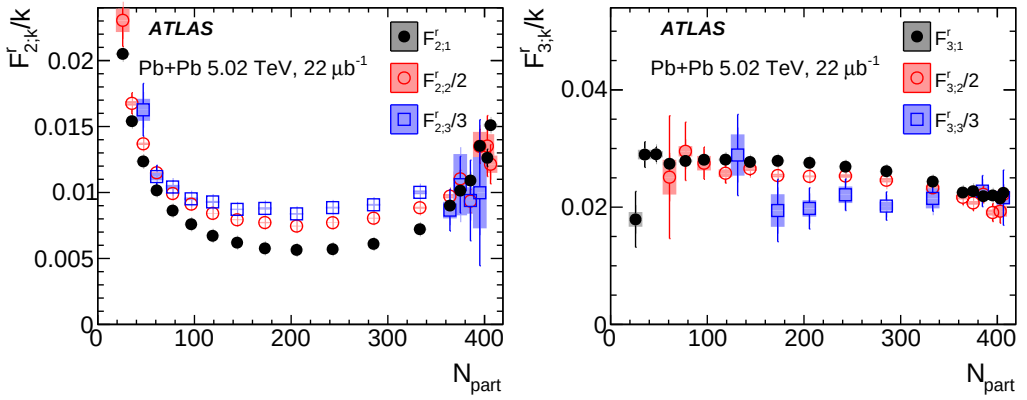

Figure 46: The values of $F^{\rm r}_{n;k}/k$ for k = 1,2 and 3 for n = 2 (left panel) and n = 3 (right panel), respectively. The error bars and shaded boxes are statistical and systematic uncertainties, respectively. The widths of the centrality intervals are not fixed but are optimized to reduce the uncertainty.

As discussed in Section 4.1, decorrelation effect can be disentangled into magnitude and event plane twist utilizing $r_{n|n;2}$ and $R_{n|n;2}$, which contains same event plane twist effect but different degrees of asymmetry.

Figure 47 compare the the two observables for second-order harmonics n = 2 and and 48 is the result for n = 3. For both harmonics $n = 2, 3$, $R_{n|n;2}$ shows a slower decreasing trend than $r_{n|n;2}$ in all centrality intervals. This is because the $R_{n|n;2}$ is mainly affected by the event-plane twist effects, while the $r_{n|n;2}$ receives contributions from both FB asymmetry and event-plane twist.

Following discussion in Section 4.1, FB asymmetry and event-plane twist are separated using the slope parameters $F^{\rm r}_{n;2}$ and $F^{\rm R}_{n;2}$ via the relation:

$$F^{\rm twi}_{n;2} = F^{\rm R}_{n;2} \ , \quad F^{\rm asy}_{n;2} = F^{\rm r}_{n;2} - F^{\rm R}_{n;2} \ . \tag{78}$$

The results are shown in Figure 49. Despite different physics origin and different decorrelation degree for v_2 and v_3, the two components are very similar to each other in the two harmonics.

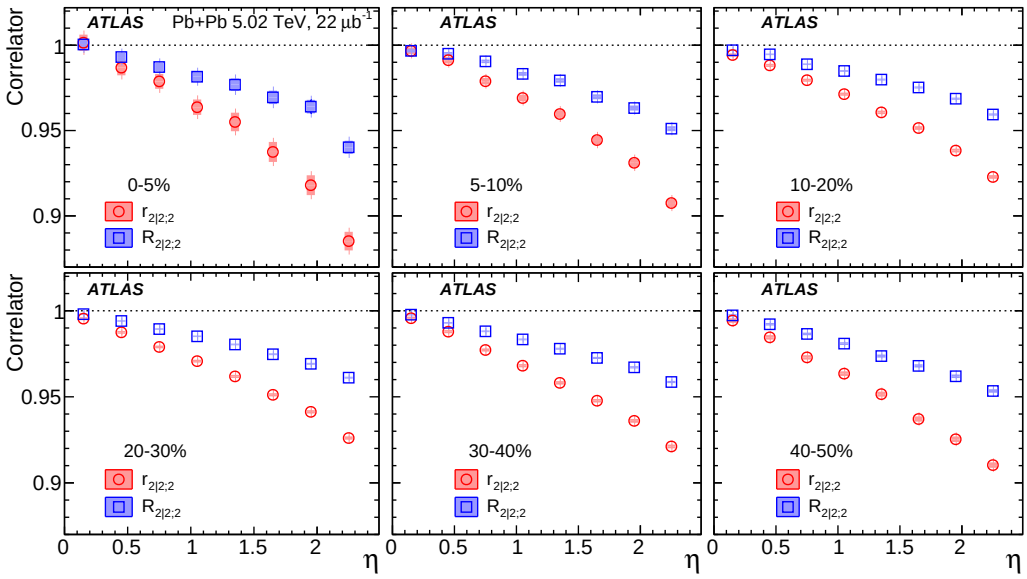

Figure 47: The $r_{2|2;2}(\eta)$ and $R_{2|2;2}(\eta)$ in various centrality intervals for Pb+Pb collisions at 5.02 TeV. The error bars and shaded boxes are statistical and systematic uncertainties, respectively.

4.7 Mixed-harmonics correlation

The hydrodynamic calculation and experimental measurements show that correlations among flow harmonics with different orders exist and only several particular combinations are meaningful observables [33, 49, 50, 54]. Therefore it is worthwhile to study how this mixed-harmonics correlation change while different harmonics are separated with a varying η gap. There are three groups of harmonics measured in this thesis work $r_{2,3|2,3}$, $r_{2,2|4}$ and $r_{2,3|5}$.

Figure 50 show $r_{2,3|2,3}$ in different centrality bins with comparison to the product of $r_{2|2;1}$ and $r_{3|3;1}$. These two observables are consistent with each other, indicating that the previously observed anti-correlation between v_2 and v_3 is a property of the entire event [54], and that longitudinal fluctuations of elliptic flow and triangular flow are uncorrelated.

Secondly, Figure 51 shows $r_{2,2|4}$ in different centrality bins, with compar-

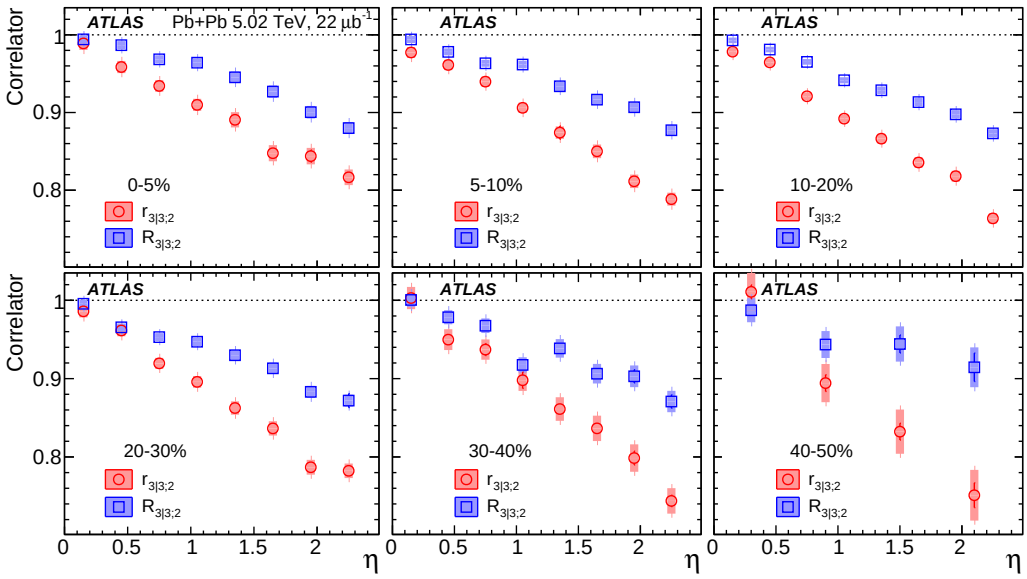

Figure 48: The $r_{3|3;2}(\eta)$ and $R_{3|3;2}(\eta)$ in various centrality intervals for Pb+Pb collisions at 5.02 TeV. The error bars and shaded boxes are statistical and systematic uncertainties, respectively. The data points in 40–50% centrality interval are rebined to reduce the uncertainty.

ison to $r_{2|2;2}$ as well as $r_{4|4;1}$. As discussed in Section 4.1, assuming that the linear and non-linear components of v_4 in Equation (51) are independent, then $r_{2,2|4}$ would be expected to be similar to $r_{2|2;2}$. The good agreement between $r_{2|2;2}$ and $r_{2,2|4}$ is confirmed in Figure 51 in different centrality bins. This figure also shows that $r_{4|4;1}$ shows stronger decorrelation effect than $r_{2|2;2}$ in all centrality intervals, suggesting that the decorrelation effects are stronger for the linear component of v_4 than for the nonlinear component (see Equation (54)).

Figure 52 shows $r_{2,3|5}$ in different centrality bins, with comparison to $r_{2,3|2,3}$ and $r_{5|5;1}$. This study checks the similar influence of the linear and nonlinear effects for v_5. The three observables $r_{2,3|2,3}$, $r_{2,3|5}$, and $r_{5|5;1}$ show similar values in all centrality intervals, albeit with large statistical uncer-

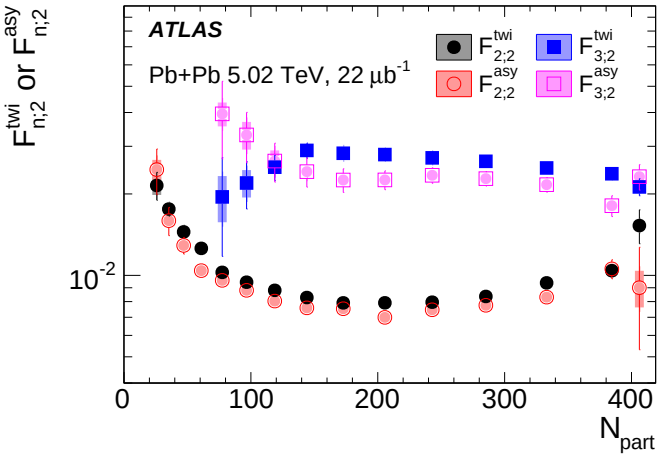

Figure 49: The estimated event-plane twist component $F^{\rm twi}_{n;2}$ and FB asymmetry component $F^{\rm asy}_{n;2}$ as a function of $N_{\rm part}$ for n = 2 and 3 for Pb+Pb collisions at 5.02 TeV. The error bars and shaded boxes are statistical and systematic uncertainties, respectively.

tainties.

The decorrelaiton measured by the three new mixed harmonics correlator in Figures 50 to 52 are also quantified by calculating the slopes in each centrality interval and presenting the results as a function of centrality. Following the example for $r_{n|n;k}$, the slopes are calculated using the linear regression method of Equation (76) and Equation (77):

$$r_{2,3|2,3} = 1 - 2F^{\rm r}_{2,3|2,3}\,\eta\,, \quad r_{2,2|4} = 1 - 2F^{\rm r}_{2,2|4}\,\eta\,, \quad r_{2,3|5} = 1 - 2F^{\rm r}_{2,3|5}\,\eta\,. \tag{79}$$

The results are summarized in Figure 53, with each panel corresponding to the slopes of distributions in Figures 50 to 52, respectively. The only significant difference is seen between $F_{4|4;1}$ and $F_{2|2;2}$ or $F_{2,2|4}$.

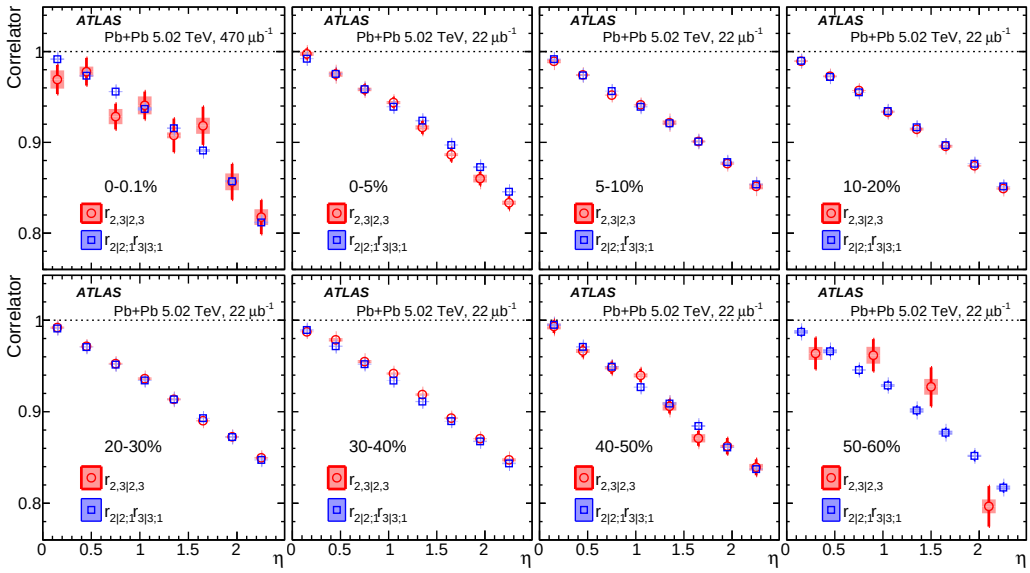

Figure 50: The $r_{2,3|2,3}$ (circles) and $r_{2|2;1}r_{3|3;1}$ (squares) as a function of η for several centrality intervals. The error bars and shaded boxes are statistical and systematic uncertainties, respectively. The $r_{2,3|2,3}$ data in the 50–60% centrality interval are rebined to reduce the uncertainty.

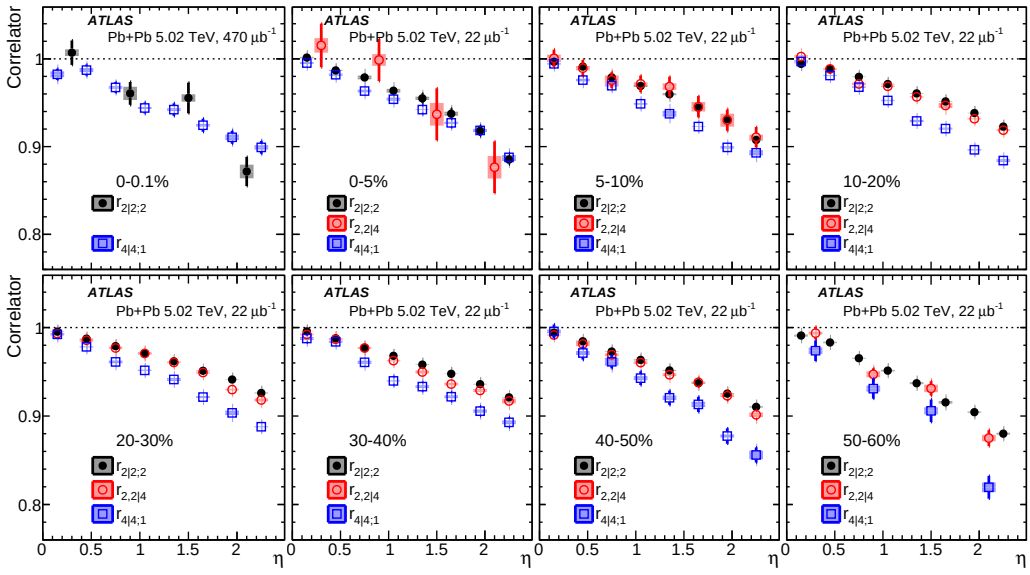

Figure 51: Comparison of $r_{2|2;2}$, $r_{2,2|4}$ and $r_{4|4;1}$ for several centrality intervals. The error bars and shaded boxes are statistical and systematic uncertainties, respectively. The data points in some centrality intervals are rebined to reduce the uncertainty.

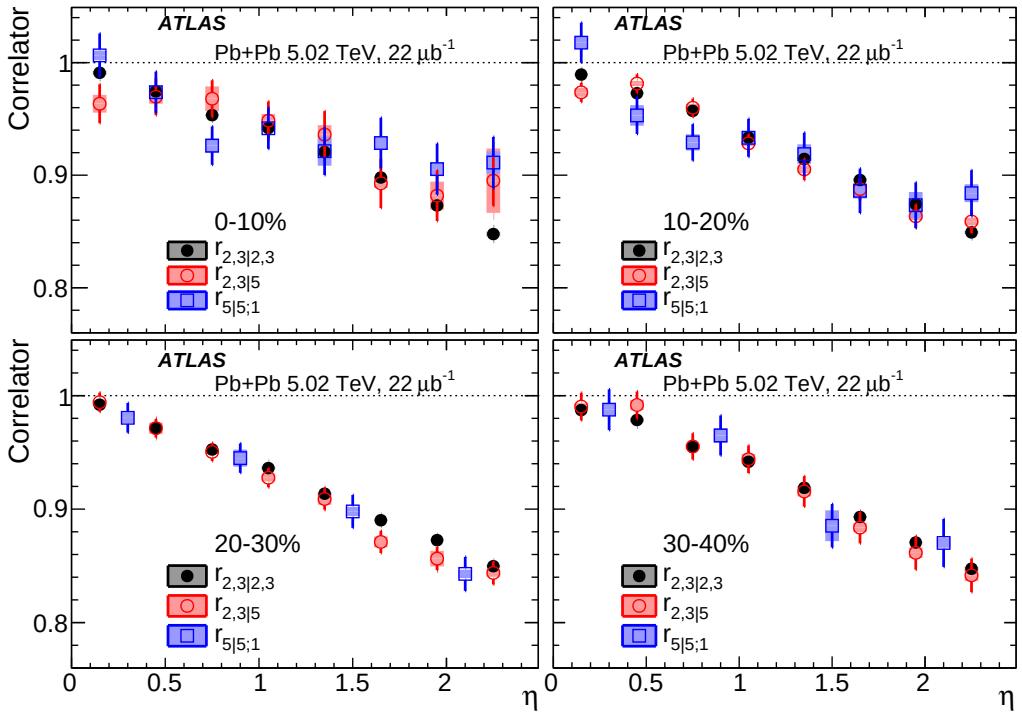

Figure 52: Comparison of $r_{2,3|2,3}$, $r_{2,3|5}$ and $r_{5|5;1}$ for several centrality intervals. The error bars and shaded boxes are statistical and systematic uncertainties, respectively. The $r_{5|5;1}$ data in some centrality intervals are rebinned to reduce the uncertainty.

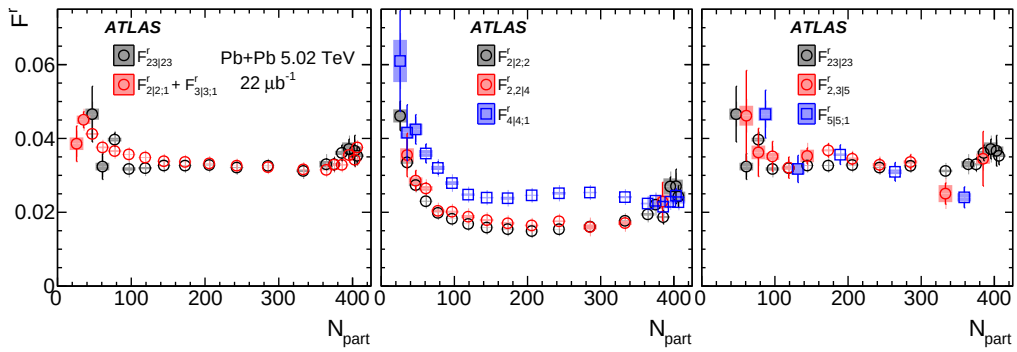

Figure 53: Comparison of the slopes of the correlators as a function of N_{part} for three groups of correlators: $r_{2,3|2,3}$ and $r_{2|2;1}r_{3|3;1}$ (for which the slope is $F_{2|2;1}$ + $F_{3|3;1}$) in Figure 50 (left panel), $r_{2|2;2}$, $r_{2,2|4}$ and $r_{4|4;1}$ in Figure 51 (middle panel), and $r_{2,3|2,3}$, $r_{2,3|5}$ and $r_{5|5;1}$ in Figure 52 (right panel). The error bars and shaded boxes are statistical and systematic uncertainties, respectively.

4.8 summary

In this analysis, the longitudinal flow decorrelation is studies using Pb+Pb data at $\sqrt{s_{\rm NN}}$ = 2.76 and 5.02 TeV, respectively. In general, the decorrelation effect is indicated by the the breakdown of factorization of two-particle azimuthal correlations into single-particle flow harmonics $\boldsymbol{V}_n$. The amount of factorization breakdown increases approximately linearly as a function of the η separation between the two particles. And the decorrelation effect is found to be stronger at lower collision energy for all harmonics, which cannot be explained entirely by the change in the beam rapidity. The decorrelation effect is found to have comparable contributions from forward-backward asymmetry of the flow magnitude and event-plane twist.

We also extended our research to study the deocrrelation of higher moments of haromincs, e.g. $k^{\rm th}$-moment of $\boldsymbol{V}_n$. The coefficient for the $k^{\rm th}$-moment of $\boldsymbol{V}_n$ scales with k for $n > 2$, but scales faster than k for $n = 2$. The coefficient for the $k^{\rm th}$-moment of $\boldsymbol{V}_n$ scales with k for $n > 2$, but scales faster than k for $n = 2$.

Lastly, we studied the longitudinal flow decorrelation between harmonic flows of different order. The correlation of $\boldsymbol{V}_2\boldsymbol{V}_3$ between two η ranges is found to factorize into the product of the correlation for $\boldsymbol{V}_2$ and the correlation for $\boldsymbol{V}_3$, suggesting that the longitudinal fluctuations of $\boldsymbol{V}_2$ and $\boldsymbol{V}_3$ are independent of each other. The correlations between $\boldsymbol{V}_4$ and $\boldsymbol{V}_2^2$ suggest that the longitudinal fluctuations of $\boldsymbol{V}_4$ have a significant nonlinear contribution from v_2, i.e. $v_4 \propto \boldsymbol{V}_2^2$. Similarly, the correlations between $\boldsymbol{V}_5$ and $\boldsymbol{V}_2\boldsymbol{V}_3$ suggest that the longitudinal fluctuations of $\boldsymbol{V}_5$ are driven by the nonlinear contribution from $\boldsymbol{V}_2\boldsymbol{V}_3$, i.e. $\boldsymbol{V}_5 \propto \boldsymbol{V}_2\boldsymbol{V}_3$. The results presented in this thesis work provide new insights into the fluctuations and correlations of harmonic flow in the longitudinal direction, which can be used to improve full three-dimensional viscous hydrodynamic models.

5 Measurements of (a)symmetric cumulants correlations in pp, p+Pb and Pb+Pb

Symmetric cumulant $\mathrm{sc}_{n,m}\{4\}$ introduced in Section 2 was first measured by ALICE collaboration in Pb+Pb [33]. Then CMS extended the analysis to small systems, pp and p+Pb, observing correlation patterns similar to Pb+Pb collisions [55]. These correlated harmonics are interpreted to provide further evidences for a long-range multi-particle collectivity in small collision systems. However, a recent study with Monte Carlo simulations shows that the CMS results, obtained with standard cumulant method, could be dominated by non-flow effects associated with jet and dijets, especially in pp collisions [56]. Thus the reanalysis of $\mathrm{sc}_{n,m}\{4\}$ using the subevent method which further suppress non-flow is necessary before the results can be used. Also we measured the proposed three particle correlator $\mathrm{ac}_n\{3\}$ using subevent method for the first time.

The majority of work presented in this chapter is published [57].

5.1 Methodology

Symmetric cumulants can be constructed in different ways, either using tracks from the whole detector, which is referred to as "standard" method, or tracks from different η region, which is referred to as "sub-event" method. Each method is summarized as below.

Cumulants in the standard method

The standard cumulant method is used by CMS and ALICE collaboration in large and small collision systems [33, 55].

Firstly, for each single event, one calculates k-particle azimuthal correlations, $\langle k \rangle$, in one event using a complex number notation [30, 31]:

$$\langle 2_n \rangle = \left\langle e^{in(\phi_1-\phi_2)} \right\rangle \ , \ \langle 3_n \rangle = \left\langle e^{i(n\phi_1+n\phi_2-2n\phi_3)} \right\rangle \ , \ \langle 4_{n,m} \rangle = \left\langle e^{in(\phi_1-\phi_2)+im(\phi_3-\phi_4)} \right\rangle \tag{80}$$

where "$\langle\rangle$" denotes average over all particle combinations in the single event, in which all the particles must be taken different, respectively.

Secondly, one use $\langle k \rangle$ to construct the event-averaged multi-particle symmetric and asymmetric cumulants

$$\mathrm{ac}_n\{3\} = \langle\langle 3_n \rangle\rangle \ , \ \mathrm{sc}_{n,m}\{4\} = \langle\langle 4_{n,m} \rangle\rangle - \langle\langle 2_n \rangle\rangle \langle\langle 2_m \rangle\rangle \ , \tag{81}$$

where the outer "$\langle\rangle$" represents a weighted event average, with the weight equal to the multiplicity in each event. Usually, the event average is done over an event ensemble with similar multiplicity in order to reduce flow fluctuation with multiplicity [30]. When the residual non-flow correlations is negligible, $\mathrm{sc}_{n,m}\{4\}$ and $\mathrm{ac}_n\{3\}$ should mostly measure the flow correlation between v_n and v_m or between v_n and v_{2n}:

$$\mathrm{ac}_n\{3\} = \left\langle v_n^2 v_{2n} \cos 2n(\Phi_n - \Phi_{2n}) \right\rangle \ , \ \mathrm{sc}_{n,m}\{4\} = \left\langle v_n^2 v_m^2 \right\rangle - \left\langle v_n^2 \right\rangle \left\langle v_m^2 \right\rangle \ . \tag{82}$$

This analysis measures three types of cumulants defined in Equation (81): $\mathrm{sc}_{2,3}\{4\}$, $\mathrm{sc}_{2,4}\{4\}$ and $\mathrm{ac}_2\{3\}$.

In data analysis, the standard cumulant is implemented in the direct cumulants framework [30, 31]. We first define Q-vectors of n^{th} order flow harmonic with moments $k = 1, 2...$ in each event [30] , along with the associated sum of weights S

$$\boldsymbol{Q}_{n,,k} = \sum_{i=1}^{M} \omega_i^k e^{in\phi_i}, \ \ S_{p,k} = \left[\sum_{i=1}^{M} w_i^k \right]^p \tag{83}$$

where w_j is the weight factor to compensate for detector effect, and is determined in the same way as in flow decorrelation analysis in Section 4. From the above definition, it immediately follows that $\boldsymbol{Q}^*_{n,,k} = \boldsymbol{Q}_{-n,,k}$.

m-particle azimuthal correlations and cumulants are then constructed in terms of the moments of the distribution of the Q-vector amplitude. For example, in the $\langle 2_n \rangle$ case, it suffices to separate the diagonal and off-diagonal

terms in $|Q_{n,1}|^2$ and $S_{2,1}$

$$|Q_{n,1}|^2 = \boldsymbol{Q}_{n,1}\boldsymbol{Q}^*_{n,1} = \sum_{i,j=1}^{M} \omega_i\omega_j e^{i(n\phi_i - n\phi_j)} \tag{84}$$
$$= \sum_{\substack{i,j=1 \\ i\neq j}}^{M} \omega_i\omega_j e^{i(n\phi_i - n\phi_j)} + S_{1,2}$$
$$S_{2,1} = \sum_{i,j=1}^{M} \omega_i\omega_j = \sum_{\substack{i,j=1 \\ i\neq j}}^{M} \omega_i\omega_j + S_{1,2} \tag{85}$$

Then the single-event observable two-particle correlation, $\langle 2_n \rangle$ is expressed as:

$$\langle 2_n \rangle = \frac{\sum_{\substack{i,j=1 \\ i\neq j}}^{M} \omega_i\omega_j e^{i(n\phi_i - n\phi_j)}}{\sum_{\substack{i,j=1 \\ i\neq j}}^{M} \omega_i\omega_j} = \frac{\boldsymbol{Q}_{n,1}\boldsymbol{Q}^*_{n,1} - S_{1,2}}{S_{2,1} - S_{1,2}} \tag{86}$$

Similarly, the three-particle correlation is

$$\langle 3_n \rangle = \frac{\boldsymbol{Q}_{n,1}\boldsymbol{Q}_{m,1}\boldsymbol{Q}^*_{2n,1} - \boldsymbol{Q}_{2n,2}\boldsymbol{Q}_{-2n,1} - 2\boldsymbol{Q}_{n,1}\boldsymbol{Q}_{n,2} + 2S_{1,3}}{S_{3,1} - 3S_{1,1}S_{1,2} + 2S_{1,3}} \tag{87}$$

and four-particle correlation is

$$\langle 4_{n,m} \rangle = \frac{|Q_{m,1}|^2|Q_{n,1}|^2 - 2\mathrm{Re}|\boldsymbol{Q}_{m+n,2}\boldsymbol{Q}^*_{m,1}\boldsymbol{Q}^*_{n,1}| - 2\mathrm{Re}|\boldsymbol{Q}_{m,1}\boldsymbol{Q}^*_{m-n,2}\boldsymbol{Q}^*_{n,1}| + |Q_{m+n,2}|^2}{S_{4,1} - 6S_{1,2}S_{2,1} + 3S_{2,2} + 8S_{1,3}S_{1,1} - 6S_{1,4}} \tag{88}$$
$$+ \frac{|Q_{m-n,2}|^2 - s_{1,2}(|Q_{m,1}|^2 + |Q_{n,1}|^2) + 4\mathrm{Re}|\boldsymbol{Q}_{m,3}\boldsymbol{Q}^*_{m,1} + \boldsymbol{Q}_{n,3}\boldsymbol{Q}^*_{n,1}| + S_{2,2} - 6S_{1,4}}{S_{4,1} - 6S_{1,2}S_{2,1} + 3S_{2,2} + 8S_{1,3}S_{1,1} - 6S_{1,4}}$$

In the "standard" cumulant method described above, all k-particle multiplets involved in $\langle k_n \rangle$ and $\langle k_{n,m} \rangle$ are selected using tracks in the entire Inner Detector (ID) acceptance of $|\eta| < \eta_{\max} = 2.5$, as illustrated on Figure 54. The non-flow contribution to $\mathrm{sc}_{n,m}\{4\}$ are negligible by in A+A collisions, but are proven to be strong in small system pp and p+Pb in a study using HIJING and PYTHIA, which only have non-flow [56].

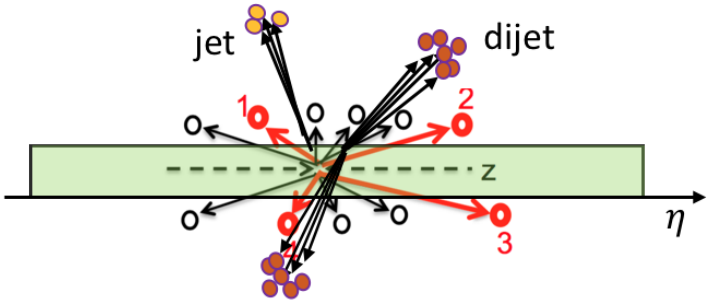

Figure 54: Schematic view of the η coverage of the Inner Detector.

Cumulants in the subevent method

In the subevent method, the tracks from ID are divided into several subevent based on the η. Each subevent covers a unique η interval. Since typically non-flow particles are correlated within a narrow region in η, the non-flow correlation should be weakened when one implement a pesudorapidity gap by require particles are from different η interval. Under this idea, the (a)symmetric cumulant are constructed by only correlating tracks between different subevents.

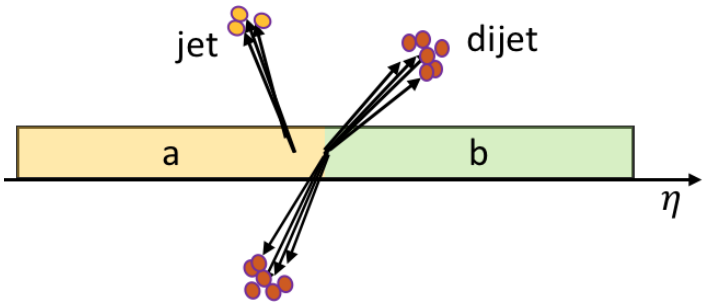

Figure 55: Schematic view of the partition of Inner Detector in two-subevent method.

The first type is the two-subevent cumulant method, where the tracks are divided into two region $-\eta_{\max} < \eta_a < 0$ and $0 \leq \eta_b < \eta_{\max}$, as illustrated

in Figure 55. The two subevents are labelled by a and b separately. The per-event k-particle azimuthal correlations are evaluated as:

$$\langle 2_n \rangle_{a|b} = \left\langle e^{in(\phi_1^a - \phi_2^b)} \right\rangle \tag{89}$$
$$= \frac{\boldsymbol{Q}_n^a \boldsymbol{Q}_n^{b*}}{S_{1,1}^a S_{1,1}^b}$$
$$\langle 3_n \rangle_{2a|b} = \left\langle e^{i(n\phi_1^a + n\phi_2^a - 2n\phi_3^b)} \right\rangle \tag{90}$$
$$= \frac{(\boldsymbol{Q}_{2,1}^a \boldsymbol{Q}_{2,1}^a - \boldsymbol{Q}_{4,2}^a)\boldsymbol{Q}_{4,1}^{b*}}{(S_{2,1}^a - S_{1,2}^a)S_{1,1}^b}$$
$$\langle 4_{n,m} \rangle_{2a|2b} = \left\langle e^{in(\phi_1^a - \phi_2^b) + im(\phi_3^a - \phi_4^b)} \right\rangle \tag{91}$$
$$= \frac{(\boldsymbol{Q}_n^a \boldsymbol{Q}_m^a - S_{1,2}^a \boldsymbol{Q}_{n+m,1}^a)(\boldsymbol{Q}_{n,1}^b \boldsymbol{Q}_{m,1}^b - S_{1,2}^b \boldsymbol{Q}_{n+m,1}^b)^*}{(S_{2,1}^a - S_{1,2}^a)(S_{2,1}^b - S_{1,2}^b)}$$

Here the three- and four-particle cumulants are defined as:

$$\mathrm{ac}_n^{2a|b}\{3\} = \langle\langle \{3\}_n \rangle\rangle_{2a|b} \ , \ \mathrm{sc}_{n,m}^{2a|2b}\{4\} = \langle\langle \{4\}_{n,m} \rangle\rangle_{2a|2b} - \langle\langle \{2\}_n \rangle\rangle_{a|b} \langle\langle \{2\}_m \rangle\rangle_{a|b} \ . \tag{92}$$

This two-subevent implementation effectively suppresses correlations within a single jet (intra-jet correlations), since each particles from one jet usually usually fall in one subevent.

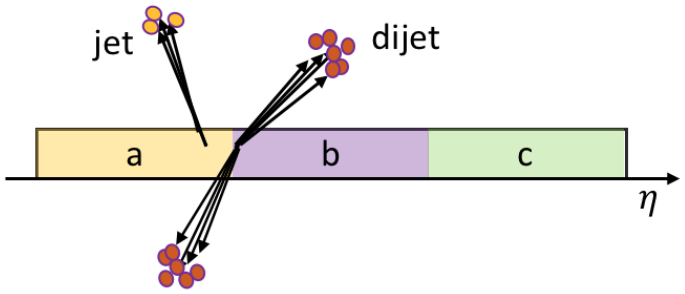

Figure 56: Schematic view of the partition of Inner Detector in three-subevent method.

The third type is the three-subevent cumulant methods. Similar to 2 subevent method, here the pseudorapidity acceptance $-2.5 < \eta < 2.5$ is divided into three subevents a, b and c, each covering one third of the η range,

as illustrated in Figure 56.The per-event k-particle azimuthal correlations are evaluated as:

$$\langle 3_n \rangle_{a,b|c} = \left\langle e^{i(n\phi_1^a + n\phi_2^b - 2n\phi_3^c)} \right\rangle = \frac{\boldsymbol{Q}_{n,1}^a \boldsymbol{Q}_{n,1}^b * \boldsymbol{Q}_{2n,1}^{c*}}{S_{1,1}^a S_{1,1}^b S_{1,1}^c} \tag{93}$$

$$\langle 4_{n,m} \rangle_{a,b|2c} = \left\langle e^{in(\phi_1^a - \phi_2^c) + im(\phi_3^b - \phi_4^c)} \right\rangle = \frac{(\boldsymbol{Q}_{n,1}^a \boldsymbol{Q}_{m,1}^a - S_{1,2}^a \boldsymbol{Q}_{n+m,1}^a) \boldsymbol{Q}_{n,1}^{b*} \boldsymbol{Q}_m^{c*}}{(S_{2,1}^a - S_{1,2}^a) S_{1,1}^b S_{1,1}^c} \tag{94}$$

Here the three- and four-particle cumulants are defined as:

$$\mathrm{ac}_n^{a,b|c}\{3\} = \langle\langle 3_n \rangle\rangle_{a,b|c} \ , \ \mathrm{sc}_{n,m}^{a,b|2c}\{4\} = \langle\langle 4_{n,m} \rangle\rangle_{a,b|2c} - \langle\langle 2_n \rangle\rangle_{a|c} \langle\langle 2_m \rangle\rangle_{b|c} \ . \tag{95}$$

Compared to two-subevent method, the three-subevent method also efficiently suppresses the inter-jet correlations associated with dijets, since a dijet event usually produce particles in at most two subevents, as seen in Figure 56. One can also swap the label η range for subevent a with subevent b or c, which should give the same result (when flow decorrelation effect is not consider). To maximize the statistical precision, these results are averaged to obtain the final value in this thesis.

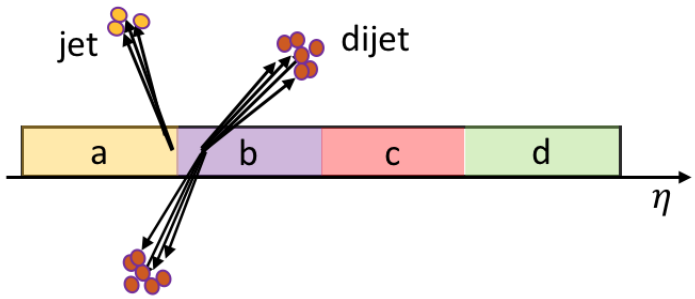

Figure 57: Schematic view of the partition of Inner Detector in four-subevent method.

The forth type is the four-subevent cumulant method, which is only applicable for the symmetric cumulants $\mathrm{sc}_{n,m}\{4\}$. Each of the four subevents a, b, c, and d covers one quarter of the η range, as illustrated in Figure 57. Then The multi-particle azimuthal correlations and cumulants are then calculated as:

$$\langle 4_{n,m}\rangle_{a,b|c,d} = \left\langle e^{in(\phi_1^a-\phi_2^c)+im(\phi_3^b-\phi_4^d)}\right\rangle = \frac{\boldsymbol{Q}^a_{n,1}\boldsymbol{Q}^b_{n,1}\boldsymbol{Q}^{c*}_{n,1}\boldsymbol{Q}^{d*}_{n,1}}{S^a_{1,1}S^b_{1,1}S^c_{1,1}S^d_{1,1}} \tag{96}$$

$$\mathrm{sc}^{a,b|c,d}_{n,m}\{4\} = \langle\langle 4_{n,m}\rangle\rangle_{a,b|c,d} - \langle\langle 2_n\rangle\rangle_{a|c}\langle\langle 2_m\rangle\rangle_{b|d} \tag{97}$$

The four-subevent method should further suppress the residual non-flow contributions than all the other method. We can also swap the η ranges for the four subevents and average these results to gain batter statistical precision.

Normalized cumulants

The positive and negative sign of $\mathrm{sc}_{n,m}\{4\}$ and $\mathrm{ac}_n\{3\}$ is an indication of positive correlation or negative correlation between different flow harmonics. On the other hand, the absolute value of $\mathrm{sc}_{n,m}\{4\}$ and $\mathrm{ac}_n\{3\}$ is deemed as the strength of flow correlations, and one expect the signal is very close to zero if the correlation is very loose.

Although the symmetric cumulant $\mathrm{sc}_{n,m}\{4\}$ reflects the nature of the correlation between v_n and v_m, the magnitude of the $\mathrm{sc}_{n,m}\{4\}$ also depends on the square of single flow harmonics v_n^2 and v_m^2 (see Equation (82)) .

However the single flow magnitude v_n itself is a function of multiplicity in most case, then the magnitude of the $\mathrm{sc}_{n,m}\{4\}$ is also affected by the square of single flow harmonics v_n^2 and v_m^2 (see Equation (82)). This dependence on the single flow harmonics can be scaled out via the normalized cumulants [49,

58]:

$$\mathrm{nsc}_{2,3}\{4\} = \frac{\mathrm{sc}_{2,3}\{4\}}{v_2\{2\}^2 v_3\{2\}^2} = \frac{\langle v_2^2 v_3^2\rangle}{\langle v_2^2\rangle\langle v_3^2\rangle} - 1\,, \tag{98}$$

$$\mathrm{nsc}_{2,4}\{4\} = \frac{\mathrm{sc}_{2,4}\{4\}}{v_2\{2\}^2 v_4\{2\}^2} = \frac{\langle v_2^2 v_4^2\rangle}{\langle v_2^2\rangle\langle v_4^2\rangle} - 1\,, \tag{99}$$

$$\mathrm{nac}_{2}\{3\} = \frac{\mathrm{ac}_{2}\{3\}}{v_2\{2\}^2\sqrt{v_4\{2\}^2}} = \frac{\langle v_2^2 v_4 \cos 4(\Phi_2 - \Phi_4)\rangle}{\langle v_2^2\rangle\sqrt{\langle v_4^2\rangle}}\,, \tag{100}$$

where the $v_n\{2\}^2 = \langle v_n^2\rangle$ are flow harmonics obtained using a two-particle correlation method based on a peripheral subtraction technique [59, 60], which will be discussed in Section 6. The normalized cumulants should reflect the nature of the correlation between v_n and v_m.

5.2 Datasets

This analysis is based on ATLAS datasets corresponding to integrated luminosities of 0.9 pb^{-1} of pp data recorded at $\sqrt{s_{\mathrm{NN}}}$ = 13 TeV, 28 nb^{-1} of p+Pb data recorded at $\sqrt{s_{\mathrm{NN}}}$ = 5.02 TeV, and 7 μb^{-1} of Pb+Pb data at $\sqrt{s_{\mathrm{NN}}}$ = 2.76 TeV. The 2.76 TeV Pb+Pb data were collected in 2010. The p+Pb data were mainly collected in 2013, but also include 0.3 nb^{-1} of data collected in 2016, which increase the number of events at moderate multiplicity. During both p+Pb runs, the LHC was configured to provide a 4~TeV proton beam and a 1.57~TeV per-nucleon Pb beam, which produced collisions at $\sqrt{s_{\mathrm{NN}}}$ = 5.02 TeV, with a rapidity shift of 0.465 of the nucleon–nucleon centre-of-mass frame towards the proton beam direction relative to the ATLAS rest frame. The direction of the Pb beam is always defined to have negative pseudorapidity. The 13 TeV pp data were collected during several special runs of the LHC with low pile-up in 2015 and 2016. A summary of the datasets used in this analysis is shown in Table 7.

For each collision system, the multi-particle cumulants are calculated using the so-called reference particles. Two selections of reference particles are considered, for which the multiplicity M_{ref} in a given event is the number

Table 7: The list of datasets used in symmetric cumulant analysis.

	Pb+Pb	p+Pb	pp
Integrated luminosity (year)	7 μb^{-1} (2010)	28 nb^{-1} (2013)	0.07 pb^{-1} (2015)
		0.3 nb^{-1} (2016)	0.84 pb^{-1} (2016)

of reconstructed charged particles with $|\eta| < 2.5$ and with corresponding p_{T} ranges: $0.3 < p_{\mathrm{T}} < 3$ GeV or $0.5 < p_{\mathrm{T}} < 5$ GeV. Figure 58 shows the multiplicity (not corrected for tracking efficiency) distributions for the reconstructed charged-particle tracks with $0.3 < p_{\mathrm{T}} < 3$ GeV for all collision systems. The observed discontinuities reflect the offline selection requirement of at least 90% efficiency for the high multiplicity triggers.

More details about the dataset, track selection and tracking efficiency are in Refs. [57, 61].

5.3 Systematic uncertainties

The evaluation of the systematic uncertainties follows closely the procedure established for the four-particle cumulants $c_n\{4\}$ and is detailed in Ref. [62]. The main sources of systematic uncertainties are related to the detector azimuthal non-uniformity, track selection, track reconstruction efficiency, trigger efficiency and pile-up. Due to the relatively poor statistics and larger non-flow effects, the systematic uncertainties are typically larger in pp collisions. The systematic uncertainties are also generally larger, in percentage, for four-particle cumulants $\mathrm{sc}_{n,m}\{4\}$ than for the three-particle cumulants $\mathrm{ac}_2\{3\}$, since the $|\mathrm{sc}_{n,m}\{4\}|$ values are much smaller than those for $\mathrm{ac}_2\{3\}$. The systematic uncertainties are generally similar among the two- and three- and four-subevent methods, but are different from those for the standard method, which is strongly influenced by non-flow correlations. The following discussion focuses on the three-subevent method, which is the default method used to present the final results.

The effect of detector azimuthal non-uniformity is accounted for using

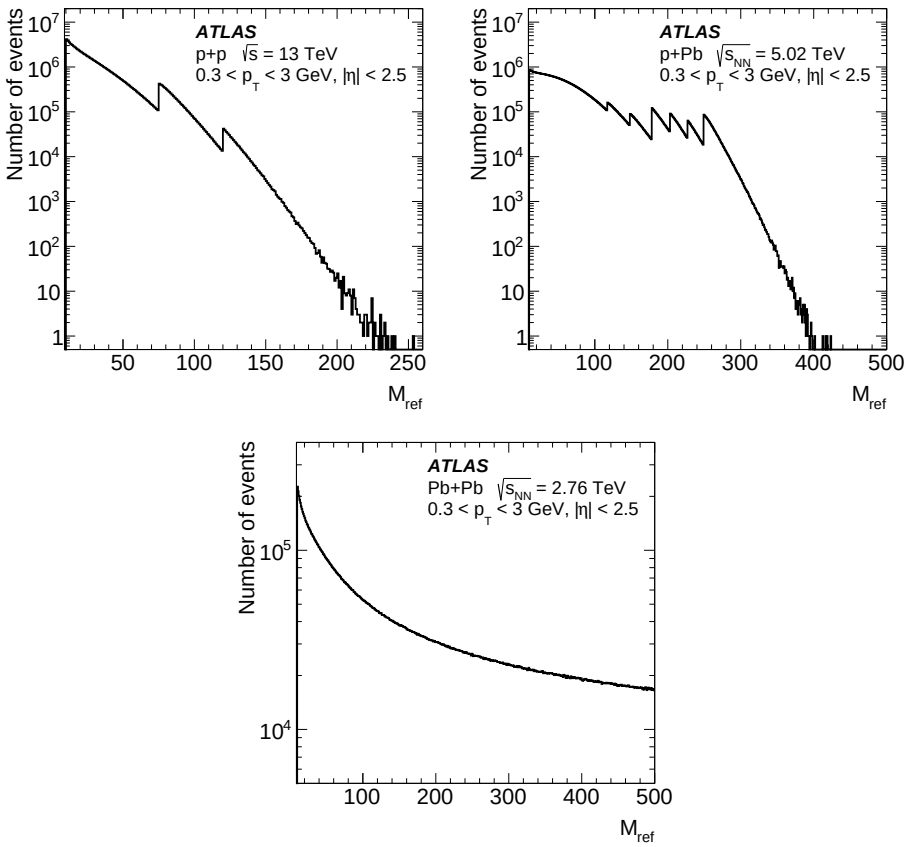

Figure 58: Distributions of the reference particle multiplicity for particles with $0.3 < p_{\mathrm{T}} < 3$ GeV from pp, p+Pb and low-multiplicity Pb+Pb collisions

.

the weight factor $w_i(\phi, \eta)$ in Equation (83). The impact of the weighting procedure is studied by fixing the weight to unity and repeating the analysis. The results are mostly consistent with the nominal results. The corresponding uncertainties for $\mathrm{sc}_{n,m}\{4\}$ vary in the range of 0–4%, 0–2% and 1–2% in pp, p+Pb and Pb+Pb collisions, respectively. The uncertainties for $\mathrm{ac}_2\{3\}$ vary in the range of 0–2% in pp collisions, and 0–1% in p+Pb and Pb+Pb collisions, respectively.

The systematic uncertainty associated with the track selection is estimated by tightening the $|d_0|$ and $|z_0 \sin\theta|$ requirements. They are each varied from the default requirement of less than 1.5 mm to less than 1 mm. In p+Pb and Pb+Pb collisions, the requirement on the significance of impact parameters, $|d_0|/\sigma_{d_0}$ and $|z_0 \sin\theta|/\sigma_{z_0}$ are also varied from less than 3 to less than 2. For each variation, the tracking efficiency is re-evaluated and the analysis is repeated. For $\mathrm{ac}_2\{3\}$, which has a large flow signal, the differences from the nominal results are observed to be less than 2% for all collision systems. For $\mathrm{sc}_{n,m}\{4\}$, for which the signal is small, the differences from the nominal results are found to be in the range of 2–10% in pp collisions, 2–7% in p+Pb collisions and 2–4% in Pb+Pb collisions. The differences are smaller for results obtained for $0.5 < p_{\mathrm{T}} < 5$ GeV than those obtained for $0.3 < p_{\mathrm{T}} < 3$ GeV.

Previous measurements indicate that the azimuthal correlations (both the flow and non-flow components) have a strong dependence on p_{T}, but a relatively weak dependence on η [27, 60]. Therefore, p_{T}-dependent systematic effects in the track reconstruction efficiency could affect the cumulant values. The uncertainty in the track reconstruction efficiency is mainly due to differences in the detector conditions and material description between the simulation and the data. The efficiency uncertainty varies between 1% and 4%, depending on track η and p_{T} [60, 61]. Its impact on multi-particle cumulants is evaluated by repeating the analysis with the tracking efficiency varied up and down by its corresponding uncertainty as a function of track p_{T}. For the standard cumulant method, which is more sensitive to jets and dijets, the evaluated uncertainty amounts to 2–6% in pp collisions and less than 2% in p+Pb collisions for $\langle N_{\mathrm{ch}} \rangle > 100$. For the subevent methods, the evaluated uncertainty is typically less than 3% for most of the $\langle N_{\mathrm{ch}} \rangle$ ranges.

Most events in pp and p+Pb collisions are collected with the high multiplicity (HMT) triggers with several online $N_{\mathrm{ch}}^{\mathrm{rec}}$ thresholds. In order to estimate the possible bias due to trigger inefficiency as a function of $\langle N_{\mathrm{ch}} \rangle$, the offline $N_{\mathrm{ch}}^{\mathrm{rec}}$ requirements are changed such that the HMT trigger effi-

ciency is at least 50% or 80%. The results are obtained independently for each variation. These results are found to be consistent with each other for the subevent methods, and show some differences for the standard cumulant method in the low $\langle N_{\mathrm{ch}} \rangle$ region. The nominal analysis is performed using the 50% efficiency selection and the differences between the nominal results and those from the 80% efficiency selection are included in the systematic uncertainty. The changes for pp collisions are in the range of 5–15% for $\mathrm{sc}_{2,3}\{4\}$, 2–8% for $\mathrm{sc}_{2,4}\{4\}$ and 1–5% for $\mathrm{ac}_2\{3\}$. The ranges for p+Pb collisions are much smaller due to the much sharper turn-on of the trigger efficiency and larger signal: they are estimated to be 1–3% for $\mathrm{sc}_{2,3}\{4\}$, 2–4% for $\mathrm{sc}_{2,4}\{4\}$ and 1–2% for $\mathrm{ac}_2\{3\}$.

In this analysis, a pile-up rejection criterion is applied to reject events containing additional vertices in pp and p+Pb collisions. In order to check the impact of residual pile-up, the analysis is repeated without the pile-up rejection criterion. No differences are observed in p+Pb collisions, as is expected since the μ values in p+Pb are modest. For the 13 TeV pp dataset, the differences with and without pile-up rejection are in the range of 0–7% for $\mathrm{sc}_{2,3}\{4\}$, 2–15% for $\mathrm{sc}_{2,4}\{4\}$ and 2–3% for $\mathrm{ac}_2\{3\}$. As a cross-check, the pp data are divided into two samples with approximately equal number of events based on the μ value: $\mu > 0.4$ and $\mu < 0.4$, and the results are compared. No systematic differences are observed between the two independent datasets.

The systematic uncertainties from different sources are added in quadrature to determine the total systematic uncertainty. In p+Pb and Pb+Pb collisions, the total uncertainties are in the range of 3–8% for $\mathrm{sc}_{2,3}\{4\}$, 1–5% for $\mathrm{sc}_{2,4}\{4\}$ and 1–4% for $\mathrm{ac}_2\{3\}$. In pp collisions, the total uncertainties are larger, mainly due to larger non-flow contribution, larger pile-up and the less sharp turn-on of the HMT triggers. They are in the ranges of 10–20% for $\mathrm{sc}_{2,3}\{4\}$, 10–20% for $\mathrm{sc}_{2,4}\{4\}$ and 2–5% for $\mathrm{ac}_2\{3\}$. The total systematic uncertainties are generally smaller than the statistical uncertainties.

The $v_n\{2\}$ values used to obtain normalized cumulants from Eqs. (98)–(100) will be discussed in later Section 6. The uncertainties of normalized

cumulants are obtained by propagation of the uncertainties from the original cumulants and $v_n\{2\}$, taking into account that the correlated systematic uncertainties partially cancel out.

5.4 Comparison between standard and subevent methods

5.4.1 $\mathrm{sc}_{2,3}\{4\}$

The top row of Figure 59 compares the $\mathrm{sc}_{2,3}\{4\}$ from the standard, two-, three- and four-subevent methods from pp collisions. In the left panel, particles are selected with range $0.3 < p_{\mathrm{T}} < 3$ GeV, while on the right panel range $0.5 < p_{\mathrm{T}} < 5$ GeV is applied.

Firstly, for the standard method, one observes positive signal over the full $\langle N_{\mathrm{ch}} \rangle$ range in each p_{T} range. And the standard method becomes larger at lower $\langle N_{\mathrm{ch}} \rangle$ or at higher p_{T}, where the non-flow correlation is more dominant and stronger. These behaviors suggest that the $\mathrm{sc}_{2,3}\{4\}$ values from the standard method in pp collisions is strongly influenced by non-flow effects in all $\langle N_{\mathrm{ch}} \rangle$ and p_{T} ranges.

In contrast, the values from the subevent methods are negative over the full $\langle N_{\mathrm{ch}} \rangle$ range.These values are slightly more negative at lowest $\langle N_{\mathrm{ch}} \rangle$ and also more negative at higher p_{T}. For $0.3 < p_{\mathrm{T}} < 3$ GeV, the two-, three- and four-subevent method gives consistent results. For the high p_{T} region of $0.5 < p_{\mathrm{T}} < 5$ GeV, results from the two-subevent method are systematically lower than the three- and four-subevent methods, suggesting that the two-subevent method may be affected by negative non-flow contributions. Such negative non-flow correlation has been observed in a PYTHIA8 calculation [56].

The middle row of Figure 59 shows the $\mathrm{sc}_{2,3}\{4\}$ from p+Pb collisions. At $\langle N_{\mathrm{ch}} \rangle > 140$, all four methods have negative and consistent values, indicating non-flow is very weak the the measurement reflects the genuine long-range collective correlations. At $\langle N_{\mathrm{ch}} \rangle < 140$, the standard method keeps increasing and remains positive at lower $\langle N_{\mathrm{ch}} \rangle$, which indicate this multiplicity the

$\mathrm{sc}_{2,3}\{4\}$ gets significant contribution from non-flow correlations. In contrast, $\mathrm{sc}_{2,3}\{4\}$ from various subevent methods are still negative and consistent with each other at $\langle N_{\mathrm{ch}} \rangle < 140$, suggesting that non-flow contribution is weak in subevent methods.

The bottom row of Figure 59 shows the $\mathrm{sc}_{2,3}\{4\}$ from low-multiplicity Pb+Pb collisions. The results are consistent among all four methods across most of the $\langle N_{\mathrm{ch}} \rangle$ range, although the results from the standard method are systematically larger. In the low $\langle N_{\mathrm{ch}} \rangle$ region, where the non-flow is expected to be significant, the results have too large uncertainties to distinguish between different methods.

5.4.2 $\mathrm{sc}_{2,4}\{4\}$

The top row of Figure 60 compares the $\mathrm{sc}_{2,4}\{4\}$ from the standard, two-, three- and four-subevent methods from pp collisions. In the left panel, particles are selected with range $0.3 < p_{\mathrm{T}} < 3$ GeV, while on the right panel range $0.5 < p_{\mathrm{T}} < 5$ GeV is applied. Positive values are seen in from all four methods over the full $\langle N_{\mathrm{ch}} \rangle$ range in each p_{T} range. However, the values from the standard method are much larger than the subevent methods and also exhibit a much faster uptrend towards the lower $\langle N_{\mathrm{ch}} \rangle$ region. These behaviors are consistent with the expectation that the standard method is more affected by dijets. As for the subevent methods, they are consistent for $\langle N_{\mathrm{ch}} \rangle > 100$ and split at low $\langle N_{\mathrm{ch}} \rangle$ region. In general, the two-subevent gives a slight larger value than three- or four-subevent methods, and the difference becomes significant at low $\langle N_{\mathrm{ch}} \rangle$ region. Within the statistical uncertainties of the measurement, no differences are observed between the three- and four-subevent methods. This comparison suggests that the residual non-flow from dijets is still not totally negligible in pp collisions since the flow signal is weak here. And three or more subevents are more robust from the non-flow correlations contamination over the measured $\langle N_{\mathrm{ch}} \rangle$ range.

The middle row of Figure 60 shows $\mathrm{sc}_{2,4}\{4\}$ in p+Pb collisions. Firstly, we see the standard method gives significant larger values than the subevent

methods over the full $\langle N_{\rm ch}\rangle$ range. However, no differences are observed among various subevent methods, except in $\langle N_{\rm ch}\rangle < 40$, which may reflect some residual non-flow correlations and the real difference could change since statistical uncertainties are also very huge here. These results suggest that the in p+Pb systems, the standard method is still biased by large contributions from non-flow correlations at low $\langle N_{\rm ch}\rangle$, and this contribution may not vanish even at large $\langle N_{\rm ch}\rangle$ values. In contrast, subevent event methods are robust measurements in $\langle N_{\rm ch}\rangle > 40$.

The bottom row of Figure 60 shows $\mathrm{sc}_{2,4}\{4\}$ from Pb+Pb collisions. The difference between standard method and subevent methods are not that big but still clear and exist at all the $\langle N_{\rm ch}\rangle$ range. This difference varies slowly with $\langle N_{\rm ch}\rangle$, similar to the behavior observed for the p+Pb collisions in the large $\langle N_{\rm ch}\rangle$ region. This increase reflects the known fact that the v_2 increases with $\langle N_{\rm ch}\rangle$ in Pb+Pb collisions.

As a summary, Figure 60 show that $\mathrm{sc}_{2,4}\{4\}$ is positive for all the three collision systems, which indicates that v_2 and v_4 are positive correlated.

5.4.3 $\mathrm{ac}_2\{3\}$

Results for asymmetric cumulant $\mathrm{ac}_2\{3\}$ is presented in Figure 61. $\mathrm{ac}_2\{3\}$ also measures v_2 and v_4 correlation like $\mathrm{sc}_{2,4}\{4\}$. It is a three particle correlator and is more prone to non-flow contamination, but the benefit is that the underlying flow signal is much stronger than $\mathrm{sc}_{2,4}\{4\}$. In this figure we will show results from three different methods: the standard, the two-subevent, and the three-subevent methods, in pp, p+Pb and Pb+Pb collisions.

The top row in Figure 61 shows the results in pp collisions in $0.3 < p_{\rm T} < 3$ GeV (left panel) and $0.5 < p_{\rm T} < 5$ GeV (right panel). The results are positive for the standard, two-subevent, and three-subevent methods. Here, we see the standard method are much larger than those from the subevent methods, consistent with the expectation that the standard method is more affected by non-flow correlations from dijets. Two-subevent and three-subevent methods are consistent at $\langle N_{\rm ch}\rangle > 100$ and become different at lower multiplicity. The

$ac_2\{3\}$ values from the three-subevent method show a slight increase for $\langle N_{\rm ch}\rangle < 40$ but are nearly constant for $\langle N_{\rm ch}\rangle > 40$. This behavior suggests that in the three-subevent method, the non-flow contribution may play some role at $\langle N_{\rm ch}\rangle < 40$, but is negligible for $\langle N_{\rm ch}\rangle > 40$. Therefore, the $ac_2\{3\}$ from the three-subevent method supports the existence of a three-particle long-range collective flow that is nearly $\langle N_{\rm ch}\rangle$-independent in pp collisions, consistent with the $\langle N_{\rm ch}\rangle$-independent behavior of v_2 and v_4 previously observed from the two-particle correlation analysis [60].

The middle and bottom rows of Figure 61 show $ac_2\{3\}$ from p+Pb and Pb+Pb collisions, respectively.

In general, the standard method shows a clear difference with subevent methods, and the subevent methods are consistent in except in the low multiplicity region. At $\langle N_{\rm ch}\rangle < 60$, non-flow correlations dominates and contribute positively to the correlator. At $\langle N_{\rm ch}\rangle > 60$ region, the influence of non-flow contributions is very small for in the subevent methods in both collision systems. Therefor the $\langle N_{\rm ch}\rangle$ dependence of $ac_2\{3\}$ reflects the $\langle N_{\rm ch}\rangle$ dependence of the v_2 and v_4, which increase with $\langle N_{\rm ch}\rangle$, and the increase is stronger in Pb+Pb collisions. This is consistent with previous observations that v_2 and v_4 increase with $\langle N_{\rm ch}\rangle$ more strongly in Pb+Pb than in p+Pb collisions [61].

The results presented above suggest that the three-subevent method is sufficient to suppress most of the non-flow effects. It is therefore used as the default method for the discussion below.

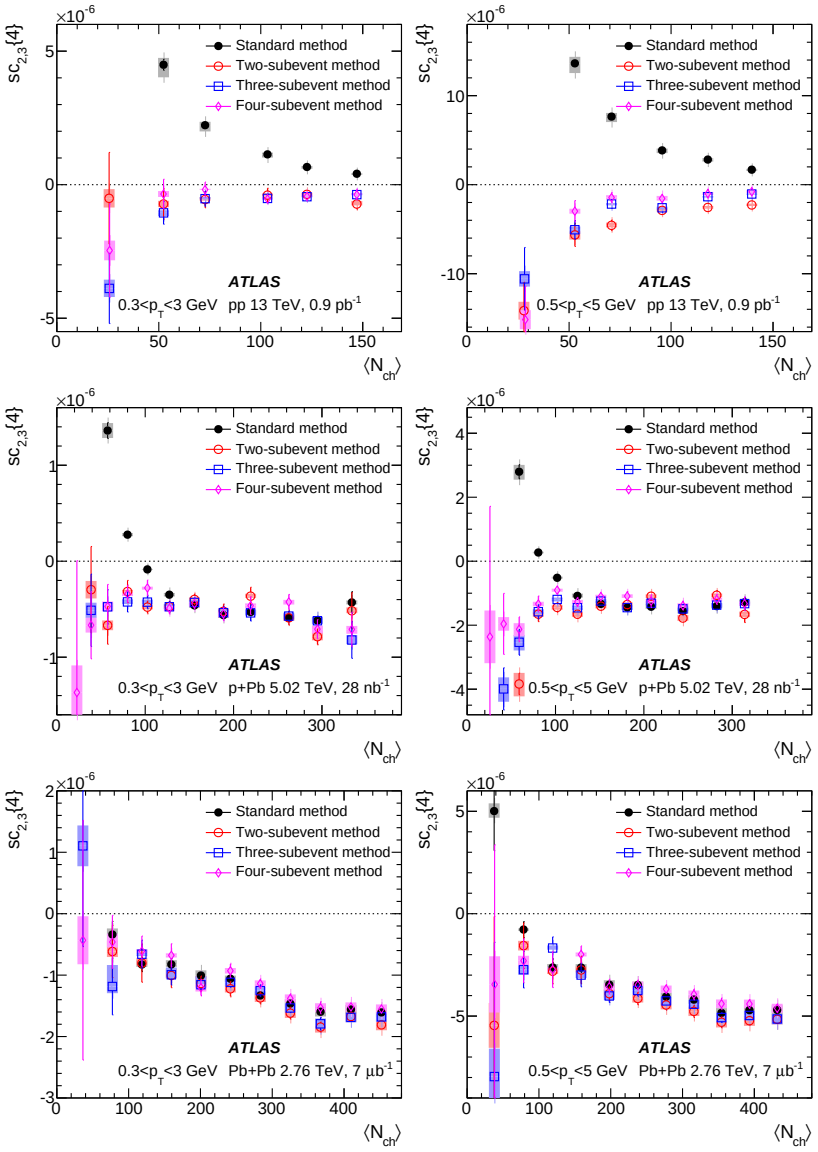

Figure 59: The symmetric cumulant $\mathrm{sc}_{2,3}\{4\}$ as a function of $\langle N_{\mathrm{ch}} \rangle$ for $0.3 < p_{\mathrm{T}} < 3$ GeV (left panels) and $0.5 < p_{\mathrm{T}} < 5$ GeV (right panels) obtained for pp collisions (top row), p+Pb collisions (middle row) and low-multiplicity Pb+Pb collisions (bottom row). In each panel, the $\mathrm{sc}_{2,3}\{4\}$ is obtained from the standard method (filled symbol), the two-subevent method (open circles), three-subevent method (open squares) and four-subevent method (open diamonds). The error bars and shaded boxes represent the statistical and systematic uncertainties, respectively.

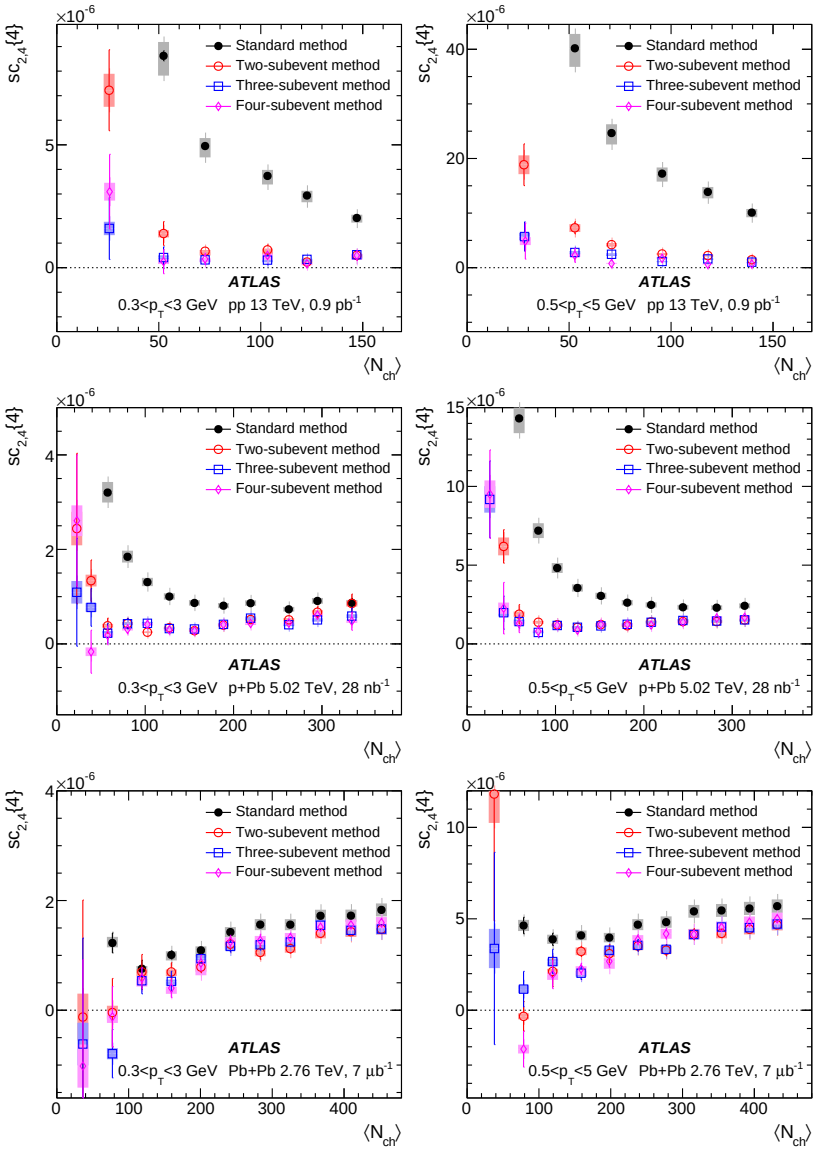

Figure 60: The symmetric cumulant $\mathrm{sc}_{2,4}\{4\}$ as a function of $\langle N_{\mathrm{ch}} \rangle$ for $0.3 < p_{\mathrm{T}} < 3$ GeV (left panels) and $0.5 < p_{\mathrm{T}} < 5$ GeV (right panels) obtained for pp collisions (top row), p+Pb collisions (middle row) and low-multiplicity Pb+Pb collisions (bottom row). In each panel, the $\mathrm{sc}_{2,4}\{4\}$ is obtained from the standard method (filled symbol), two-subevent method (open circles), three-subevent method (open squares) and four-subevent method (open diamonds). The error bars and shaded boxes represent the statistical and systematic uncertainties, respectively.

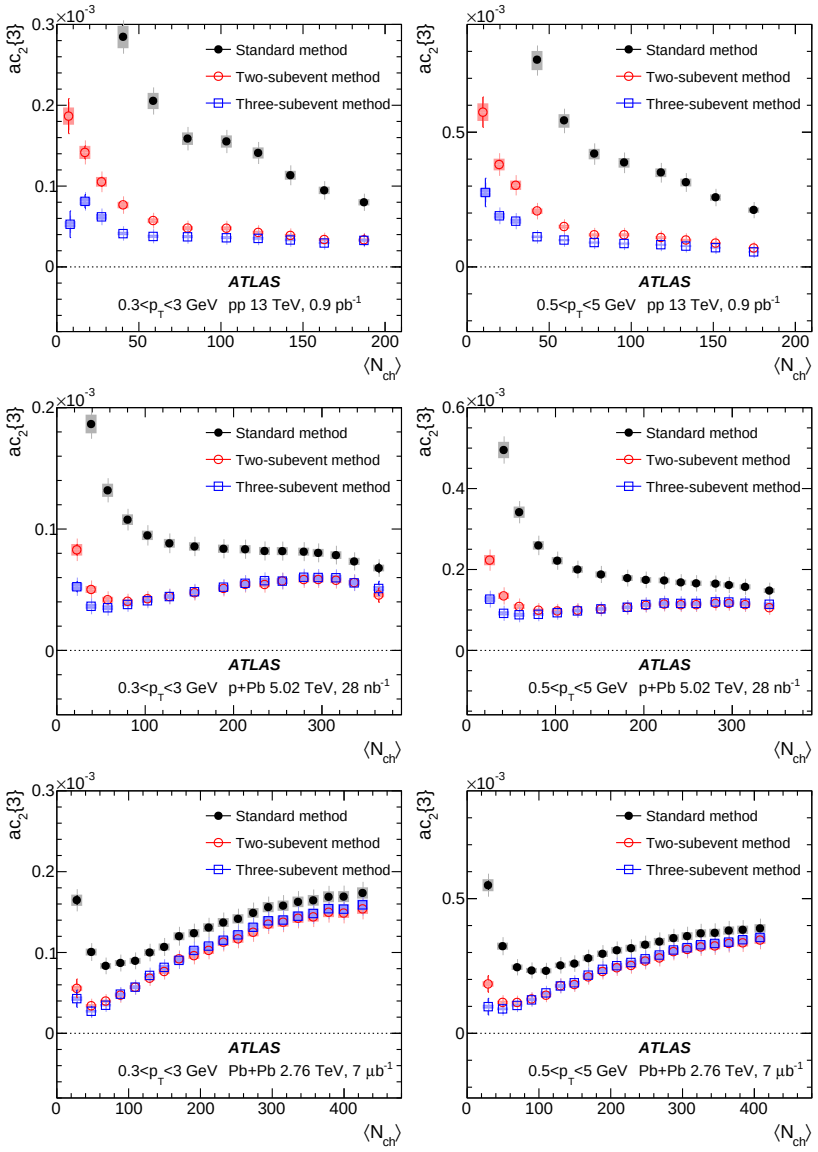

Figure 61: The asymmetric cumulant $\mathrm{ac}_2\{3\}$ as a function of $\langle N_{\mathrm{ch}} \rangle$ for $0.3 < p_{\mathrm{T}} < 3$ GeV (left panels) and $0.5 < p_{\mathrm{T}} < 5$ GeV (right panels) obtained for pp collisions (top row), p+Pb collisions (middle row) and low-multiplicity Pb+Pb collisions (bottom row). In each panel, the $\mathrm{ac}_2\{3\}$ is obtained from the standard method (filled symbol), two-subevent method (open circles), and three-subevent method (open squares). The error bars and shaded boxes represent the statistical and systematic uncertainties, respectively.

5.5 Comparison between collision systems

5.5.1 $sc_{2,3}\{4\}$, $sc_{2,4}\{4\}$ and $ac_2\{3\}$

Figure 62 shows a direct comparison of cumulants for the three collision systems.

The results for $sc_{2,3}\{4\}$, $sc_{2,4}\{4\}$ and $ac_2\{3\}$ are presented in three panels respectively. The top row is the results for $0.3 < p_T < 3$ GeV and the bottom row is for $0.5 < p_T < 5$ GeV. These results support negative correlation between v_2 and v_3 and a positive correlation between v_2 and v_4. Such correlation patterns have previously been observed in Pb+Pb systems [33, 50, 54], but are now confirmed also in the small collision systems without the influence of non-flow effects. For symmetric cumulants $sc_{2,3}\{4\}$ and $sc_{2,4}\{4\}$, we adopt a wide multiplicity bin including more events to reduce statistical uncertainty for each measured points. In the multiplicity range covered by the *pp* collisions, $\langle N_{ch} \rangle < 150$, the results for $sc_{2,3}\{4\}$ and $sc_{2,4}\{4\}$ are similar among the three systems. In the range $\langle N_{ch} \rangle > 150$, $sc_{2,3}\{4\}$ and $sc_{2,4}\{4\}$ are larger in Pb+Pb than in *p*+Pb collisions one reason is due to magnitude of flow v_n is larger in Pb+Pb. For asymmetric cumulant $ac_2\{3\}$, we have finer $\langle N_{ch} \rangle$ bin which gives more points in *pp* system than $sc_{n,m}\{4\}$. At $\langle N_{ch} \rangle < 100$, the results are similar among the three systems, but they deviate from each other at higher $\langle N_{ch} \rangle$. The *pp* data are approximately constant or decrease slightly with $\langle N_{ch} \rangle$, while the *p*+Pb and Pb+Pb data show significant increases as a function of $\langle N_{ch} \rangle$.

5.5.2 $nsc_{2,3}\{4\}$, $nsc_{2,4}\{4\}$ and $nac_2\{3\}$

Figure 63 shows the results for normalized cumulants, $nsc_{2,3}\{4\}$, $nsc_{2,4}\{4\}$ and $nac_2\{3\}$, compared among the three systems. This normalization helps to remove the variation from multiplicity dependence of v_n. Within expectation, the normalized cumulants generally show a much weaker multiplicity dependence at $\langle N_{ch} \rangle > 100$, where the statistical uncertainties are small.

In the top row are results from $0.3 < p_T < 3$ GeV. For the normalized

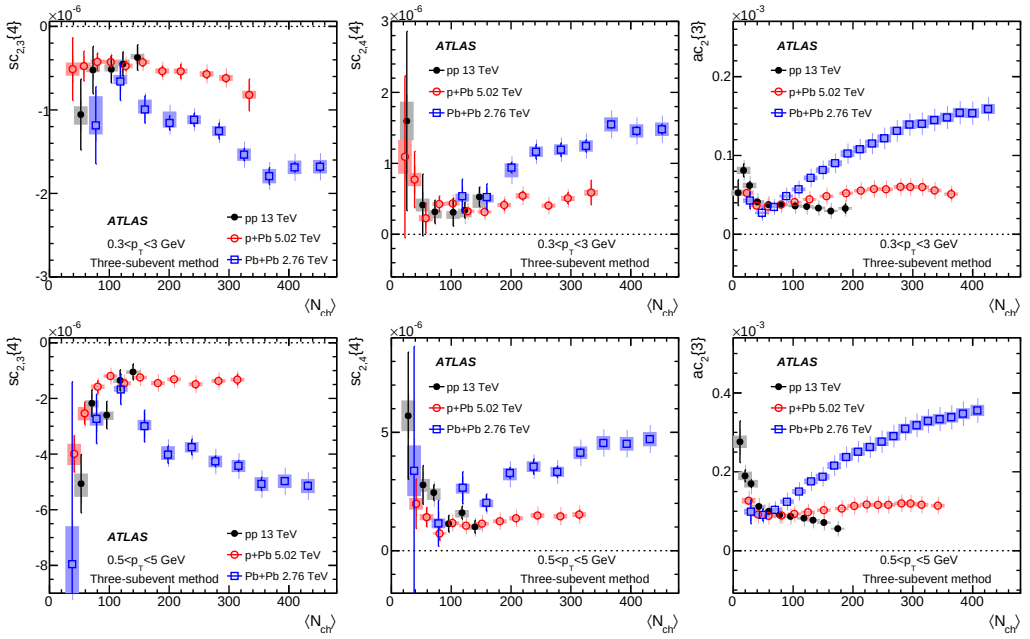

Figure 62: The $\langle N_{\rm ch}\rangle$ dependence of $\mathrm{sc}_{2,3}\{4\}$ (left panels), $\mathrm{sc}_{2,4}\{4\}$ (middle panels) and $\mathrm{ac}_2\{3\}$ (right panels) in $0.3 < p_{\rm T} < 3$ GeV (top row) and $0.5 < p_{\rm T} < 5$ GeV (bottom row) obtained for pp collisions (solid circles), p+Pb collisions (open circles) and low-multiplicity Pb+Pb collisions (open squares). The error bars and shaded boxes represent the statistical and systematic uncertainties, respectively.

symmetric cumulant $\mathrm{nsc}_{2,3}\{4\}$, values from p+Pb and Pb+Pb are consistent while the absolute magnitude in pp is almost 4 times larger. This is very different from the good consistency of $\mathrm{sc}_{2,3}\{4\}$ values shown in Fig. 62. One highly possible reason is because $\langle v_3^2\rangle$ values from the template fit method [60] may be significantly underestimated due to the presence of a large away-side peak at $\Delta\phi \sim \pi$ in the two-particle correlation function [27, 39]. We will discuss the produce to obtain $\langle v_n^2\rangle$ used in the normalization in Section 6. For $\mathrm{nsc}_{2,4}\{4\}$ and $\mathrm{nac}_2\{3\}$, the value are similar among different collision systems and is constant at large $\langle N_{\rm ch}\rangle$, although some differences at the

relative level of 20–30% are observed.

The bottom row in Figure 63 shows normalized cumulants in $0.5 < p_{\mathrm{T}} < 5$ GeV. The normalized cumulants are consistent with $0.3 < p_{\mathrm{T}} < 3$ GeV not only in the patterns but also in the magnitude of values. On the other hand, the original un-normalized cumulants in Figure 62 differ by a large factor between the two p_{T} ranges: about a factor of three for $\mathrm{sc}_{2,3}\{4\}$ and $\mathrm{sc}_{2,4}\{4\}$, and a factor of two for $\mathrm{ac}_2\{3\}$. These results suggest that the p_{T} dependence of $\mathrm{sc}_{2,3}\{4\}$, $\mathrm{sc}_{2,4}\{4\}$ and $\mathrm{ac}_2\{3\}$ largely reflects the p_{T} dependence of the v_n at the single-particle level.

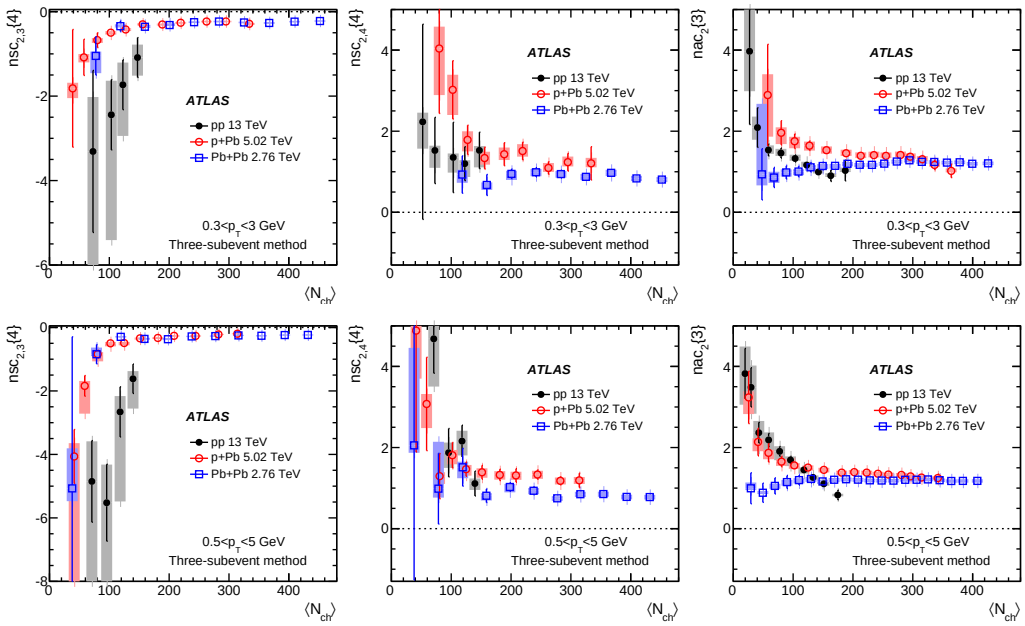

Figure 63: The $\langle N_{\mathrm{ch}} \rangle$ dependence of $\mathrm{nsc}_{2,3}\{4\}$ (left panels), $\mathrm{nsc}_{2,4}\{4\}$ (middle panels) and $\mathrm{nac}_2\{3\}$ (right panels) in $0.3 < p_{\mathrm{T}} < 3$ GeV (top row) and $0.5 < p_{\mathrm{T}} < 5$ GeV (bottom row) obtained for pp collisions (solid circles), p+Pb collisions (open circles) and low-multiplicity Pb+Pb collisions (open squares). The error bars and shaded boxes represent the statistical and systematic uncertainties, respectively.

5.6 Summary

In summary, in this chapter we present results of symmetric and asymmetric cumulants in $\sqrt{s} = 13$ TeV pp, $\sqrt{s_{\rm NN}} = 5.02$ TeV p+Pb, and low-multiplicity $\sqrt{s_{\rm NN}} = 2.76$ TeV Pb+Pb collisions. The symmetric cumulants $\mathrm{sc}_{n,m}\{4\} = \langle v_n^2 v_m^2 \rangle - \langle v_n^2 \rangle \langle v_m^2 \rangle$ probe the correlation of the flow magnitudes, while the asymmetric cumulant $\mathrm{ac}_2\{3\} = \langle v_2^2 v_4 \cos 4(\Phi_2 - \Phi_4) \rangle$ is sensitive to correlations involving both the flow magnitude v_n and flow phase Φ_n. These cumulants are calculated with the standard cumulant method, which is same with CMS and ALICE, as well as with the two-, three- and four-subevent methods to suppress non-flow effects. The final results are presented as a function of the average number of charged particles with $p_{\rm T} > 0.4$ GeV, $\langle N_{\rm ch} \rangle$.

Firstly, comparison between different methods suggest the standard method is inevitable contaminated by non-flow correlations, which is significant in pp collisions over the full $\langle N_{\rm ch} \rangle$ range, as well as over the low $\langle N_{\rm ch} \rangle$ range in p+Pb and Pb+Pb collisions. Secondly, systematic, but much smaller, differences are also observed in the low $\langle N_{\rm ch} \rangle$ region between the two-subevent method and three- or four-subevent methods, which indicate that the two-subevent method may still be affected by correlations arising from jets. Lastly, the three-subevent and four-subevent methods show consistent results within experimental uncertainties, suggesting that non-flow correlations have been sufficiently suppressed in these methods. Therefore, the three-subevent method is used to present the main results in this analysis.

The three-subevent method provides a measurement of negative $\mathrm{sc}_{2,3}\{4\}$ and positive $\mathrm{sc}_{2,4}\{4\}$ and $\mathrm{ac}_2\{3\}$ over nearly the full $\langle N_{\rm ch} \rangle$ range and in all three collision systems. These results indicate a negative correlation between v_2 and v_3 and a positive correlation between v_2 and v_4, which is similar with observation in Pb+Pb systems [33, 50, 54] where the result is attributed to the hydrodynamic flow of a strongly interacting medium. After scaling by the $\langle v_n^2 \rangle$ estimated from a two-particle analysis [59, 60], the resulting normalized cumulants $\mathrm{nsc}_{2,3}\{4\}$, $\mathrm{nsc}_{2,4}\{4\}$ and $\mathrm{nac}_2\{3\}$ show a much weaker

dependence on $\langle N_{\rm ch} \rangle$, and their values are quantitatively similar to each other among the three systems. These new results from subevent cumulant methods provides further evidence of a similar origin of long-range collective phenomenon involving many particles in small and large systems. These similarity provide an important input and constraints on theoretical model calculations.

6 Measurements of two-particle correlations in pp, p+Pb and Pb+Pb

This section details the procedure to extract the $\langle v_n^2 \rangle$ used to normalize the cumulants $\mathrm{sc}_{n,m}\{4\}$ and $\mathrm{ac}_n\{3\}$ in Section 5 in pp, p+Pb and Pb+Pb systems. The orginazation of this scetion is as follows: In Section 6.1 and Section 6.2, the construction of 2D and 1D correlation function in data analysis are discussed. In Sections 6.3 and 6.4, the template fit method is introduced which subtracts non-flow correlation before extracting $\langle v_n^2 \rangle$. In Section 6.5, the systematic uncertainties are described. And In Section 6.6 the final results are shown. The analysis is done in two different p_{T} range: $p_{\mathrm{T}} \in (0.3, 3)$ GeV and $p_{\mathrm{T}} \in (0.5, 5)$ GeV separately. This analysis is mostly contained in Ref. [57].

6.1 2D Two-particle correlations

Two-particle correlation method measures the distribution of pair yields of two particles via the relative azimuthal difference $\Delta\phi$ and relative pseudo-rapdity difference $\Delta\eta$. For a given event class, which is decided upon the number of reconstructed tracks ($N_{\mathrm{ch}}^{\mathrm{rec}}$), the correlation function is defined as:

$$C(\Delta\phi, \Delta\eta) = \frac{S(\Delta\phi, \Delta\eta)}{B(\Delta\phi, \Delta\eta)} \tag{101}$$

where S and B represent pair distributions constructed from the same event and from "mixed events", respectively.

The same-event distribution (signal distribution) is constructed using all particle pairs that can be formed in each event from tracks, averaged over many events

$$S(\Delta\eta, \Delta\phi) = \left\langle \frac{d^2 N_{\mathrm{same}}^{\mathrm{pairs}}(\Delta\phi, \Delta\eta)}{d\Delta\eta d\Delta\phi} \right\rangle \tag{102}$$

The S distribution contains both the physical correlations between particle pairs and correlations arising from detector acceptance effects.

The mixed-event distribution is similarly constructed by choosing the two particles in the pair from two different events, also averaged over many event pairs

$$B(\Delta\eta, \Delta\phi) = \left\langle \frac{d^2 N^{\text{pairs}}_{\text{mixed}}(\Delta\phi, \Delta\eta)}{d\Delta\eta d\Delta\phi} \right\rangle \tag{103}$$

The B distribution does not contain physical correlations, but has detector acceptance effects similar to those in S. Upon dividing by the B, detector acceptance effects largely cancel from S, and the resulting correlation function contains physical correlations only. The pair of events used in the mixing are have similar $N^{\text{rec}}_{\text{ch}}$ ($|\Delta N^{\text{rec}}_{\text{ch}}| < 10$) and similar vertex position z_{vtx} ($|\Delta z_{\text{vtx}}| < 10$ mm), so that acceptance effects in S are properly reflected in, and compensated by, corresponding variations in B. To correct S and B for the individual ϕ-averaged inefficiencies of particles a and b, the pairs are weighted by the inverse product of their tracking efficiencies $1/(\epsilon_a \epsilon_b)$. Typically, the two-particle correlations are used only to study the shape of the correlations in $\Delta\phi$, and are conveniently normalized. In this paper, the normalization of $C(\Delta\eta, \Delta\phi)$ is chosen such that the $\Delta\phi$-averaged value of $C(\Delta\eta, \Delta\phi)$ is unity for $|\Delta\eta| > 2$.

Figure 64 shows one example of mixed-event distribution, signal distribution and correlation function in high multiplicity p+Pb events at 5.02 TeV. Tracks are taken from ATLAS Inner Detector (ID) which has a pseudorapidity coverage $\eta \in (-2.5, 2.5)$ and a full azimuthal coverage. Thus for a pair of particles, the relative pseuodurapdity range is $\eta \in (-5, 5)$.The mixed-event distribution have a triangular shape in $\Delta\eta$ direction, which is is understood as the finite pair acceptance effect such that the phase space to sample a pair at larger $\Delta\eta$ drops linearly toward the edge of the detector acceptance. Apart from the the shape, the are also small modulation in both $\Delta\eta$ and $\Delta\phi$ due to non-uniform acceptance of detector, which are small effect and invisible. A similar triangular shape is also seen in signal distribution, along with some visible $\Delta\eta$ and $\Delta\phi$ modulation reflecting the physics correlations. After dividing by mixed-event distribution both triangular shape and detector effect are cancelled in the correlation function. The the magnitude of

correlation function is ~ 1 on average rather than true pair yields, due to the normalization of $B(\Delta\eta, \Delta\phi)$. However, the overall normalization is not so important for the extraction of v_n as they are defined as modulations relative to the average in Equation (28).

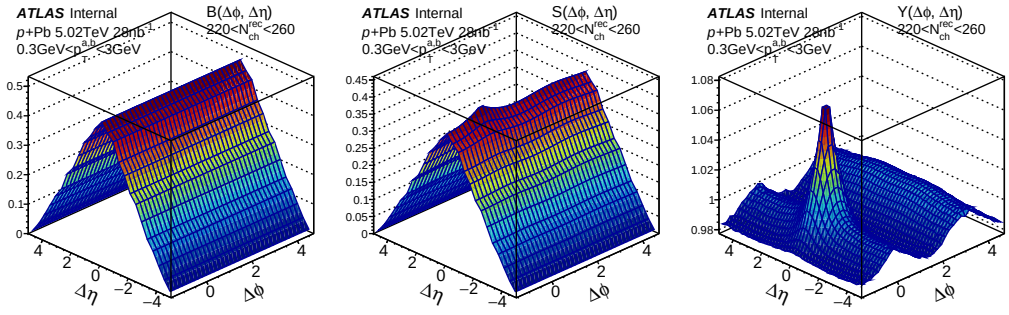

Figure 64: Signal distribution, mixed-event distribution and correlation function from p+Pb collision, with trigger and associated particles selected from $p_{\mathrm{T}} \in (0.3, 3)$GeV. These correlation functions are plotted over the range $-\pi/2 < \Delta\phi < 3\pi/2$; the periodicity of the measurement requires $C(\Delta\eta, 3\pi/2) = C(\Delta\eta, -\pi/2)$.

6.2 1D Two-particle correlations

One-dimensional correlation functions $C(\Delta\phi)$ are obtained by integrating the numerator and denominator of Equation (101) over long-range region $(2 < |\Delta\eta| < 5)$ prior to taking the ratio

$$C(\Delta\phi) = \frac{\int_2^5 d|\Delta\eta| S(|\Delta\eta|, \Delta\phi)}{\int_2^5 d|\Delta\eta| B(|\Delta\eta|, \Delta\phi)} \tag{104}$$

The $|\Delta\eta|$ range is choose to avoid non-flow peak around $(\Delta\eta \approx 0, \Delta\phi \approx 0)$. From the one-dimensional correlation function, *per-trigger-particle yields* (PTY) is calculated

$$Y(\Delta\phi) = \frac{\int_{-\pi/2}^{3\pi/2} B(\Delta\pi) d\Delta\pi}{N^a \int_{-\pi/2}^{3\pi/2} d\Delta\pi} C(\Delta\phi) \tag{105}$$

where N^a denotes the total number of trigger particles, with each track is corrected to account for the tracking efficiency. The $Y(\Delta\phi)$ distribution is identical in shape to $C(\Delta\phi)$, but has a physically relevant normalization: it represents the average number of particles correlated with each trigger particle in a given $\Delta\phi$ interval. This allows operations, such as subtraction of the $Y(\Delta\phi)$ distribution in one event-activity class from the $Y(\Delta\phi)$ distribution in another, which will be discussed in Section 6.3.

Figure 65 shows the per-trigger yields at different $N_{\rm ch}^{\rm rec}$ range in p+Pb. In these "peripheral" (low multiplicity) events, the modulation in $\Delta\phi$ is mainly dominated by away-side dijet correlations. From "peripheral" to "central" (high multiplicity) events, a clear near-side "ridge" becomes visible. Figure 66 is the similar plot for pp at 13TeV and near-size ridge emerges in more central events.

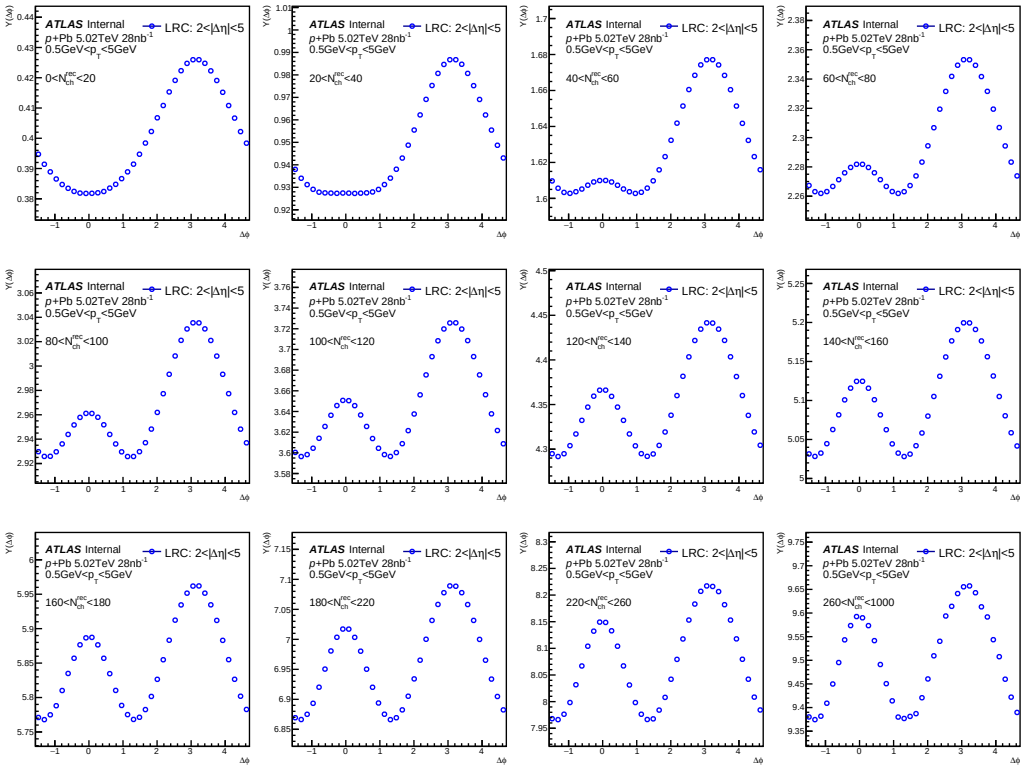

Figure 65: The landscape of 1D correlation function in $Y(\Delta\phi)$, integrated over $2 < |\Delta\eta| < 5$ in 5.02TeV p+Pb with $0.5 < p_{\mathrm{T}}^{a,b} < 5$ GeV. Each panel shows the distributions for one multiplicity interval.

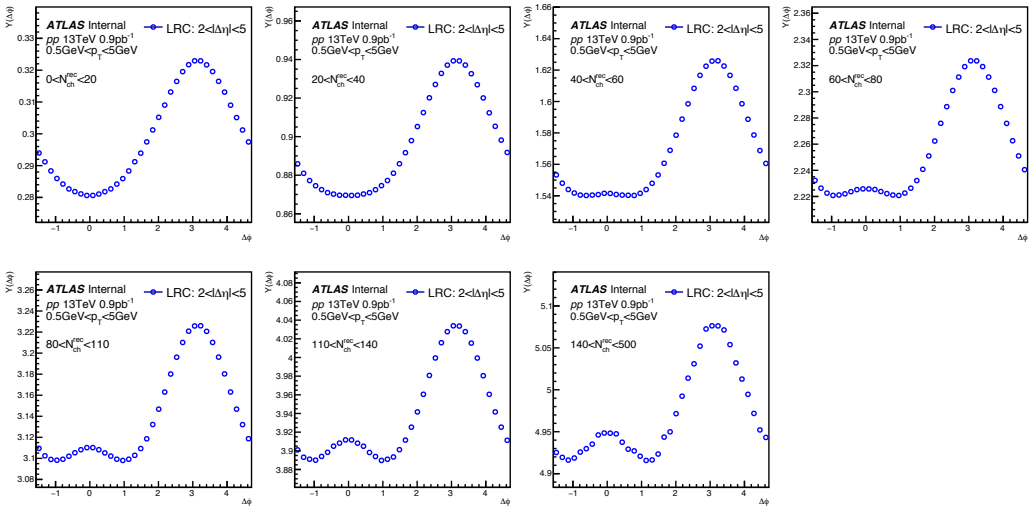

Figure 66: Similar plot with Figure 65 but for *pp* 13TeV.

6.3 Template fitting method

In the small system, away-side dijet correlations dominate the $\Delta\phi$ structure of per-trigger yield, as seen in Figures 65 and 66. Direct Fourier decomposition method

$$Y(\Delta\phi) = A(1 + 2\sum_{n=1}^{\infty} v_{n,n}\cos(n\Delta\phi)) \tag{106}$$

gives a measured v_n^2 biased by the dijet correlation, especially for odd harmonics. For this purpose, a template fit method [59, 60] is proposed, in which the dijet contribution was estimated and removed, thus obtaining the genuine long-range correlation and its Fourier coefficient. This method is developed by ATLAS for several publications already [59, 60]. Here we just give a brief introuction.

In this method, The measured per-trigger yield distribution in a given $N_{\mathrm{ch}}^{\mathrm{rec}}$ interval is assumed to result from a superposition of a scaled "peripheral" distribution $Y(\Delta\phi)^{\mathrm{peri}}$, obtained for low multiplicity events $N_{\mathrm{ch}}^{\mathrm{rec}} < 20$, and a constant pedestal modulated by $\cos(n\Delta\phi)$ for $n \geq 2$ [59, 60]. Therefore, we construct the template fit function

$$Y(\Delta\phi)^{\mathrm{tmp}} = F\,Y(\Delta\phi)^{\mathrm{peri}} + Y_{\mathrm{ridge}}(\Delta\phi) \tag{107}$$

where

$$Y_{\mathrm{ridge}}(\Delta\phi) = G^{\mathrm{tmp}}\left(1 + 2\sum_{n=2}^{\infty} v_n\{2,\mathrm{tmp}\}^2\cos n\Delta\phi\right) \tag{108}$$

By fitting the template function $Y(\Delta\phi)^{\mathrm{tmp}}$ to the actual measured per-trigger yield $Y(\Delta\phi)$, the scale factor F and pedestal G^{tmp} are fixed, and $v_n\{2,\mathrm{tmp}\}$ are calculated from a Fourier transform.

The left panel of Figure 67 shows such a template fit, in the 13 TeV pp data, that only includes $v_2\{2,\mathrm{tmp}\}^2$. The right panel shows the difference between the $Y(\Delta\phi)$ and the $Y(\Delta\phi)^{\mathrm{tmp}}$ distributions demonstrating the presence of small, but significant residual $v_3\{2,\mathrm{tmp}\}^2$ and $v_4\{2,\mathrm{tmp}\}^2$ components. While it is possible that $\cos 3\Delta\phi$ and $\cos 4\Delta\phi$ contributions could arise in the template fitting method due to small multiplicity-dependent changes in the shape of the dijet component of the correlation function, such effects

would not produce the excess at $\Delta\phi \sim 0$ observed in the right-hand panel in Figure 67. That excess and the fact that its magnitude is compatible with the remainder of the distribution indicates that there is real $\cos 3\Delta\phi$ and $\cos 4\Delta\phi$ modulation in the two-particle correlation functions. Thus this analysis measures $v_n\{2, \mathrm{tmp}\}^2$ with $n = 2 - 4$.

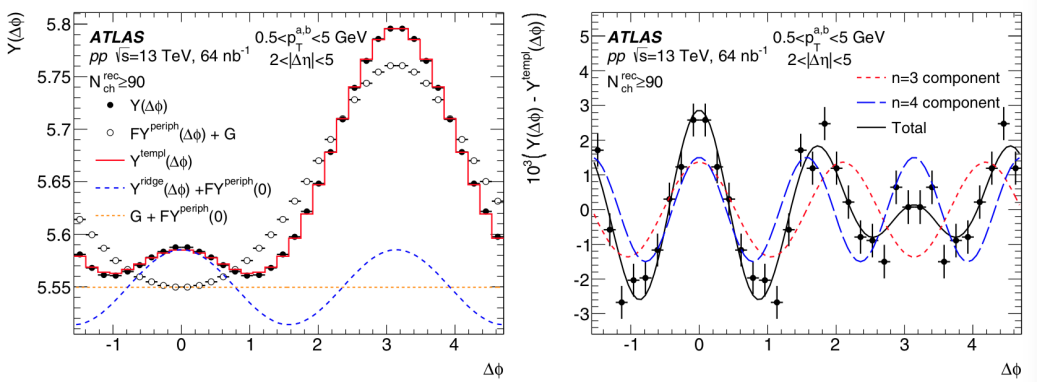

Figure 67: Left panel: template fit to the $Y(\Delta\phi)$ in 13 TeV pp collisions. This plot corresponds to the $N_{\mathrm{ch}}^{\mathrm{rec}} > 90$ multiplicity range. The template fitting includes only the second-order harmonic, $v_2\{2, \mathrm{tmp}\}^2$. The solid points indicate the measured $Y(\Delta\phi)$, the open points and curves show different components of the template (see legend) that are shifted along the y axis by G or by $FY(0)^{\mathrm{peri}}$, where necessary, for presentation. Right panel: The difference between the $Y(\Delta\phi)$ and the template fit, showing the presence of $v_3\{2, \mathrm{tmp}\}^2$ and $v_4\{2, \mathrm{tmp}\}^2$ components. The vertical error bars indicate statistical uncertainties.

However, template fit method has a limitation that $v_n\{\mathrm{tmp}\}^2$ from the fit does not equal to the true flow v_n^2 if v_n has multiplicity dependence. One notice both $Y(\Delta\phi)$ and $Y(\Delta\phi)^{\mathrm{peri}}$ contain a dijet component and flow

component:

$$Y(\Delta\phi) = Y(\Delta\phi)^{\text{cent}}_{\text{dijet}} + G^{\text{cent}}\left(1 + 2\sum_{n=2}^{\infty} v_n^2 \cos n\Delta\phi\right). \tag{109}$$

$$Y(\Delta\phi)^{\text{peri}} = Y(\Delta\phi)^{\text{peri}}_{\text{dijet}} + G^{\text{peri}}\left(1 + 2\sum_{n=2}^{\infty} v_n\{\text{peri}\}^2 \cos n\Delta\phi\right). \tag{110}$$

With the assumption that the shape of the dijet component is invariant at different of $N_{\text{ch}}^{\text{rec}}$, and the magnitudes of the dijet components are related by the scale factor F: $Y_{\text{dijet}}(\Delta\phi) = FY^{\text{peri}}_{\text{dijet}}(\Delta\phi)$, Equation (107) can be written as:

$$Y(\Delta\phi) = Y(\Delta\phi)^{\text{cent}}_{\text{dijet}} + (G^{\text{tmp}} + FG^{\text{peri}}) + 2\sum_{n=2}^{\infty}\left(G^{\text{tmp}} v_n\{\text{tmp}\}^2 + FG^{\text{peri}} v_n\{\text{peri}\}^2\right)\cos n\Delta\phi. \tag{111}$$

Comparing with Equation (109) and Equation (110), one obtains $G^{\text{cent}} = G^{\text{tmp}} + FG^{\text{peri}}$ and the following relation:

$$v_n\{2,\text{tmp}\}^2 = v_n\{2\}^2 + \frac{F\,G^{\text{peri}}}{G^{\text{tmp}}}\left(v_n\{2\}^2 - v_n\{2,\text{peri}\}^2\right) \tag{112}$$

or equivalently

$$v_n\{2\}^2 = v_n\{2,\text{tmp}\}^2 - \frac{F\,G^{\text{peri}}}{G^{\text{tmp}} + FG^{\text{peri}}}\left(v_n\{2,\text{tmp}\}^2 - v_n\{2,\text{peri}\}^2\right), \tag{113}$$

The above equation indicates that one can only measure the exact flow harmonics when v_n is constant at different multiplicity, which is the case for v_2 in pp but not for other systems. In most cases, collective behavior developing at low multiplicity region is less prominent compared to those at the high multiplicity region, i.e. v_n increase with multiplicity. Therefore results from the template fit method overestimated the true flow. Another limitation is that $v_n\{2,\text{tmp}\}$ has sensitivity to choice of multiplicity bin of these peripheral events, which determines the contribution of overestimation in Equation (112).

6.4 One-step correction after template fit

In principle, we can use Equation (113) to get the true flow value. Since $v_n\{2,\text{tmp}\}$ and F are determined already from template fit, there are only

two unknown G^{peri} and $v_n\{2, \text{peri}\}$ and we use a data-driven way to get a raw estimation.

We can assume $Y(\Delta\phi)^{\text{peri}}$ is mainly modulated by (di)jets correlations on top of uncorrelated pairs (G^{peri}) and flow contribution is negligible based on observation. Using zero-yield-at-minimum (ZYAM) method, which assumes pair yield from (di)jets has its minimum value equal to zero, one can use value of the lowest point on $Y(\Delta\phi)^{\text{peri}}$ to represent G^{peri}. A second-order polynomial fit to the 1D $Y(\Delta\phi)^{\text{peri}}$ distribution is used to find the location of the minimum point, $\Delta\phi_{\text{ZYAM}}$, as show on Figure 68. From this the value G^{peri} is determined as the yield $Y(\Delta\phi_{\text{ZYAM}})^{\text{peri}}$.

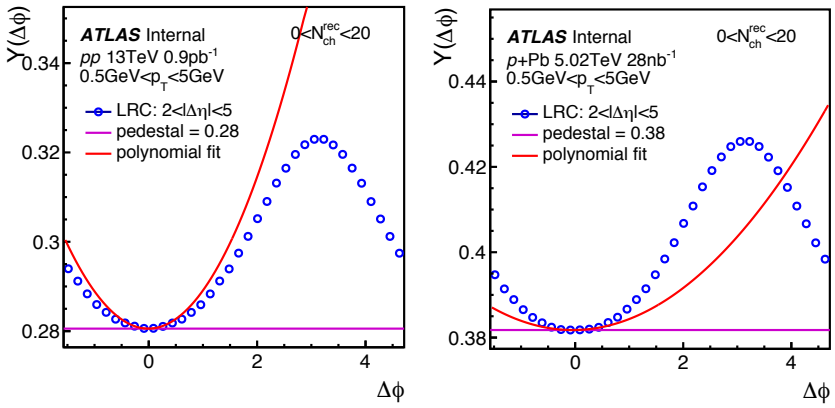

Figure 68: ZYAM procedue to get G^{peri} using a second order polynomila fit. Left: p+Pb at 5.02TeV, Right: pp at 13TeV.

The $v_n\{2, \text{peri}\}$ is not measurable directly in the peripheral interval ($N_{\text{ch}}^{\text{rec}} < 20$), so we can use $v_n\{2, \text{tmp}\}$ of the second $N_{\text{ch}}^{\text{rec}}$ interval ($20 \leq N_{\text{ch}}^{\text{rec}} < 40$) as an estimate. So the the correction is applied starting from the third-lowest $N_{\text{ch}}^{\text{rec}}$ interval ($40 \leq N_{\text{ch}}^{\text{rec}} < 60$) in this analysis. Since the non-flow contribution primarily affects the odd harmonics, the $v_3\{2, \text{tmp}\}^2$ may become negative in the first few $N_{\text{ch}}^{\text{rec}}$ intervals in pp collisions. In such cases, the correction starts from the second $N_{\text{ch}}^{\text{rec}}$ interval with positive $v_3\{2, \text{tmp}\}^2$ ($60 \leq N_{\text{ch}}^{\text{rec}} < 80$) by using $v_3\{2, \text{tmp}\}$ from the previous $N_{\text{ch}}^{\text{rec}}$ interval ($40 \leq N_{\text{ch}}^{\text{rec}} < 60$).

Figure 69 compares the corrected $v_n\{2\}^2$ and $v_n\{2,\mathrm{tmp}\}^2$ for three peripheral $N_{\mathrm{ch}}^{\mathrm{rec}}$ intervals: $N_{\mathrm{ch}}^{\mathrm{rec}} < 20$, $N_{\mathrm{ch}}^{\mathrm{rec}} < 10$ and $10 \le N_{\mathrm{ch}}^{\mathrm{rec}} < 20$. The corrected values are smaller than original template fit values and is less sensitive to choice of peripheral bins.

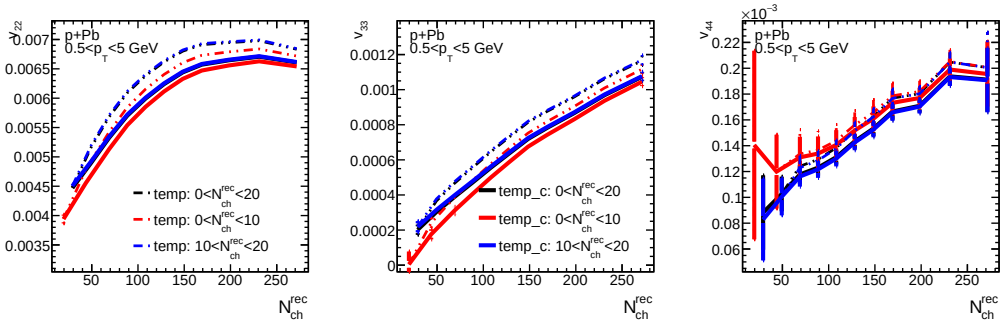

Figure 69: The values of $v_n\{2,\mathrm{tmp}\}^2$ from template fit and $v_n\{2\}^2$ with correction applied obtained in p+Pb collisions for n = 2 (left panel), n = 3 (middle panel) and n = 4 (right panel). In each panel, the values are calculated for three peripheral $N_{\mathrm{ch}}^{\mathrm{rec}}$ intervals: $N_{\mathrm{ch}}^{\mathrm{rec}} < 20$, $N_{\mathrm{ch}}^{\mathrm{rec}} < 10$ and $10 \le N_{\mathrm{ch}}^{\mathrm{rec}} < 20$. Only statistical uncertainties are shown.

6.5 Systematic error

The template fit method follows the prescription of the previous ATLAS publications. So the systematic uncertainties is very similar to Ref. [60]. Here we will discuss the several main sources : pileup, tracking efficiency and choice of the peripheral bin used in the template fits.

Pileup. Pileup events, when included in the two-particle correlation measurement, dilute the v_n^2 signal since they produce pairs where the trigger and associated particle are from different collisions and thus have no physical correlations. In the p+Pb data, nearly all of the events containing pileup are removed by the procedure in Ref. [27]. The influence of the residual pileup is evaluated by relaxing the pileup rejection criteria and then calculating the change to v_n^2 values. The differences are taken as an estimate of the uncer-

tainty for the $v_n\{2\}^2$, and are found to be negligible in low event activity classes, and increase to 4% for events with $N_{\rm ch}^{\rm rec}$ ~300.

In *pp*, default analysis use events with only 1 reconstructed vertex since events with multiple vertices have a high possibility to have pileup events. However there is still a chance of merged vertices, and events with multiple unresolved vertices affect the results by increasing the combinatoric pedestal in $Y(\Delta\phi)$. The fraction of events with merged vertices is estimated and taken as the relative uncertainty associated with pileup in the *pp* analysis. The merged-vertex rate in the 13 TeV *pp* data is0–3% over the 0-150 $N_{\rm ch}^{\rm rec}$ range.

In Pb+Pb, no pileup effect is checked since rate of pileup events is negligible.

Tracking efficiency. The systematic uncertainties in the efficiency $\epsilon(p_{\rm T},\eta)$ is studied in the same way as in Section 4. In the *pp* analysis, this uncertainty is estimated to be 0.5% for v_2^2 and 2.5% for v_3^2 and v_4^2. Tracks in *p*+Pb and peripheral Pb+Pb are reconstructed using the same algorithm, the corresponding uncertainties are the same for both cases, which are 0.8%, 1.6%, and 2.4% for v_2^2, v_3^2 and v_4^2, respectively.

Choice of the peripheral bin . The important feature of the template fit analysis is the assumption that the dijet component $Y(\Delta\phi)_{\rm dijet}$ is independent of $\langle N_{\rm ch}\rangle$. In Ref. [60], the uncertainty associated with this assumption is studied by changing the default peripheral interval from $N_{\rm ch}^{\rm rec} < 20$ to $N_{\rm ch}^{\rm rec} < 10$ and $10 \leq N_{\rm ch}^{\rm rec} < 20$. It was found that the $v_n\{\rm tmp\}$ values are relatively insensitive to the choice of the peripheral interval for $n = 2$ and $n = 4$, but the sensitivity is much larger for $n = 3$. This finding is reproduced in Fig. 70 for *pp* collisions, which shows that the $v_3\{\rm tmp\}^2$ obtained via Equation (107) differs substantially for the different $N_{\rm ch}^{\rm rec}$ ranges. The big difference in $v_3\{\rm tmp\}^2$ may due to the known fact that template fitting have a bias when v_n^2 has a obvious $\langle N_{\rm ch}\rangle$ dependence, as shown in Equation (113). This bias is only significant for $n = 3$ in *pp* but should be there for all harmonics in *p*+Pb and Pb+Pb, where flow of the first few orders $n = 2 - 4$ are

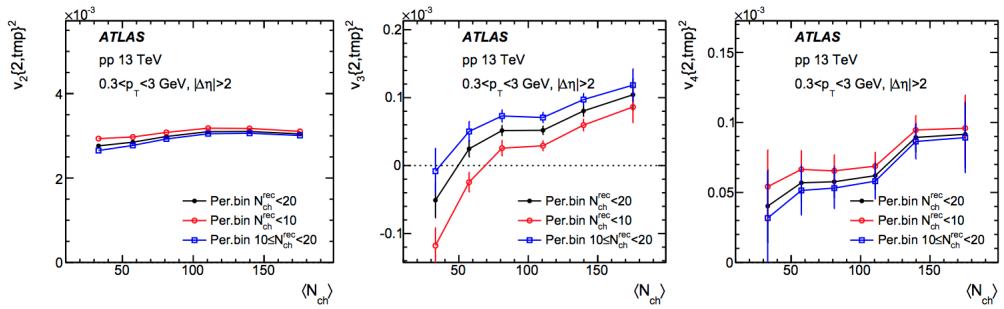

Figure 70: The values of $v_n\{2,\mathrm{tmp}\}^2$ obtained following the template fit procedure Equation (107) [60] in pp collisions for $n = 2$ (left panel), $n = 3$ (middle panel) and $n = 4$ (right panel). In each panel, the values are calculated for three peripheral $N_{\mathrm{ch}}^{\mathrm{rec}}$ intervals: $N_{\mathrm{ch}}^{\mathrm{rec}} < 20$, $N_{\mathrm{ch}}^{\mathrm{rec}} < 10$ and $10 \leq N_{\mathrm{ch}}^{\mathrm{rec}} < 20$. Only statistical uncertainties are shown.

found to increase monotonously with multiplicity. For a more precise result, the bias term need to be corrected.

6.6 Results

In addition to the template fit with and without the above mentioned correction procedure, ATLAS and CMS Collaborations also calculated directly the $v_n\{2\}$ values via a Fourier transform of the $Y(\Delta\phi)$ distribution without dijet subtraction [55, 60]. The differences between the direct Fourier transform and template fit reflect mainly the away-side jet contribution subtracted by the template fit procedure, and therefore give a sense of the magnitude of unknown systematics associated with the template fit procedure. If these differences are too large, the $v_n\{2,\mathrm{tmp}\}$ values may be sensitive to the systematic effects associated with the assumption that the shape of $Y(\Delta\phi)_{\mathrm{jet}}$ is independent of $N_{\mathrm{ch}}^{\mathrm{rec}}$.

Figure 71 compares the $v_n\{2\}$ in $0.3 < p_{\mathrm{T}} < 3$ GeV obtained from $Y(\Delta\phi)$ using three methods: a direct Fourier transform (solid circles), a template

fit (open circles) and a template fit corrected for the bias (open squares), as described above. The systematic uncertainties for the template fit results are nearly the same as those from Ref. [60]. Figure 71 shows that the changes introduced by the correction procedure described above are small in all cases and for all harmonics. The values of the even-order harmonics, v_2 and v_4, are also quite similar to those obtained from the direct Fourier transformation, reflecting the fact that the dijet correlations have very little influence on the even-order harmonics. On the other hand, significant differences are observed between the direct Fourier transform and template fit for v_3, especially in the pp collisions, due to the influence of $Y(\Delta\phi)_{\text{jet}}$, a trend observed and discussed previously in Refs. [39, 60]. The template fit procedure is able to subtract the dijet correlations and change the sign of v_3, but also introduces a large uncertainty associated with the procedure. As discussed in Section 5, the behavior of the symmetric cumulants $\text{sc}_{2,3}\{4\}$ in Figure 62 and normalized cumulants $\text{nsc}_{2,3}\{4\}$ in Figure 63 in pp collisions, suggest that the v_3 values from the template fit procedure are significantly underestimated due to the presence of a large residual non-flow bias. In contrast, the differences of v_3 between the direct Fourier transform and the template fit are much smaller in the p+Pb and the Pb+Pb collisions, except in the very low $\langle N_{\text{ch}} \rangle$ region. Therefore, the v_3 values in p+Pb and Pb+Pb systems extracted from the template fit procedure are expected to be less affected by the dijets.

Figure 72 shows the $v_n\{2\}$ for $0.5 < p_{\text{T}} < 5$ GeV in three collision systems.

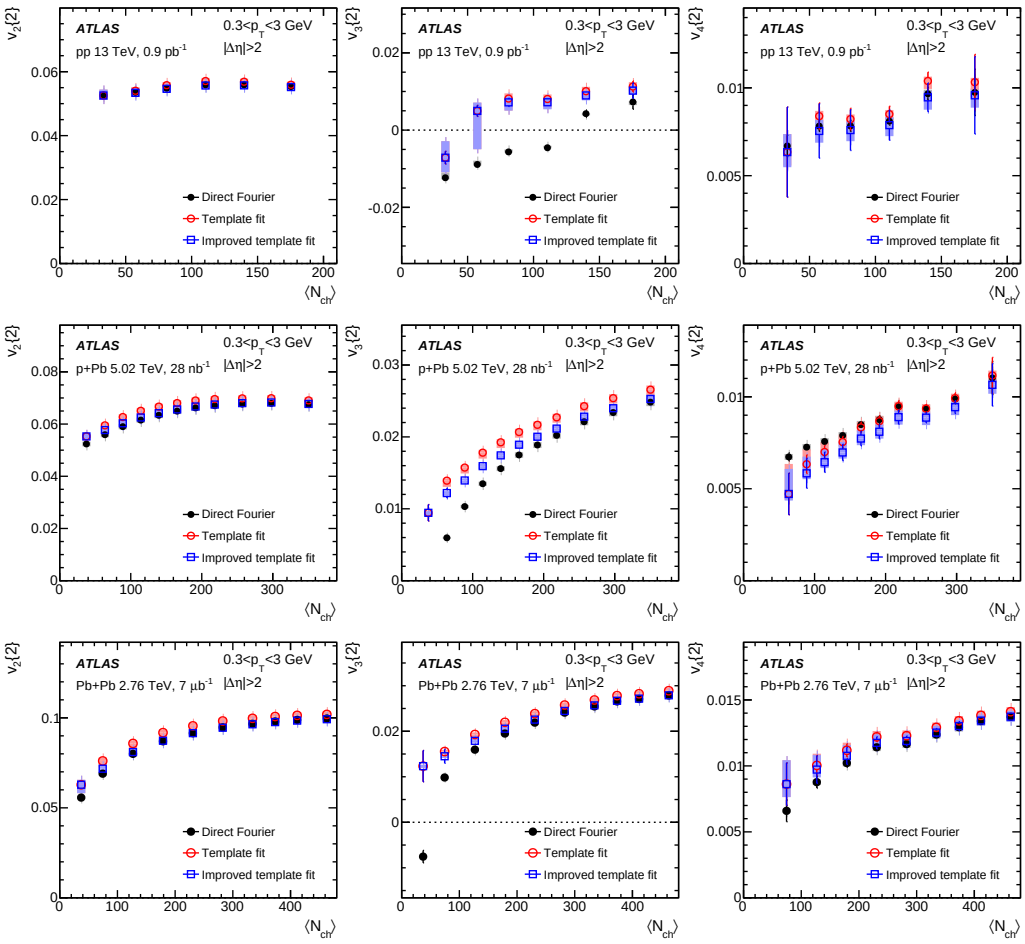

Figure 71: The v_2 (left column), v_3 (middle column) and v_4 (right column) obtained from two-particle correlations in $0.3 < p_{\mathrm{T}} < 3$ GeV in pp (top row), p+Pb (middle row) and Pb+Pb (bottom row) collisions. In each panel, they are compared between three methods: direct Fourier transformation (solid circles), template fit (open circles) and the improved template fit (open squares). The error bars and shaded boxes represent the statistical and systematic uncertainties, respectively.

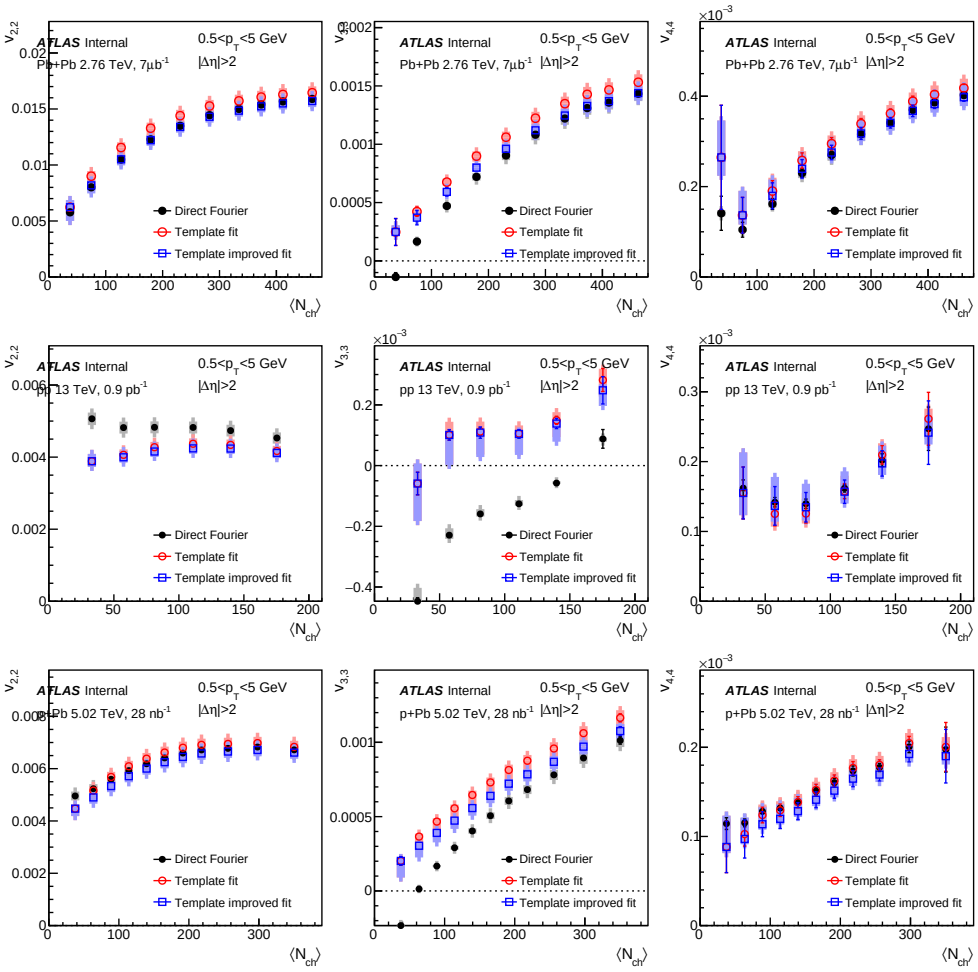

Figure 72: Similar plot with Figure 71 but for $0.5 < p_{\mathrm{T}} < 5$ GeV.

7 Conclusions

In this thesis work, comprehensive studies of flow decorrelation in longitudinal direction in 2.76 TeV and 5.02 TeV Pb+Pb collisions were presented. The factorization of two-particle azimuthal correlations into single-particle flow harmonics $\boldsymbol{V}_n$ is found to be broken due to flow decorrelation, and the amount of factorization breakdown increases approximately linearly as a function of the η separation between the two particles. Centrality depenence, p_{T} dependence and energy dependence of this decorrelation effect is studied. The results presented in this thesis work provide new insights into the fluctuations and correlations of harmonic flow in the longitudinal direction, which can be used to improve full three-dimensional viscous hydrodynamic models.

Correlations of two flow harmonics v_n and v_m via three- and four-particle cumulants are measured in 13 TeV pp, 5.02 TeV p+Pb, and 2.76 TeV peripheral Pb+Pb collisions. The large non-flow background from dijet production present in the standard cumulant method is suppressed using a method of subevent cumulants involving two, three and four subevents separated in pseudorapidity. The results show a negative correlation between v_2 and v_3 and a positive correlation between v_2 and v_4 for all collision systems and over the full multiplicity range. The relative correlation strength, obtained by normalisation of the cumulants with the $\langle v_n^2 \rangle$ from a two-particle correlation analysis, is similar in the three collision systems and depends weakly on the event multiplicity and transverse momentum. These results based on the subevent methods provide strong evidence of a similar long-range multi-particle collectivity in pp, p+Pb and peripheral Pb+Pb collisions.

While the two analyses presented here are independent measurements relying on different experimental techniques and in different systems, together they can help to provide measurements toward a unified picture of the collective phenomena from pp, p+Pb and Pb+Pb.

References

[1] Edward V. Shuryak. "Quantum Chromodynamics and the Theory of Superdense Matter". In: *Phys. Rept.* 61 (1980), pp. 71–158. DOI: 10.1016/0370-1573(80)90105-2.

[2] Y. Aoki et al. "The QCD transition temperature: results with physical masses in the continuum limit II." In: *JHEP* 06 (2009), p. 088. DOI: 10.1088/1126-6708/2009/06/088. arXiv: 0903.4155 [hep-lat].

[3] A. Bazavov et al. "The chiral and deconfinement aspects of the QCD transition". In: *Phys. Rev.* D85 (2012), p. 054503. DOI: 10.1103/PhysRevD.85.054503. arXiv: 1111.1710 [hep-lat].

[4] Szabolcs Borsanyi et al. "Transition temperature and the equation of state from lattice QCD, Wuppertal-Budapest results". In: *J. Phys. Conf. Ser.* 316 (2011), p. 012020. DOI: 10.1088/1742-6596/316/1/012020. arXiv: 1109.5032 [hep-lat].

[5] A. Bazavov et al. "Equation of state and QCD transition at finite temperature". In: *Phys. Rev.* D80 (2009), p. 014504. DOI: 10.1103/PhysRevD.80.014504. arXiv: 0903.4379 [hep-lat].

[6] Z. Fodor and S. D. Katz. "Critical point of QCD at finite T and mu, lattice results for physical quark masses". In: *JHEP* 04 (2004), p. 050. DOI: 10.1088/1126-6708/2004/04/050. arXiv: hep-lat/0402006 [hep-lat].

[7] J. D. Bjorken. "Highly Relativistic Nucleus-Nucleus Collisions: The Central Rapidity Region". In: *Phys. Rev.* D27 (1983), pp. 140–151. DOI: 10.1103/PhysRevD.27.140.

[8] Michael L. Miller et al. "Glauber modeling in high energy nuclear collisions". In: *Ann. Rev. Nucl. Part. Sci.* 57 (2007), pp. 205–243. DOI: 10.1146/annurev.nucl.57.090506.123020. arXiv: nucl-ex/0701025 [nucl-ex].

[9] Georges Aad et al. "Measurement of the centrality dependence of the charged particle pseudorapidity distribution in lead-lead collisions at $\sqrt{s_{NN}}$ = 2.76 TeV with the ATLAS detector". In: *Phys. Lett.* B710 (2012), pp. 363–382. DOI: 10.1016/j.physletb.2012.02.045. arXiv: 1108.6027 [hep-ex].

[10] Betty Abelev et al. "Centrality determination of Pb-Pb collisions at $\sqrt{s_{NN}} = 2.76$ TeV with ALICE". In: *Phys. Rev.* C88.4 (2013), p. 044909. DOI: 10.1103/PhysRevC.88.044909. arXiv: 1301.4361 [nucl-ex].

[11] S. A. Bass and A. Dumitru. "Dynamics of hot bulk QCD matter: From the quark gluon plasma to hadronic freezeout". In: *Phys. Rev.* C61 (2000), p. 064909. DOI: 10.1103/PhysRevC.61.064909. arXiv: nucl-th/0001033 [nucl-th].

[12] Serguei Chatrchyan et al. "Observation of sequential Upsilon suppression in PbPb collisions". In: *Phys. Rev. Lett.* 109 (2012). [Erratum: Phys. Rev. Lett.120,no.19,199903(2018)], p. 222301. DOI: 10.1103/PhysRevLett.109.222301, 10.1103/PhysRevLett.120.199903. arXiv: 1208.2826 [nucl-ex].

[13] Georges Aad et al. "Observation of a Centrality-Dependent Dijet Asymmetry in Lead-Lead Collisions at $\sqrt{s_{NN}}$ = 2.77 TeV with the ATLAS Detector at the LHC". In: *Phys. Rev. Lett.* 105 (2010), p. 252303. DOI: 10.1103/PhysRevLett.105.252303. arXiv: 1011.6182 [hep-ex].

[14] G. Agakishiev et al. "Strangeness Enhancement in Cu+Cu and Au+Au Collisions at $\sqrt{s_{NN}}$ = 200 GeV". In: *Phys. Rev. Lett.* 108 (2012), p. 072301. DOI: 10.1103/PhysRevLett.108.072301. arXiv: 1107.2955 [nucl-ex].

[15] Jean-Yves Ollitrault. "Anisotropy as a signature of transverse collective flow". In: *Phys. Rev.* D46 (1992), pp. 229–245. DOI: 10.1103/PhysRevD.46.229.

[16] Derek Teaney and Li Yan. "Triangularity and Dipole Asymmetry in Heavy Ion Collisions". In: *Phys. Rev.* C83 (2011), p. 064904. DOI: 10.1103/PhysRevC.83.064904. arXiv: 1010.1876 [nucl-th].

[17] Derek Teaney and Li Yan. "Non linearities in the harmonic spectrum of heavy ion collisions with ideal and viscous hydrodynamics". In: *Phys. Rev.* C86 (2012), p. 044908. DOI: 10.1103/PhysRevC.86.044908. arXiv: 1206.1905 [nucl-th].

[18] Li Yan. "A flow paradigm in heavy-ion collisions". In: *Chin. Phys.* C42.4 (2018), p. 042001. DOI: 10.1088/1674-1137/42/4/042001. arXiv: 1712.04580 [nucl-th].

[19] Bjoern Schenke, Prithwish Tribedy, and Raju Venugopalan. "Fluctuating Glasma initial conditions and flow in heavy ion collisions". In: *Phys. Rev. Lett.* 108 (2012), p. 252301. DOI: 10.1103/PhysRevLett.108.252301. arXiv: 1202.6646 [nucl-th].

[20] Sergei A. Voloshin, Arthur M. Poskanzer, and Raimond Snellings. "Collective phenomena in non-central nuclear collisions". In: *Landolt-Bornstein* 23 (2010), pp. 293–333. DOI: 10.1007/978-3-642-01539-7_10. arXiv: 0809.2949 [nucl-ex].

[21] Francois Gelis et al. "The Color Glass Condensate". In: *Ann. Rev. Nucl. Part. Sci.* 60 (2010), pp. 463–489. DOI: 10.1146/annurev.nucl.010909.083629. arXiv: 1002.0333 [hep-ph].

[22] F. Gelis. "Color Glass Condensate and Glasma". In: *Int. J. Mod. Phys.* A28 (2013), p. 1330001. DOI: 10.1142/S0217751X13300019. arXiv: 1211.3327 [hep-ph].

[23] Jiangyong Jia. "Event-shape fluctuations and flow correlations in ultra-relativistic heavy-ion collisions". In: *J. Phys.* G41.12 (2014), p. 124003. DOI: 10.1088/0954-3899/41/12/124003. arXiv: 1407.6057 [nucl-ex].

[24] Serguei Chatrchyan et al. "Observation of long-range near-side angular correlations in proton-lead collisions at the LHC". In: *Phys. Lett.* B718 (2013), pp. 795–814. DOI: 10.1016/j.physletb.2012.11.025. arXiv: 1210.5482 [nucl-ex].

[25] Betty Abelev et al. "Long-range angular correlations on the near and away side in p-Pb collisions at $\sqrt{s_{NN}}$ = 5.02 TeV". In: *Phys. Lett.* B719 (2013), pp. 29–41. DOI: 10.1016/j.physletb.2013.01.012. arXiv: 1212.2001 [nucl-ex].

[26] Georges Aad et al. "Observation of Associated Near-Side and Away-Side Long-Range Correlations in $\sqrt{s_{NN}}$=5.02$TeVProton-LeadCollisionswiththeATLASDe$ In: *Phys. Rev. Lett.* 110.18 (2013), p. 182302. DOI: 10.1103/PhysRevLett.110.182302. arXiv: 1212.5198 [hep-ex].

[27] Georges Aad et al. "Measurement of long-range pseudorapidity correlations and azimuthal harmonics in $\sqrt{s_{NN}}$ = 5.02 TeV proton-lead collisions with the ATLAS detector". In: *Phys. Rev.* C90.4 (2014), p. 044906. DOI: 10.1103/PhysRevC.90.044906. arXiv: 1409.1792 [hep-ex].

[28] Vardan Khachatryan et al. "Evidence for Collective Multiparticle Correlations in p-Pb Collisions". In: *Phys. Rev. Lett.* 115.1 (2015), p. 012301. DOI: 10.1103/PhysRevLett.115.012301. arXiv: 1502.05382 [nucl-ex].

[29] Nicolas Borghini, Phuong Mai Dinh, and Jean-Yves Ollitrault. "A New method for measuring azimuthal distributions in nucleus-nucleus collisions". In: *Phys. Rev.* C63 (2001), p. 054906. DOI: 10.1103/PhysRevC.63.054906. arXiv: nucl-th/0007063 [nucl-th].

[30] Ante Bilandzic, Raimond Snellings, and Sergei Voloshin. "Flow analysis with cumulants: Direct calculations". In: *Phys. Rev.* C83 (2011), p. 044913. DOI: 10.1103/PhysRevC.83.044913. arXiv: 1010.0233 [nucl-ex].

[31] Ante Bilandzic et al. "Generic framework for anisotropic flow analyses with multiparticle azimuthal correlations". In: *Phys. Rev.* C89.6 (2014), p. 064904. DOI: 10.1103/PhysRevC.89.064904. arXiv: 1312.3572 [nucl-ex].

[32] Georges Aad et al. "Measurement of flow harmonics with multi-particle cumulants in Pb+Pb collisions at $\sqrt{s_{\mathrm{NN}}}$ = 2.76 TeV with the ATLAS detector". In: *Eur. Phys. J.* C74.11 (2014), p. 3157. DOI: 10.1140/epjc/s10052-014-3157-z. arXiv: 1408.4342 [hep-ex].

[33] Jaroslav Adam et al. "Correlated event-by-event fluctuations of flow harmonics in Pb-Pb collisions at $\sqrt{s_{\mathrm{NN}}}$ = 2.76 TeV". In: *Phys. Rev. Lett.* 117 (2016), p. 182301. DOI: 10.1103/PhysRevLett.117.182301. arXiv: 1604.07663 [nucl-ex].

[34] H. Niemi, K. J. Eskola, and R. Paatelainen. "Event-by-event fluctuations in a perturbative QCD + saturation + hydrodynamics model: Determining QCD matter shear viscosity in ultrarelativistic heavy-ion collisions". In: *Phys. Rev.* C93.2 (2016), p. 024907. DOI: 10.1103/PhysRevC.93.024907. arXiv: 1505.02677 [hep-ph].

[35] Piotr Bozek and Wojciech Broniowski. "Collective dynamics in high-energy proton-nucleus collisions". In: *Phys. Rev.* C88.1 (2013), p. 014903. DOI: 10.1103/PhysRevC.88.014903. arXiv: 1304.3044 [nucl-th].

[36] Kevin Dusling and Raju Venugopalan. "Comparison of the color glass condensate to dihadron correlations in proton-proton and proton-nucleus collisions". In: *Phys. Rev.* D87.9 (2013), p. 094034. DOI: 10.1103/PhysRevD.87.094034. arXiv: 1302.7018 [hep-ph].

[37] Gökçe Başar and Derek Teaney. "Scaling relation between pA and AA collisions". In: *Phys. Rev.* C90.5 (2014), p. 054903. DOI: 10.1103/PhysRevC.90.054903. arXiv: 1312.6770 [nucl-th].

[38] Björn Schenke, Sören Schlichting, and Raju Venugopalan. "Azimuthal anisotropies in p+Pb collisions from classical Yang–Mills dynamics". In: *Phys. Lett.* B747 (2015), pp. 76–82. DOI: 10.1016/j.physletb.2015.05.051. arXiv: 1502.01331 [hep-ph].

[39] Vardan Khachatryan et al. "Evidence for collectivity in pp collisions at the LHC". In: *Phys. Lett.* B765 (2017), pp. 193–220. DOI: 10.1016/j.physletb.2016.12.009. arXiv: 1606.06198 [nucl-ex].

[40] Vardan Khachatryan et al. "Long-range two-particle correlations of strange hadrons with charged particles in pPb and PbPb collisions at LHC energies". In: *Phys. Lett.* B742 (2015), pp. 200–224. DOI: 10.1016/j.physletb.2015.01.034. arXiv: 1409.3392 [nucl-ex].

[41] G. Aad et al. "The ATLAS Inner Detector commissioning and calibration". In: *Eur. Phys. J.* C70 (2010), pp. 787–821. DOI: 10.1140/epjc/s10052-010-1366-7. arXiv: 1004.5293 [physics.ins-det].

[42] *ATLAS inner detector: Technical Design Report, 1*. Technical Design Report ATLAS. Geneva: CERN, 1997. URL: https://cds.cern.ch/record/331063.

[43] G. Aad et al. "Readiness of the ATLAS Liquid Argon Calorimeter for LHC Collisions". In: *Eur. Phys. J.* C70 (2010), pp. 723–753. DOI: 10.1140/epjc/s10052-010-1354-y. arXiv: 0912.2642 [physics.ins-det].

[44] Morad Aaboud et al. "Performance of the ATLAS Trigger System in 2015". In: *Eur. Phys. J.* C77.5 (2017), p. 317. DOI: 10.1140/epjc/s10052-017-4852-3. arXiv: 1611.09661 [hep-ex].

[45] Vardan Khachatryan et al. "Evidence for transverse momentum and pseudorapidity dependent event plane fluctuations in PbPb and pPb collisions". In: *Phys. Rev.* C92.3 (2015), p. 034911. DOI: 10.1103/PhysRevC.92.034911. arXiv: 1503.01692 [nucl-ex].

[46] Morad Aaboud et al. "Measurement of longitudinal flow decorrelations in Pb+Pb collisions at 2.76 and 5.02 TeV with the ATLAS detector". In: *Eur. Phys. J.* C78.2 (2018), p. 142. DOI: 10.1140/epjc/s10052-018-5605-7. arXiv: 1709.02301 [nucl-ex].

[47] Jiangyong Jia et al. "Observables for longitudinal flow correlations in heavy-ion collisions". In: *J. Phys.* G44.7 (2017), p. 075106. DOI: 10.1088/1361-6471/aa74c3. arXiv: 1701.02183 [nucl-th].

[48] Jiangyong Jia, Mingliang Zhou, and Adam Trzupek. "Revealing long-range multiparticle collectivity in small collision systems via subevent cumulants". In: *Phys. Rev.* C96.3 (2017), p. 034906. DOI: 10.1103/PhysRevC.96.034906. arXiv: 1701.03830 [nucl-th].

[49] Giuliano Giacalone et al. "Symmetric cumulants and event-plane correlations in Pb + Pb collisions". In: *Phys. Rev.* C94.1 (2016), p. 014906. DOI: 10.1103/PhysRevC.94.014906. arXiv: 1605.08303 [nucl-th].

[50] Georges Aad et al. "Measurement of event-plane correlations in $\sqrt{s_{NN}}$ = 2.76 TeV lead-lead collisions with the ATLAS detector". In: *Phys. Rev.* C90.2 (2014), p. 024905. DOI: 10.1103/PhysRevC.90.024905. arXiv: 1403.0489 [hep-ex].

[51] Peng Huo, Jiangyong Jia, and Soumya Mohapatra. "Elucidating the event-by-event flow fluctuations in heavy-ion collisions via the event shape selection technique". In: *Phys. Rev.* C90.2 (2014), p. 024910. DOI: 10.1103/PhysRevC.90.024910. arXiv: 1311.7091 [nucl-ex].

[52] Xiang-Yu Wu et al. "Longitudinal fluctuations and decorrelations of anisotropic flows at the LHC and RHIC energies". In: (2018). arXiv: 1805.03762 [nucl-th].

[53] Long-Gang Pang et al. "Decorrelation of anisotropic flow along the longitudinal direction". In: *Eur. Phys. J.* A52.4 (2016), p. 97. DOI: 10.1140/epja/i2016-16097-x. arXiv: 1511.04131 [nucl-th].

[54] Georges Aad et al. "Measurement of the correlation between flow harmonics of different order in lead-lead collisions at $\sqrt{s_{NN}}$=2.76 TeV with the ATLAS detector". In: *Phys. Rev.* C92.3 (2015), p. 034903. DOI: 10.1103/PhysRevC.92.034903. arXiv: 1504.01289 [hep-ex].

[55] Albert M Sirunyan et al. "Observation of Correlated Azimuthal Anisotropy Fourier Harmonics in *pp* and $p + Pb$ Collisions at the LHC". In: *Phys. Rev. Lett.* 120.9 (2018), p. 092301. DOI: 10.1103/PhysRevLett.120.092301. arXiv: 1709.09189 [nucl-ex].

[56] Peng Huo et al. “Importance of non-flow in mixed-harmonic multi-particle correlations in small collision systems”. In: *Phys. Lett.* B777 (2018), pp. 201–206. DOI: 10.1016/j.physletb.2017.12.035. arXiv: 1710.07567 [nucl-ex].

[57] Morad Aaboud et al. “Correlated long-range mixed-harmonic fluctuations measured in pp, p+Pb and low-multiplicity Pb+Pb collisions with the ATLAS detector”. In: (2018). arXiv: 1807.02012 [nucl-ex].

[58] Sruthy Jyothi Das et al. “Relating centrality to impact parameter in nucleus-nucleus collisions”. In: *Phys. Rev.* C97.1 (2018), p. 014905. DOI: 10.1103/PhysRevC.97.014905. arXiv: 1708.00081 [nucl-th].

[59] Georges Aad et al. “Observation of Long-Range Elliptic Azimuthal Anisotropies in $\sqrt{s}$ =13 and 2.76 TeV pp Collisions with the ATLAS Detector”. In: *Phys. Rev. Lett.* 116.17 (2016), p. 172301. DOI: 10.1103/PhysRevLett.116.172301. arXiv: 1509.04776 [hep-ex].

[60] Morad Aaboud et al. “Measurements of long-range azimuthal anisotropies and associated Fourier coefficients for pp collisions at $\sqrt{s}$ = 5.02 and 13 TeV and p+Pb collisions at $\sqrt{s_{\mathrm{NN}}}$ = 5.02 TeV with the ATLAS detector”. In: *Phys. Rev.* C96.2 (2017), p. 024908. DOI: 10.1103/PhysRevC.96.024908. arXiv: 1609.06213 [nucl-ex].

[61] Morad Aaboud et al. “Measurement of multi-particle azimuthal correlations in pp, p+Pb and low-multiplicity Pb+Pb collisions with the ATLAS detector”. In: *Eur. Phys. J.* C77.6 (2017), p. 428. DOI: 10.1140/epjc/s10052-017-4988-1. arXiv: 1705.04176 [hep-ex].

[62] Morad Aaboud et al. “Measurement of long-range multiparticle azimuthal correlations with the subevent cumulant method in pp and $p+Pb$ collisions with the ATLAS detector at the CERN Large Hadron Collider”. In: *Phys. Rev.* C97.2 (2018), p. 024904. DOI: 10.1103/PhysRevC.97.024904. arXiv: 1708.03559 [hep-ex].